DESIGN AND EPITAXIAL GROWTH OF VERTICAL CAVITY SURFACE-EMITTING LASERS (VCSEL) EMITTING AT ULTRAVIOLET WAVELENGTH

A Dissertation
Presented to
The Academic Faculty

by

Mohamed ABID

In Partial Fulfillment
of the Requirements for the Degree
Doctor of Philosophy
in the
School of Electrical and Computer Engineering

Georgia Institute of Technology
May 2013

DESIGN AND EPITAXIAL GROWTH OF VERTICAL CAVITY SURFACE-EMITTING LASERS (VCSEL) EMITTING AT ULTRAVIOLET WAVELENGTH

Approved by:

Dr. Abdallah Ougazzaden, Advisor
School of ECE
Georgia Institute of Technology

Dr. Russel Dupuis
School of ECE
Georgia Institute of Technology

Dr. Paul Voss
School of ECE
Georgia Institute of Technology

Dr. James Kenney
School of ECE
Georgia Institute of Technology

Dr. Mohammed Cherkaoui
School of ME
Georgia Institute of Technology

Date Approved: 04/04/2013

In memory of my father Mongi

This dissertation is dedicated to my wife Hajer, my brother Skander, my sister Dorra, and my mother Amel. Their support and love have encouraged me on this long path.

ACKNOWLEDGEMENTS

The results presented in this work could not have been achieved without the contribution and support for all the people listed below. I believe that the multitude of people with whom I have had the great fortune of interacting should be acknowledged.

Firstly, I owe a great many thanks to my supervisor Prof. Abdallah Ougazzaden and for giving me this opportunity to work in such challenging topic and all the suggestions and guidance that he has provided to me for my research. His assistance and encouragement helped me overcome the different obstacles I encountered over the past years. Also thanks go to Prof. Russel Dupuis, Prof. Paul Voss and Jean Paul Salvestrini for their contribution, insights and guidances.

I am very grateful to Gaelle Orsal for assistance with SEM, AFM, and X-Ray Diffraction, her kind corrections and comments in the articles and dissertation, and her precious help in the scientific work.

This project would have never gotten off the ground for me without the extensive training and help of Tarik Moudakir and Simon Gautier in the MOVPE lab. Many thanks for introducing me to the MOVPE epitaxial growth of the III-N alloys and sharing your knowledge on growing the valuable samples throughout the years.

I would like to thank Zakaria Djebbour for his transmission/reflection measurements of my several samples, for his enlightening discussions and especially for his best to give me the good results from some difficult samples.

I am grateful to Otmane En Naciri for the worthy discussions and measurements in the optical properties investigation with Ellipsometry.

I would like to acknowledge Gilles Patriarche for his TEM measurements and reports and for his nice cooperation and infinite knowledge. Appreciation is also extended to Jerome Gleize for Raman analysis, Vinod Ravindran for PL investigation, Frederic Genty for FTIR measurements, François Jomard for SIMS profiles and David

Alamarguy for XPS measurements. Thank you all for your suggestions and help, which have contributed a great deal to this thesis.

I would like to acknowledge all the member of the "nitride groups" that I might have forgotten for their help in the different occasions and the staff of Georgiatech Lorraine, in particular Josyane, John, sandrine, Francis, Christine and Durdane.

My thanks go to Jeramy, Gaelle, Tarik and Simon for reading and making comments and corrections on the manuscript.

Of course, it wasn't only fellow worker that deserve my gratitude. More importantly, I would like to thank all my friend who took the time to distract me and helped me to regain some energy: Fred, Vinod, Konstantinos, Wui, Manas, Jeramy, Tarik, Simon, Wissem, Wajdi, Malek ... No matter how cool and exciting the research, the best times are the soccer matches, the game nights, the trip to Tunisia and just hanging-out with you guys.

Finally, I want to express my deepest gratitude to my family, especially my mother and my wife for giving me their great love, for all their care and endless support during all those years, and especially at the end of my PHD. I am also deeply indebted to Dorra, Hatem, Skander and Malek. Though you are 2000 km away, I have always felt you were right beside me throughout all my struggles and accomplishments.

TABLE OF CONTENTS

LIST OF TABLES

LIST OF FIGURES

SUMMARY

One of the key advances in photonic technology in recent decades was the development of a new type of diode lasers emitting in the visible and infrared region. These vertical cavity surface-emitting lasers (VCSELs) emerged from a laboratory curiosity in 1977 [13] to an object of industrial mass production [14] and are currently used in many applications. The applications include communication, printing, and absorption spectroscopy [15]. Their rise in credibility has largely been motivated by the rapid evolution of their performance, the more sweeping recognition of their compatibility with low-cost wafer-scale fabrication, and their possible formation into specific arrays with no change in the fabrication procedure.

Various applications such as advanced chemical sensors and high-density optical storage require coherent and small-size ultraviolet-emitting devices (below 400nm). Therefore, to extend the VCSEL emission to the ultraviolet (UV) region, intensive efforts have been made in the VCSEL technology. However, the achievement of such UV VCSEL is very challenging because of the various limitations and issues. The issues noticeably include the carrier injection, optical confinement, and highly reflective distributed Bragg reflectors (DBR) structures with a broad bandwidth operating in the UV region [16]. In this context, motivated by the reported large refractive index induced by boron incorporation [7], we propose to introduce the boron-based material systems (BAlGaN) as an innovative solution to address some of the encountered difficulties.

The objective of the proposed research is to investigate and optimize new wide-bandgap BAlGaN material systems and illustrate their incorporation into the building blocks of vertical cavity surface-emitting laser structures for operation in the UV spectral range (λ<400nm).

Toward this goal, we have focused our research activities in three main directions. The first direction is devoted to the simulation of DBRs reflectivity by taking into

consideration the experimental refractive indexes. Once the materials needed in the different components of the VCSEL are well defined, the second direction lies in the achievement of growth conditions optimization and characterization of the new wide-bandgap BAlGaN material systems. The study has led to the structural and morphological quality improvement of (B,Al,Ga)N materials. Unique optical properties of the BGaN and BAlN materials were also demonstrated. Upon demonstrating the materials' promising optical characteristics, the final direction consists of the epitaxial growth and characterization of the highly reflective DBRs and active region of the UV VCSEL structure.

CHAPTER 1

INTRODUCTION

1.1 Motivation and applications of UV VCSELs

The context of this project falls in the wide range of potential applications of UV light sources, some of which are already available as commercial products in our everyday lives, while others are still under extensive research and development.

One major application of UV sources is high-density optical storage systems that would benefit from the short wavelength of compact UV sources. In fact, the recording density is inversely proportional to the wavelength squared [17]. UV sources can destroy bacteria and viruses making these sources useful for sterilization, water and air purification, and environmental problems [18]. These sources can also be of paramount importance for optical imaging systems ranging from sophisticated astronomical telescopes to household cameras and security systems. Furthermore, UV sources are required for some medical applications like eye surgery, light therapy (exposure to UV light 300-320nm), and UV radiations to reduce inflammatory responses. UV sources cover additional fields, such as advanced biological and chemical sensors, laser lithography, and white-light generation. Finally, the covert communication systems can use UV light rather than radio waves as a medium for communication; the transmitted UV light may contain both voice information and other data [19]. Examples of the important applications mentioned earlier are shown in Figure 1.

To date, most of UV light sources are gas sources, which include excimer lasers and mercury lamps. However, these sources present few limitations related to their low level of performance, low reliability, significant size, and mainly to the toxic substances they contain, leading to significant environmental nuisance.

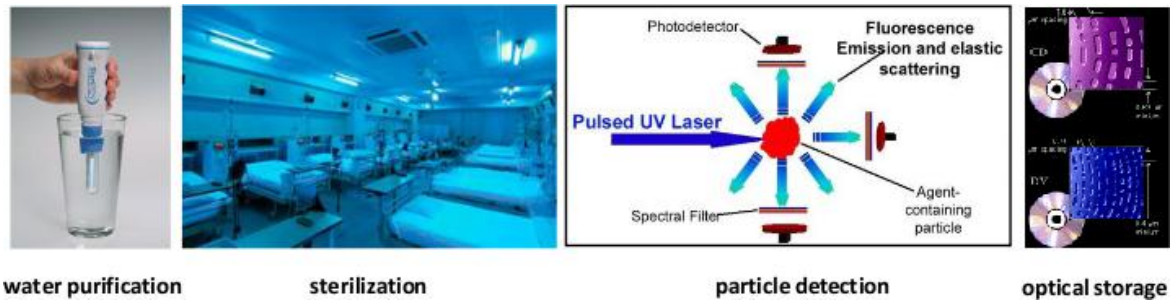

Figure 1: Some applications of UV sources.

The durability and compactness of semiconductor solid-state light-emitting devices make them ideal for various applications. Light-emitting devices are highly efficient, cheap, reliable, and harmless to the environment. Moreover, the emission wavelength can be tuned by changing the semiconductor composition. As a matter of fact, UV semiconductor light sources are of great technological interest in our every-day life. Figure 2 presents the three major configurations for light-emitting devices, including light-emitting diodes (LEDs) and laser diodes (LDs).

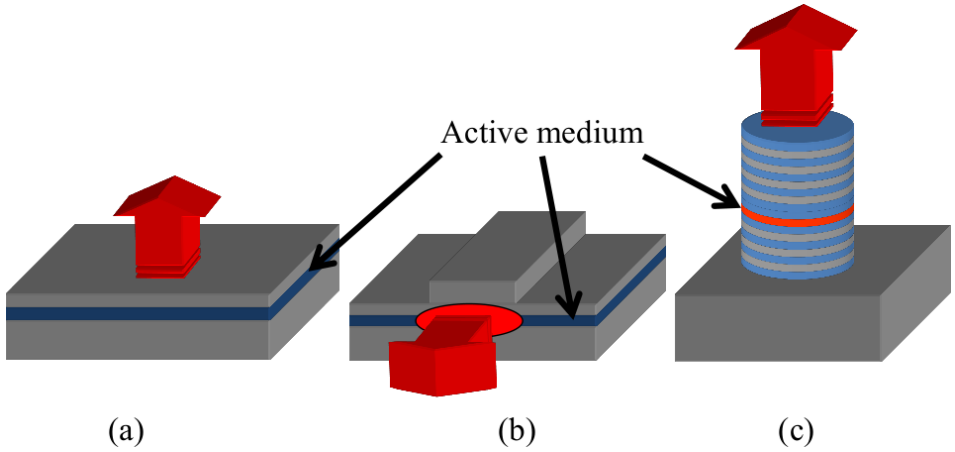

Figure 2: Three typical structures of light-emitting devices: (a) light-emitting diodes (300 μm long), (b) edge-emitting laser (300 μm long), and (c) vertical cavity surface-emitting laser (5 μm long).

The primary advantage of LEDs is that they are much cheaper than lasers, because of a much simpler processing. However, LEDs present several drawbacks, including the wide angle of emission and the large spectral distribution [20]. In contrast

to LEDs, lasers present a more precise spectrum incurring less chromatic dispersion and provide more intensity.

Among semiconductor laser devices, VCSELs are undoubtedly one of the more sophisticated configurations. VCSELs have attracted tremendous interest over the past few years as they present advantages over edge-emitting lasers. The advantages consist of a high-output optical power and a thin cavity. The last feature makes VCSELs less prone to dislocations than edge-emitting lasers, hence, leading to higher-quality structures. Additionally, since on-wafer testing prior to dicing and packaging can be carried out with VCSELs, the cost of production is much lower than that of edge-emitting lasers. Finally, the compact size of VCSELs yields more devices per wafer.

1.2 Overview of the fundamental properties of III-N materials

Toward the development of VCSEL devices emitting in the UV spectrum, III-nitrides (also known as nitrides or III-N) are undoubtedly the most adapted materials with emission wavelengths going as low as 200 nm. In fact, depending on the alloy composition, nitride materials with bandgap spanning from infrared through visible to UV wavelengths can be demonstrated [21, 22, 23]. A map of the different binaries forming the III-N materials system and their ternaries and quaternaries is shown in Figure 3. It is observed that as we move along the lines linking the different binaries, a very wide spectral range is covered. The most used technique to grow nitride materials is metalorganic vapor-phase epitaxy (MOVPE).

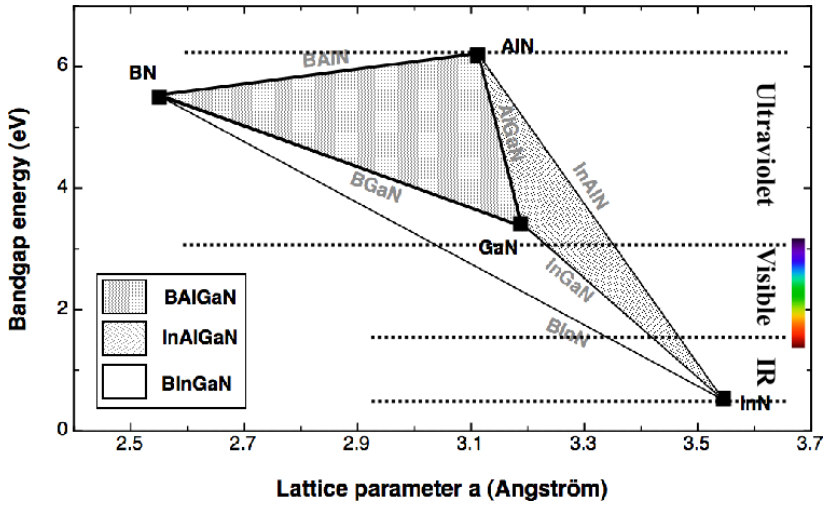

Figure 3: Bandgap energy versus in-plane lattice parameter diagram for III-N materials.

In contrast to II-VI ZnCdSSe systems, which can also achieve these wavelengths [24], III-nitride alloys represent a very special class of materials with unique properties. In fact, these materials present several remarkable chemical and physical properties making them particularly attractive and suitable for reliable applications. In addition to the bandgap flexibility mentioned earlier, nitride materials exhibit interesting thermal conductivity and fairly high bond strengths which could improve the device reliability [25]. The nitrides are also resistant to chemical etching enabling III-N based devices to operate under hostile environments [26]. Additionally, among the III-V conventional semiconductors, III-Nitrides are the only systems showing a built-in electric polarization referred as "spontaneous polarization". This polarization is very important in several optoelectronic applications such as lasers and also other devices as High electron mobility transistors (HEMT).

Driven by the paramount interest in reliable electronic and optoelectronic device applications, III-N alloys were intensively investigated. Taking advantage of their unique material characteristics, the objective is to push the limits beyond the ability of conventional devices. These alloys were not only suitable for light-emitting sources but also for solar cells and photodetectors. Additionally, because of their robustness, they are

candidates for high-temperature, high power, and high frequency electronic applications such as transistors or thyristors.

Despite their unique intrinsic properties and the performed intense research efforts worldwide on nitride materials and devices, the progress of the research on nitride devices is still hampered by several technical limitations. The following sections tend to review the intrinsic properties of the III-N materials and give a short overview of the different issues they might suffer from.

1.2.1 Structural properties

Group III-nitrides can be categorized into two allotropes: cubic and hexagonal. In fact AlN, GaN, InN, and their alloys can crystallize in both hexagonal wurtzite (α-phase) and zinc-blende (β-phase) prototypes. However, the nitride alloys wurtzite crystal system is energetically and thermodynamically favored over cubic (zinc-blende) structure which could exist by forcing the film to grow on {001} crystal planes of cubic substrates. It is important to note that the coexistence of zinc-blende (ZB) and wurtzite (W) crystal structures is possible as they slightly differ in the stacking sequence. This crystal mixture results on stacking faults in the grown films, as will be shown in the BGaN structural study in Chapter 4.

Cubic-phase structure alloys will not be discussed further in this report as the vast majority of research on nitride alloys focused on the stable hexagonal form. Additionally, all samples in this study were grown under conditions conductive to wurtzite structures.

GaN, AlN, BN, and InN have direct room temperature bandgaps of 3.4 eV, 6.2 eV, 5.5 eV, and 0.7 eV, respectively. This direct bandgap is especially fortuitous as it allows high quantum efficiency light emitters to be fabricated using nitride materials.

The primitive unit cell of hexagonal wurtzite system is a parallelepiped with a basis of four atoms. Each atom of the structure can be seen as surrounded by the four nearest neighboring atoms forming tetrahedron bounding. The four nearest atomic

neighbors of the other type are located at the four corners of the tetrahedron, as illustrated in Figure 4a. These planes consist of two embedded hexagonal ABABAB, where "A" represents the first cubic lattice (FCC) composed by III elements and "B" represents the second FCC lattice referring to N elements. Each atom in the hexagonal structure can be described by a set of vectors:

$$R = n_1a_1 + n_2a_2 + n_3c \quad , \tag{1}$$

where a_1, a_2, and c are the lattice vectors, and n_1, n_2, and n_3 are integers.

To identify the planes and orientations in the hexagonal system, four indexes are normally used, referred as the millers indexes (hkil). As shown in Figure 4b, the three basis vectors have an angle of 120°. Consequently, i can be omitted and the millers indexes will be written (hkl).

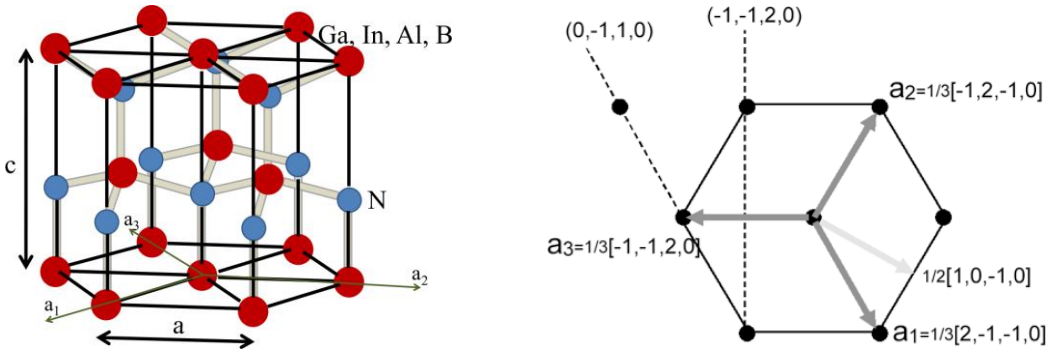

(a) (b)

Figure 4: (a) III-N wurtzite structures. (b) Bravais Millers index systems.

In the hexagonal phase, the plane distance is depicted by Equation 2:

$$d = \sqrt{\frac{1}{\frac{4}{3}\frac{h^2+hk+k^2}{a^2} + \frac{l^2}{c^2}}}, \tag{2}$$

whereas hkl are the miller indexes, and a and c are the in- and out of plane lattice parameters. These parameters are the height of hexagonal (c) and the edge length of basal-plane hexagonal (a), as shown in Figure 4a. In an ideal wurtzite structure, the c/a

ratio is 1.6633, which is quite close from III-N binaries c/a ratio. The lattice parameters are summarized in Table 1.

Table 1: Properties of the different III-Nitride binaries (after [1]).

Parameters	GaN	AlN	BN	InN
a (Å)	3.189	3.122	2.55	3.548
c (Å)	5.185	4.982	4.17	5.718
c/a	1.626	1.596	1.635	1.612
Eg (eV)	3.42	6.28	5.9	0.7
Electron affinity (eV)	4.1	0.6	4.1	5.8

The theoretical lattice parameters of ternaries can be predicted by Vegard's law [27] using the composition-weighted average of the different binaries forming the alloy. The lattice parameters can be expressed by the following equation:

$$a, c(A_x B_{1-x} N) = xa, c(AN) + (1-x)a, c(BN). \quad (3)$$

In comparison to other group III-V compound semiconductors such as InP and GaAs, the nitride alloys have a group of III-nitrogen covalent bond with very strong chemical bonds. This feature is the origin of some useful properties of nitride materials. This is caused by the large difference in electronegativity between the different III elements and nitrogen (Table 2) atoms and the small size of the N atom. In fact, in the III-N configuration, the involved electrons are attracted by the high coulomb potential of the nitrogen atomic nucleus. This results in the strong ionicity of the metal nitrogen bond.

Table 2: Summary of the different electronegativities and covalent radius of the different III-Nitride atoms [2].

Parameters	Al	Ga	B	In	N
Electronegativity (eV)	1.61	1.81	2.04	1.78	3.04
Covalent radius (Å)	1.21	1.22	0.84	1.42	0.71

Another consequence of the small radius of nitrogen (0.71 A) in comparison to As (1.18 A), P (1.10 A), and Sb (1.36 A) is the small lattice parameters of III-N alloys. Consequently, high bond energies are induced in the III-N alloys implying a high melting temperature, revealing by the way large variation in the bond energy. For instance, in opposition to Al-As alloys whose E_B and melting temperature that do not exceed 2 eV and 2000°C, respectively, the melting temperature of AlN and E_B(Al-N) are much higher. These values result noticeably in the high AlN stability. Taking advantage of their thermal and chemical stability, the III-N materials were proved as suitable candidates for high-frequency, high-power, and high-temperature applications [28].

1.2.2 Optical properties

The development of optoelectronic devices based on nitride alloys requires a detailed knowledge of the optical constants over an extended photon energy range. In this section, the major optical properties including the optical bandgap and the complex index of refraction will be summarized.

Optical bandgap: Energy gaps (E_G) for the wurtzite group III-nitride compounds and their related alloys span the wide range from 0.7 to 6.2 eV. Therefore, as illustrated in Figure 3, almost the entire visible and deep-UV wavelengths are covered. Equation 4 illustrates the link between eV and nm values at room temperature.

$$\lambda(nm) = \frac{1240(eVnm)}{E_g(eV)}. \tag{4}$$

For this study, UV devices are the ultimate goal of this study, and AlN layers are required in the DBR and multiple quantum well (MQW) blocks. AlN is a direct bandgap material as the valence band maximum and the conduction band minimum lay at the center of the Brillouin zone (Γ point). The AlN optical bandgap is slightly equal to the distance between them. The calculated band structure near Γ point of hexagonal AlN is illustrated in Figure 5 [4, 28].

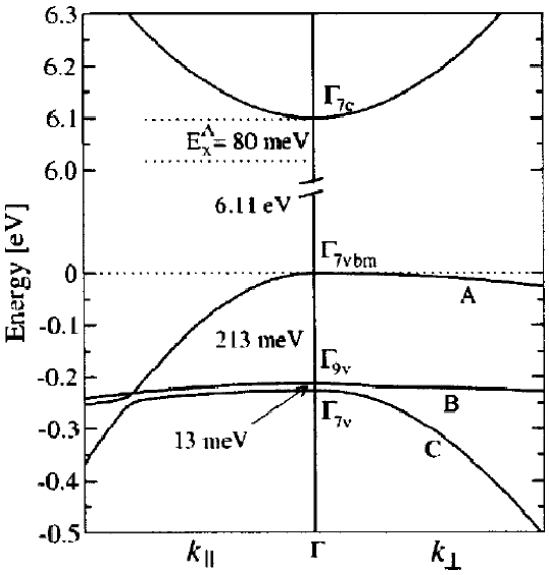

Figure 5: Calculated band structure of wurtzite AlN near the Γ point [4].

Knowledge of the III-N ternary and quaternary alloys in relationship with III-elements composition is fundamental in several applications. For example, the optical bandgap defines the wavelength emission of light-emitting devices and can also be used to impose the cutoff wavelength for detectors. As a matter of fact, an accurate determination of the bandgap as a function of III-element content is fundamental for bandgap engineering in the design of the different optoelectronic devices. Conventionally, to obtain the ternaries data, a linear interpolation between binary parameters is required. This approximation is valid for several parameters and constants such as lattice parameters (Table 1) and elastic constants. However, for optical bandgap, a bowing parameter was introduced to consider the non-linear term. Experimentally, a wide spectrum of bandgap-bowing parameters has been reported for nitride alloys systems. This feature can be explained by the difference in growth techniques and measurement conditions [29, 30]. For instance, as concerning the AlGaN alloys, there are many reports of various bowing parameters from -0.8 eV (upward bowing) to 2.6 eV (downward bowing). However, the most notable bowing parameter is 1eV for the entire

compositional range, as expressed by Equation 5 to illustrate the AlGaN bandgap. The bandgap-bowing parameters of the other III-Nitrides are summarized in Table 3.

$$E_g(Al_xGa_{1-x}N) = xE_g(AlN) + (1-x)E_g(GaN) - 1 * x * (1-x). \quad (5)$$

Table 3: Energy-bowing parameters of the different nitride ternaries.

	AlGaN	BAlN	BGaN	AlInN	InGaN
Bowing (eV)	1 [31]	5.45 [32]	9 [33]	2.5 [31]	3 [31]

Taking into consideration the most common bowing parameters, Figure 6 presents the bandgap versus lattice constant dependance of direct bandgap semiconductors compounds and their related alloys.

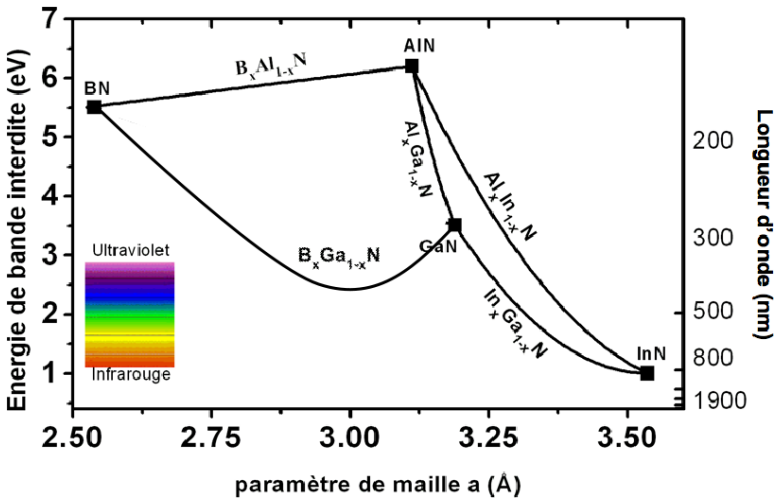

Figure 6: Bandgap energy versus lattice parameter diagram for III-N materials taking into consideration bandgap-bowing parameters.

Another important parameter linked to the bandgap energy that can be critical for the design of nitride optoelectronic device is the band offset. The offset is also referred to the band structure discontinuity at each hetero-interface. The band offset is tied to the electron affinity of each material. Therefore, intensive research focused on the calculation of the band offset in the different systems using several techniques, including photoluminescence, cathodoluminescence, and X-ray spectroscopy. As a general rule for

nitride heterostructures grown on relaxed GaN templates, a 3/7 ratio is used to calculate the band offset between the conduction and valence band. For example, if we consider an AlN/GaN interface, the bandgap variation between the binaries compounds is ΔE_g = 2.8eV, leading to a ΔE_c = 1.96eV and ΔE_v = 0.84eV band offset [34]. As a direct consequence of this band offset distribution, the efficiency of trapping or blocking electrons is higher than holes in the nitride heterostructures.

Complex index of refraction: The complex index of refraction describes the propagation of light in a semiconductor and is expressed by Equation 6.

$$N = n - ik, \tag{6}$$

whereas n is the refractive index indicating the phase velocity of light in the material, and k is referred as the extinction coefficient describing the absorption loss when the electromagnetic wave propagates through the material. Both n and k depend on the radiation wavelength.

The refractive index is denoted by the following equation:

$$n = \frac{c}{\mu}, \tag{7}$$

whereas μ is the the phase velocity of the radiation of a given frequency, and c is the speed of all electromagnetic radiation in vacuum ($c = 3*10^8$ m/s).

It is fundamental to accurately determine the refractive index of the nitride alloys to design advanced optoelectronic devices, including distributed Bragg reflectors and light-emitting devices. As a matter of fact, the refractive indexes of the different ternaries that can potentially be used in this study are depicted in Figure 7.

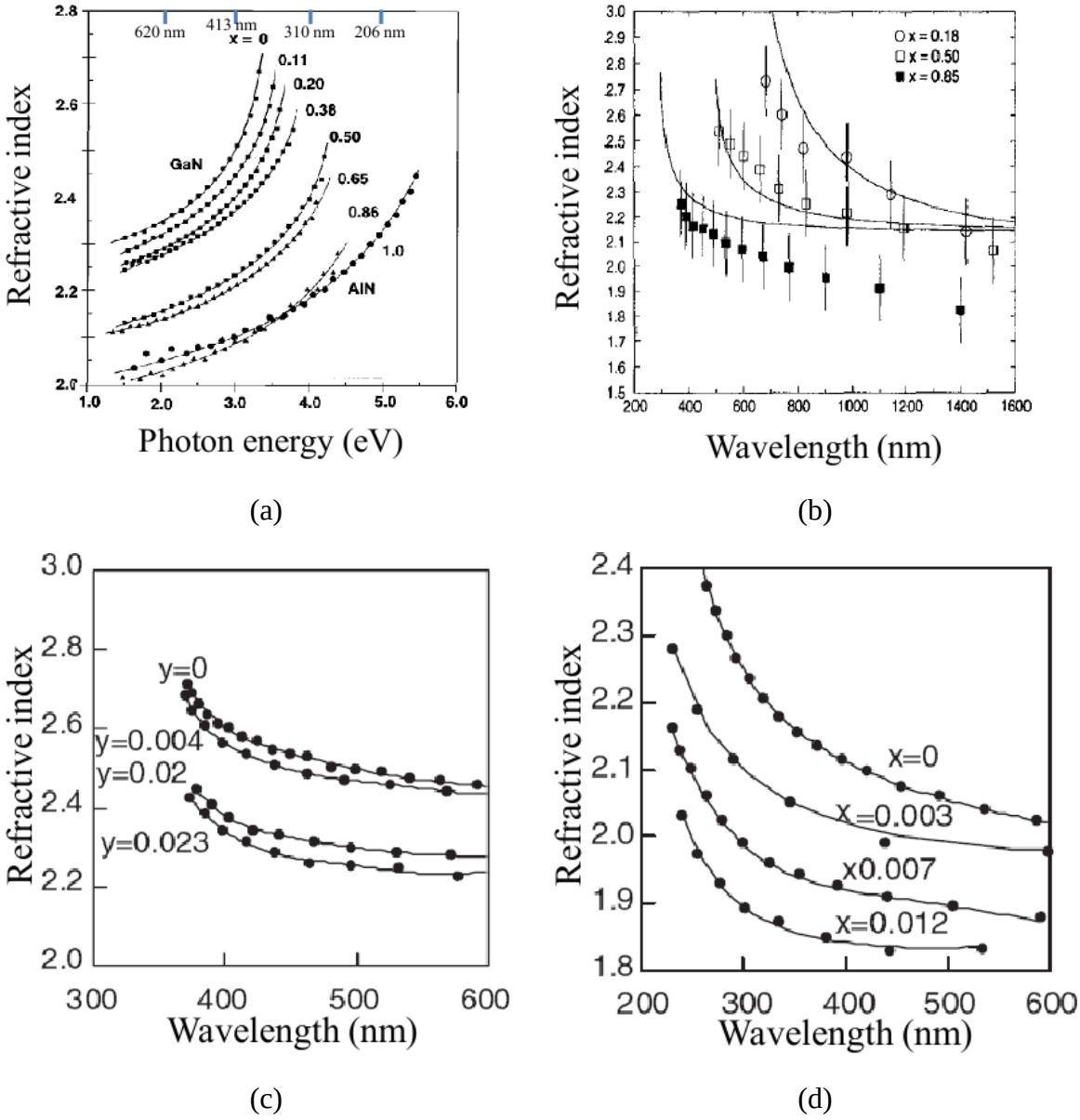

Figure 7: Refractive index of (a) AlGaN [5], (b) AlInN [6], (c) BGaN [7], and (d) BAlN [7] as a function of the wavelength/energy.

As it was widely used in this study in the different simulations and experimentations, the AlGaN refractive index as a function of the wavelength and the Al composition is given in Equation 8 [5]. Details of measurement and estimation of the refractive index of BGaN and BAlN layers will be discussed in Chapter 4.

$$n(Al_xGa_{1-x}N) = \sqrt{C(x) + \frac{A(x)(2 - \sqrt{(1+y)} - \sqrt{(1-y)})}{y^2}}, \quad (8)$$

where:

$$C(x) = -(2.2 \pm 0.2)x + (2.66 \pm 0.12), \quad (9)$$

$$A(x) = (3.17 \pm 0.39)\sqrt{x} + (9.98 \pm 0.27), \quad (10)$$

$$y = \frac{h\mu}{E_g(x)}. \quad (11)$$

Similarly to the refractive index dispersion, light absorption is also a critical design parameter in the different optoelectronic devices based on nitride materials. The absorption coefficient α is directly linked to the extinction coefficient k and the wavelength λ by the following equation: $\alpha = \frac{4k\Pi}{\lambda}$. The absorption coefficient is described as the reciprocal of the penetration depth of light into a bulk solid, at which the radiation energy is attenuated by a factor e.

For semiconductor layers, there are two distinct regimes in the spectral range above and below the material bandgap. Below the bandgap energy, also referred as sub-bandgap absorption, the absorption is not significant and does not affect the optical losses. However, the absorption above the bandgap, which is mainly explained by the band-to-band transitions, leads to a very strong absorption. This absorption increases as a function of photon energy, as shown in Figure 8 for AlGaN materials [5]. The nitride materials should be fully transparent to radiation with energy lower than the bandgap. However, experimentally, the presence of dislocation or free-carriers induces an increase of the material absorption. This absorption issue has to be considered in the design and simulation of the different optoelectronic components.

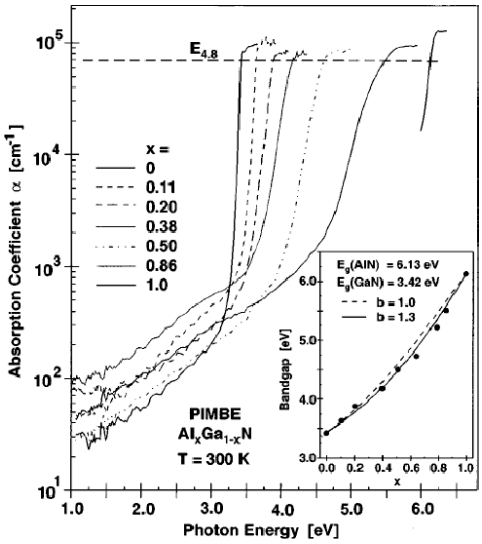

Figure 8: AlGaN absorption coefficient as a function of the energy for different Al content.

The most common and efficient techniques to measure the complex refractive index of a material are based on ellipsometry and reflection/transmission measurements. However, these techniques are not direct, and a complex modelisation is required to measure the refractive index. The process of refractive index measurements for boron-based materials is developed in Chapter 4.

1.2.3 Heterostructures and growth challenges

Major recent breakthroughs in the MOVPE growth of high-quality nitride materials enabled the fabrication of several optoelectronic devices. All devices are commonly developed from heterostructures of different semiconductor materials such as the quantum well structures for LEDs and superlattices (SL) for DBRs.

In addition to the negative effects of band structures discontinuity near the interfaces in the electrical and optical properties, the structural properties are also largely affected during the heterostructures growth. This feature is mainly caused by the difference in the in-plane lattice parameters of the different materials forming the nitrides heterostructures (Table 1).

Figure 9 illustrates the deformation origin that the nitride materials can undergo at the atomic scale where the grown layer has to adapt its lattice parameter to the substrate one. The induced strain can be either tensile when the substrate in-plane lattice parameter is larger than the grown film or compressive in the other case.

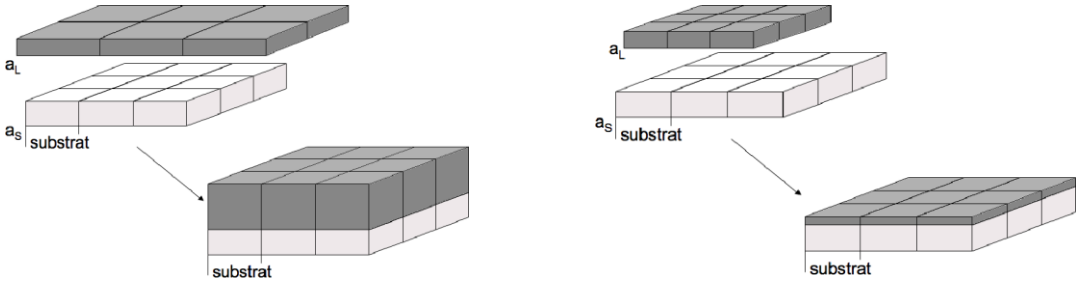

(a) (b)

Figure 9: The different strains occurring for lattice mismatched layers: (a) compressive strain ($a_{Sub}<a_{Layer}$) and (b) tensile strain ($a_{Sub}>a_{Layer}$).

The strain induces a deformation in the different dimensions for a tensile strain in the (0001) plane, as shown in Figure 10. The deformation results in a modification of the lattice parameters a and c.

The connection between the stress σ_{ij} (force per unit area) and the strain ε_{kl} (a measure of deformation per unit length) is governed by Hooke's law (Equation 12). In fact they are linked by the stiffness constants C_{mn} reported in Table 9 (Apendix A).

$$\begin{pmatrix} \sigma_{xx} \\ \sigma_{yy} \\ \sigma_{zz} \\ \sigma_{yz} \\ \sigma_{xz} \\ \sigma_{xy} \end{pmatrix} = \begin{pmatrix} c_{11} & c_{12} & c_{13} & 0 & 0 & 0 \\ c_{12} & c_{11} & c_{13} & 0 & 0 & 0 \\ c_{13} & c_{13} & c_{33} & 0 & 0 & 0 \\ 0 & 0 & 0 & c_{44} & 0 & 0 \\ 0 & 0 & 0 & 0 & c_{44} & 0 \\ 0 & 0 & 0 & 0 & 0 & \frac{1}{2}(c_{11} - c_{12}) \end{pmatrix} \begin{pmatrix} \epsilon_{xx} \\ \epsilon_{yy} \\ \epsilon_{zz} \\ \epsilon_{yz} \\ \epsilon_{xz} \\ \epsilon_{xy} \end{pmatrix} \quad (12)$$

The relative elongation of the grown film describes the variation of the lattice parameters a and c from their relaxed state. This variation is expressed by the following equations:

$$\epsilon_{zz} = \frac{c - c_0}{c_0}. \tag{13}$$

$$\epsilon_{xx} = \epsilon_{yy} = \frac{a - a_0}{a_0}. \tag{14}$$

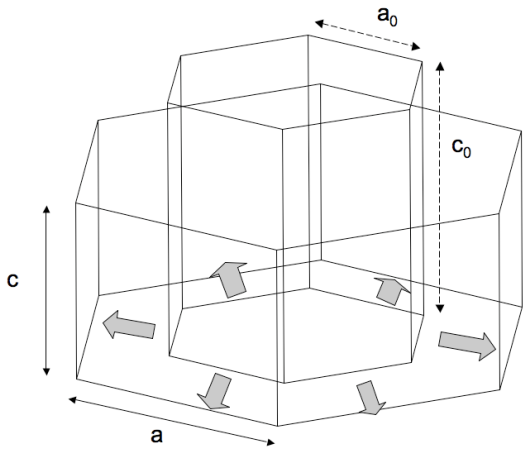

Figure 10: Illustration of the tensile strain movement. The strain induces an enlargement of the hexagonal base shrinking the unit cell along the growth direction.

As a consequence of the large in-plane lattice mismatch between nitride epilayer and conventional substrates (16% between GaN and sapphire and 3.5% between GaN and SiC), the epitaxial growth induces a large number of dislocations. These dislocations are detrimental for the optical and electrical properties of the nitride devices.

Consequently, without any strain engineering, growth is limited to a thickness referred as "the critical thickness". This issue presents a major limitation in the development of thick optoelectronic devices.

The critical thickness is governed by Equation 15 [35]:

$$h_c = \frac{b}{2f\Pi}\frac{1 - \mu cos^2\alpha}{(1+\mu)cos\lambda}(ln\frac{h_c}{b} + 1), \tag{15}$$

whereas b is the relevant Burger's vector, μ is the Poisson's ratio, f is the mismatch strain, and α is the angle between the burger vector and the dislocation. λ is the angle between the slip direction and the direction in film plane perpendicular to the line of intersection of the slip plane and the interface [35].

Few years ago, it was hard to believe the production and commercialization of high-quality devices with such materials. Nevertheless, taking advantage of the progress in addressing some of the growth issues of III-N materials, combined to their unique properties, significant progress in advanced III-N research was achieved. The breakthrough includes the strain engineering solutions and the progress in the development of native GaN substrates, which can not be only seen as a research curiosity anymore. However, major technological challenges still remain in the development of high-performance devices. Some of them will be addressed within this study using novel boron-based materials.

1.2.4 Spontaneous and stimulated emission

The major processes governing the photon-electron interaction were reported for the first time by Einstein in 1917. The processes of the absorption and spontaneous and stimulated emissions of light, also referred as radiative recombination, are shown in Figure 11. The figure illustrates the case of two-energy levels E_1 and E_2 (for valence and conduction band). Radiative recombination occurs when a hole and an electron in the valence and conduction bands recombine. The excess energy leads to a photon emission.

Both spontaneous and stimulated emissions are of paramount importance in light-emitting devices. For instance, semiconductor lasers are based on the amplification of an optical wave through stimulated emission of photons. In contrast, spontaneous emission and absorption process are the fundamental modes of LEDs and solar cells, respectively.

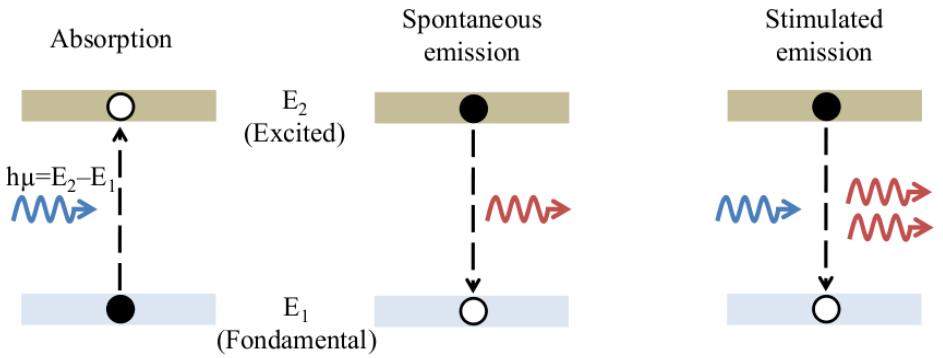

Figure 11: Energy band diagrams featuring different processes: (a) absorption, (b) spontaneous emission, and (c) stimulated emission.

In any two-energy levels system, a photon with energy E_{ph} = hμ equal to the material bandgap energy can be absorbed by an atom. Only photons with a specific wavelength can be absorbed. This absorption gives rise to an electron that was originally in a low energy state (fundamental state) to an upper energy level (excited state). This transition is also denoted "induced absorption" as it is induced by the incident light. Because of the limited lifetime of any excited state, which is typically less than 10^{-6}s, the electron remains a limited period of time in this excited state and then spontaneously returns to the equilibrium state. This process is connected to a photon emission with random phase and direction, and it is referred as the spontaneous emission. The emitted photon wavelength is the same than the material bandgap energy.

Despite spontaneous emission can not produce any light amplification, this emission is considered as a very important process. In fact, the process constitutes the first step in the stimulated emission, as the generated photon through the first process results in two photons. Similarly to the spontaneous emission, the excited atom can return to the fundamental state stimulated by its interaction with a photon of light. This process results in the emission of two photons that have a common wave vector (same frequency and same propagation direction). The emitted photon is said to be in phase with the incident wave. This feature ensures a fixed link between light radiated from different atoms in the amplifying medium and leads to the highly monochromatic and coherent

laser emission. Similarly to the absorption process, this phenomenon is a resonant process as the incoming photon has to have the same energy than the material bandgap. Additionally, both processes have the same probability, as shown by quantum theory [36]. In the thermal equilibrium conditions, the absorption process predominates. In fact, more atoms are present in the low-energy level E_1 (more stable) than in the excited-level E_2. To promote the stimulated emission rather than absorption, the reversed situation should exist. This uncommon condition, for which more atoms are present in the upper levels, is called the population inversion. This phenomenon is fundamental for laser action to occur [37], and it is realized by excitation of the system with continuous provision of energy through optical pumping or electric carrier injection. The laser oscillators use a small part of the spontaneous emission as the optical input and then amplify the fractions by the stimulated emission under population inversion.

1.3 VCSEL's principle and fabrication

1.3.1 VCSEL's principle

The typical layout of a VCSEL is illustrated in Figure 12. The structure is realized by sandwiching a light-emitting layer (i.e., a thin layer of semiconductor material with a large optical gain such as multiple quantum well structure [38, 39, 40]) between two highly reflective mirrors. The mirrors can be multilayered-dielectric or epitaxially-grown DBRs. The mirrors enable the generated photons in the active region to bounce fourth and back stimulating the emission of other photons from electron-hole recombination [41].

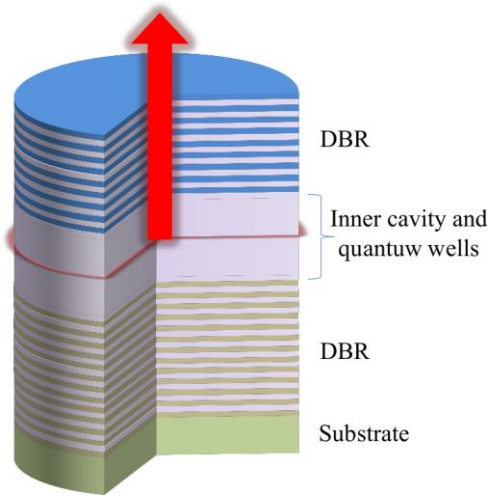

Figure 12: Schematic structure and operating principle of a VCSEL.

The basic physics governing the operation of VCSELs is not different from other laser diodes. Pumping is required to stimulate emission, which provides gain for the optical mode confined in the optical cavity [42]. Depending on the top or bottom emission, the conductivity and transparency of the layers forming the mirror stacks should be taken into consideration. As the name indicates, the light is emitted through the surface and not through the side facets as in edge-emitting lasers. Light emission will occur if the beam increases in intensity during a round trip. However, additional losses in intensity, including absorption, scattering, and reflections, can occur [43]. The lasing threshold is achieved when the gain exactly compensates for the losses.

The typical round-trip gain in a VCSEL cavity is in the order of a few percents (typically 2%). To reach the lasing threshold, the total cavity losses, including those induced by the mirrors, have to be maintained below this value. Consequently, the reflectivity of the DBRs should be greater than 99%.

1.3.2 VCSEL's fabrication

Toward the fabrication of nitride VCSEL in the UV range, two features are required. The first lies on the high current density in the active region to have an amplifier.

Consequently, the injected carrier density is high enough so that the absorption rate is lower than the stimulated emission rate. The second feature is related to the resonator. Low losses are required to guarantee a gain coefficient in the amplifier higher than the total losses during a round-trip in the cavity [34]. The active medium structure, where the light is generated, is introduced in next paragraphs.

The requirement of an active region in VCSELs is more stringent than in edge-emitting lasers because of the shorter gain region. This difference leads to high threshold gain and typically high thermal resistance [44] in VCSELs. However, this threshold current density of VCSELs can be minimized if the value of the differential gain g_N can be increased (Eq. 16) [45]. In fact, the differential gain can be largely increased by replacing bulk materials with QW structures.

$$g_N = a_N(N - N_{th}), \tag{16}$$

where a_N is the gain coefficient, N is the injected carrier density, and N_{th} is the carrier concentration at threshold.

Energy can be pumped into the active region in different forms, leading to a radiation energy. In fact, the active region generates the first photons (through spontaneous and stimulated emissions) that will balance between the top and bottom mirrors to generate other photons. In fact, as opposed to being directly emitted following electron-hole recombination, the photons are oscillating making several passes over the active medium [46].

To confine carriers in the active region, double-heterostructure is designed using a thin and small-bandgap layer between two large-bandgap layers. If the thickness of the small-bandgap layer is reduced to the range of de Broglie wavelength of the carriers, a quantum well will be formed. Therefore, the energy levels within the wells are quantized in discrete levels. Consequently, the radiative lifetime is shorter than in bulk materials and device radiative efficiency increases. In the case of QW, electrons and holes can only

move freely in two dimensions within the finite potential barriers that are determined by the band structure offset. Therefore, the well width and potential-barrier height are the main factors influencing the quantized energies [28].

The active medium of III-nitride based VCSELs is composed of $Al_xGa_yIn_{1-x-y}N$-based multiple quantum wells (x and y referring to the aluminum and gallium content, respectively). The function of the QW is to further enhance carrier confinement and allow for laser wavelength selection via the correlation between well dimensions and electron-hole recombination energies. The bandgap energy can be tuned to attain the desired wavelength depending on the composition of the different elements.

Figure 13 illustrates the schematic bandgap energy of an AlGaN/AlN MQW active layer. If the well width is much shorter than the length of VCSEL, the corresponding optical confinement of the QW Γ_w can be approximated by Equation 17.

$$\Gamma_w \approx \frac{n_w L_w}{L}, \tag{17}$$

where L_w and n_w are the thickness and the number of QWs, respectively. L is the VCSEL total cavity length.

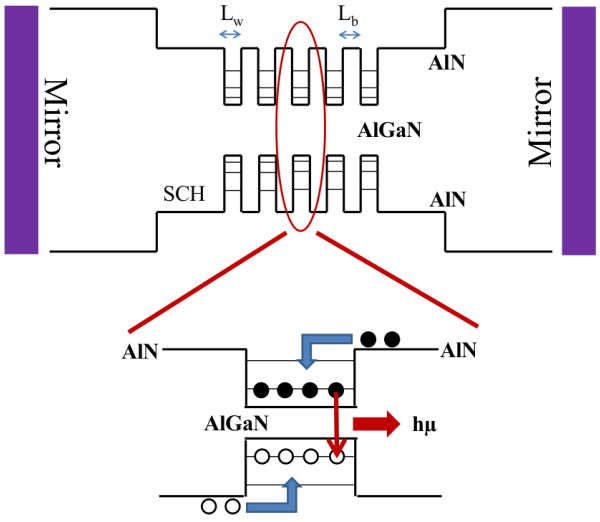

Figure 13: Schematic diagram of an AlGaN/AlN MQW with a separate confinement heterostructure.

To allow reflection to occur at the interfaces, the active layer has a lower bandgap and a higher refractive index than those of the surrounding materials. The generated photons can be therefore confined within the active medium to increase the probability of stimulated emission.

In principle, the light emission efficiency of QW depends on many factors: material quality, well and barrier width, and well and barrier band-offset (ΔE_C, ΔE_V). The number of QWs has to be optimized as a function of the round-trip losses. These QWs are therefore located optimally at the peak of the optical field. For an efficient radiative recombination [28], it is also required to approximate the well thickness to the dimension of the free-exciton.

An additional feature designers should consider when developing active region for light-emitting devices is the electron blocking layers. In fact, electrons and holes have different mobilities in nitride systems. Consequently, in contrast to holes which are often injected predominantly in the first quantum well, electrons are equally distributed in the active region. Electrons tend generally to overflow the MQW system. This electron diffusion should be minimized, as it does not contribute to the light emission in the active region. Therefore, the introduction of an electron blocking layer has proved to be an efficient solution to overcome this issue [47].

The shortest wavelength achievement of the different lasers and distributed Bragg reflectors will be discussed in next paragraphs.

1.4 State-of-the-art of DBRs and lasers operating in the UV Range

The different applications mentioned earlier have fueled the need for compact UV light sources. Toward the achievement of compact devices, wide-bandgap semiconductor (B,Al,Ga,In)N materials are undoubtedly the most suitable technology. Consequently, III-N materials have been extensively explored in the past decades toward their use in semiconductor devices.

ZnSe-based materials were the first material system to provide continuous wave (CW) operation of blue-green lasers [48]. However, serious reliability problems, possibly arising from its chemically and structurally unstable material system, have hindered the application of ZnSe lasers in the real-world systems. Moreover, because of its low bandgap, this material is not adapted to UV applications.

Later, $Al_xGa_yIn_{1-x-y}N$-based wide bandgap semiconductor material systems [49, 50] have brought innovative changes in photonic devices. These materials enabled the operating wavelengths of LEDs and lasers to reach a spectral range spanning from blue to UV [51].

From the first nitride-based injection laser demonstrated in 1995 [52], lasers have undergone tremendous evolution through the rapid progress in material growth, device fabrication, and packaging. Therefore, high-efficiency short-wavelength LDs covering the UV spectral range from 340nm to 360nm [18, 39, 53] were demonstrated with electrical injection. A number of advances are needed to develop short-wavelength devices. The advances include: 1) reduction of nonradiative defects in the QW active region, 2) improvement of AlGaN materials conductivity and p-type doping, and 3) the development of low-dislocation density materials [54, 55].

As mentioned earlier, VCSEL is an advanced configuration of LD which can offer several advantages over edge-emitting lasers [56, 57, 58]. One major feature is that VCSEL devices suffer less from dislocation issues than edge-emitting lasers. However, because of other limitations, so far, VCSELs can only operate in the visible and violet spectral range [59, 60]. The development of III-nitride-based VCSEL [61] includes optically-pumped devices at blue wavelengths [62], current-injected CW lasing blue VCSELs at 77K [63], and room-temperature CW lasing violet VCSELs by current injection [64].

A major technical challenge for the development of III-nitride VCSELs operating in the UV range lies in the need of highly reflective DBRs with large bandwidth and high

structural quality. AlN/GaN DBRs were employed to prove the existence of high reflectivity in the near-UV range (R > 99%). However, cracks appeared because of the large lattice mismatch [65]. $Al_xGa_{1-x}N$/GaN system was also used in an attempt to reduce the strain in the whole DBR structure [66, 67]. However, the reduced refractive index contrast leads to a reduced bandwidth (<20nm) and a large number of DBR periods to achieve high reflectivity. For example, $Al_{0.34}Ga_{0.66}N$/GaN DBRs require 35 and 43 pairs to achieve 96% at 390nm and 98% at 400nm of peak reflectivities, respectively [62, 68]. To manage strain, lattice-matched InAlN/GaN DBRs were proposed [69]. However, these structures suffer from the numerous temperature ramping processes during the growth.

All the DBRs mentioned earlier operate in the visible and near-UV range. However, these GaN-based structures cannot be used for UV-VCSELs because of the strong absorbtion in GaN materials. For the development of III-nitride DBRs operating below 380nm, AlGaN/AlGaN, AlGaN/AlN, and AlGaN/InAlN structures have been studied with an aluminum concentration adapted to the DBR working wavelength. A 29-pair $Al_{0.43}Ga_{0.57}N$/AlN DBR on AlN template substrate was designed to achieve a peak reflectivity of R ~ 99% at λ ~ 356nm [69]. A crack-free 25-pair $Al_{0.18}Ga_{0.82}N/Al_{0.8}Ga_{0.2}N$ DBR on GaN template was reported to have a peak reflectivity of 99% at λ ~ 350nm [70]. A 35-pair $Al_{0.2}Ga_{0.8}N/In_{0.15}Al_{0.85}N$ DBR on $Al_{0.2}Ga_{0.8}N$ template was reported to achieve a reflectivity of R ~ 99% at λ ~ 345nm [71]. To date, the highly reflective DBRs (> 95%) realized for UV applications are only centered at λ > 340nm. The wavelength limit is imposed to avoid internal absorption while maintaining high refractive index contrast. For short-wavelength DBRs, high Al mole fraction is required in both materials comprising the DBR pair to prevent wavelengths to be absorbed by the AlGaN layers. However, this feature results in a reduced refractive index contrast. To our knowledge, only few studies have reported functional DBRs with peak reflectivities below 340nm [16, 72]. C.G. Moe *et al.* have demonstrated the shortest wavelength reflectivity for a

DBR using 10 and 21 pairs of AlGaN/AlN with peak reflectivities of 66% and 82% at 245 and 279 nm, respectively [16]. X.L. Ji *et al.* reported a 30-pair $Al_{0.43}Ga_{0.57}N$/AlN DBR with a 93% reflectivity centered around 313nm [72]. The DBR reflectivities as a function of the wavelength for AlN/GaN [73, 74, 75], AlGaN/GaN [66, 68], AlGaN/AlN [16, 72], AlGaN/AlGaN [70, 76], and AlInN/AlGaN [71] systems are summarized in Figure 14.

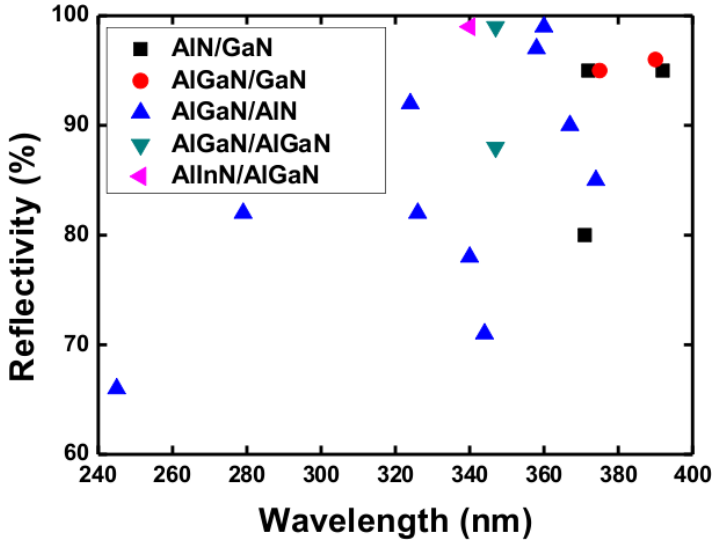

Figure 14: DBR reflectivities as a function of wavelength for various nitride systems.

As a conclusion, it is proved to be challenging to achieve highly reflective DBRs in the wide spectral range of UV wavelengths, with the conventional material technologies. Consequently, the development of new materials technology is required. Therefore, we propose to introduce boron-based materials as an alternative to conventional materials to combine high reflectivity and large bandwidth in the UV range.

1.5 Technical challenges limiting the development of UV VCSELs

Conversely to infrared and visible VCSEL, the development of VCSELs emitting in the UV range is a very challenging milestone because of several issues associated with their fabrication. The issues are related to materials quality, highly reflective DBRs, optical

confinement, carrier injection, and the lack of lattice-matched substrate. Such issues are briefly discussed in next paragraphs.

As mentioned earlier, III-N alloys have emerged as the leading and the most adapted materials for VCSEL devices in the UV region because of their remarkable physical properties and their bandgap flexibility. Toward the achievement of UV VCSELs, the development of high-quality (crack-free and low threading-dislocation density) III-N materials is fundamental. In fact, in the case of low-quality materials, lasers experience non-radiative recombination. This feature leads to heating problems and consequently to a significant increase of the lasing threshold.

An impediment in the development of high-performance devices based on III-N materials is the lack of lattice-matched substrates. Despite the intensive research investigating alternative substrates such as silicon (Si), Silicon Carbide (SiC), Lithium niobate (LiNbO3), zinc oxide (ZnO), and others, sapphire is undoubtedly the most used substrate because of its availability and low cost. However, the large difference in lattice parameters between sapphire and III-Nitrides has a detrimental effect on the structural and morphological quality of the heteroepitaxially layers. The thickness of the epitaxial mirror is therefore limited. Additionally, sapphire is insulating, which prevents efficient backside contact. Consequently, providing bulk GaN and AlN substrates to grow nitride materials is fundamental for UV VCSEL development. However, the technology is not mature yet and their high price and small size are currently major obstacles.

In addition to the previously reported issues, the development of UV VCSELs is still hampered by some doping issues. In fact, in opposition to n-type doping for AlGaN layers which is straightforward using silicon as typical n-dopant, the p-doping using magnesium is still considered to be challenging. In fact, important Al-content suffer from high contact resistance and issues with current spreading. Different approaches were applied to achieve p-type III-nitrides by Mg doping such as co-doping, delta doping [77], and valence-band modulation using strained superlattice structures. However, p-type

doping is not mastered yet. As a consequence of the poor conductivity of p-type AlGaN alloys, the electrical injection remains challenging in the UV region.

To reach the lasing threshold, minimizing the losses and maximize the gain in the active region is needed, which requires a good optimization of the optical quality of the quantum wells. In fact, enormous enhancement in the gain can be achieved by replacing the bulk active layer with QWs. However, the optical quality of the active region is still considered critical in the VCSEL structure operating in the UV range. To achieve sufficient gain in the cavity, VCSELs also need highly reflective DBRs exceeding 99%. To date, among nitride materials, the $Al_xGa_{1-x}N/Al_yGa_{1-y}N$ system was the most reported candidate for functional UV DBRs [69, 72]. However, the DBR design has to comply with an intricate trade-off between the limited refractive index contrast, the transparency of the AlGaN layers, and the in-plane lattice mismatch AlGaN/AlN. In fact, the AlN/GaN system exhibits a lattice mismatch as high as 2.4%, while the refractive index variation does not exceed $\Delta n=0.5$. The AlGaN refractive index versus photon energy for different Al compositions is shown in Figure 15 [5]. As a matter of fact, below 300nm, a large aluminum content-contrasted structure would benefit from a large refractive index contrast at the expense of high absorption in the AlGaN layers. Additionally the structural quality of the materials will be affected by the large lattice mismatch. Consequently, most of the demonstrated $Al_xGa_{1-x}N/Al_yGa_{1-y}N$ DBRs suffer from cracks [72], rough interface, and/or limited reflectivities with narrow stopband widths [16, 65]. In addition to their detrimental effect on the reflectivity, the cracks make the device processing very challenging. To overcome these issues and reduce the strain in the whole structure, researchers have recently reported nearly lattice-matched AlInN/AlGaN DBRs to achieve highly reflective DBRs in the UV region [71, 78, 79]. However, the AlInN-based DBRs are time-consuming and difficult. This is explained by the numerous temperature ramping processes during the growth and the sensitivity of In incorporation to the growth temperature [80].

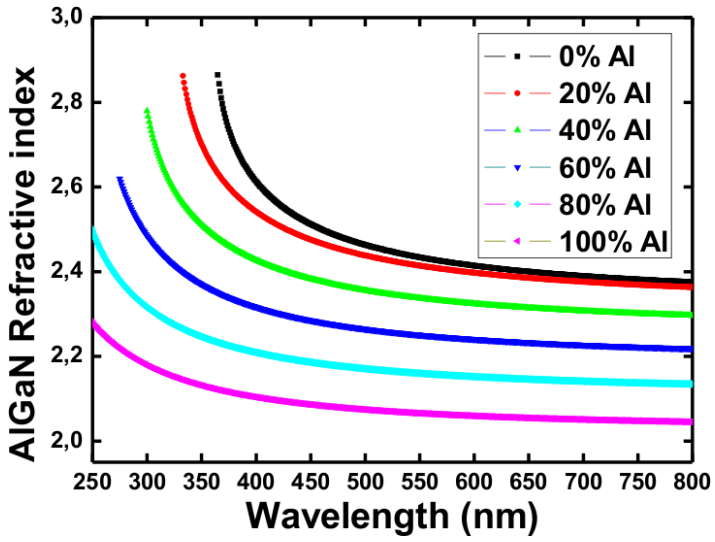

Figure 15: Refractive index versus wavelength for $Al_xGa_{1-x}N$ alloys (adapted from ref [5]).

Another limitation that has to be taken into consideration when designing DBR structures in the UV region is the DBR bandwidth. This parameter will be deeply described in Section 3.1. DBRs are characterized by their high selectivity. This selectivity is considered to be an advantage when it is about filters. However, in VCSEL devices, it is considered a main drawback as the high reflectivity is only reached in a wavelength range called "stopband", and it falls dramatically outside. Consequently, photons with an incident angle falling outside the stopband are not properly reflected, which limits the maximum extraction efficiency. They are referred as the "leaky modes". Therefore, it is fundamental to have a large refractive index contrast Δn to obtain a sufficient bandwidth.

As a result of the several listed issues and especially the difficulty to fabricate highly reflective DBR with large bandwidth in the UV range, the development of VCSEL devices operating in this region has proved to be challenging. In this work, the main objective is to investigate highly reflective DBRs.

1.6 Scope of this dissertation

The purpose of this dissertation is to investigate the MOVPE growth of group III-nitrides BAlGaN materials system for their incorporation in the main building blocks of VCSEL devices. The research work described in this dissertation is organized as follows:

The history of the research, the important aspects of group III-nitride materials properties, the motivation, and applications of UV VCSELs have been addressed in this chapter. An overview of the state-of-the-art of DBR structures and VCSEL in the UV range was also covered.

Chapter 2 deals with the principle of MOVPE system employed in this study and an overview of the different growth conditions and equations governing the nitrides growth. It also covers a description of the different characterization tools used in this study.

In the beginning of Chapter 3, the focus will shift to the description of the distributed Bragg reflectors. The different simulations and software developed within this study will also be outlined in this chapter.

Chapter 4 will be devoted to the complete discussion of the epitaxial growth of the different III-N materials and their optical and structural characterizations. The chapter starts with the conventional AlGaN materials, then the boron-based materials will be presented. The demonstrated optical properties of the boron-based materials motivate their possible use in the distributed Bragg reflectors operating in the UV range.

Chapter 5 will present the distributed Bragg reflectors using different III-N alloys. The boron-based structures will be deeply investigated and compared to conventional AlGaN stacks.

Finally, the dissertation concludes with Chapter 6 through a summary of the different results achieved and a discussion of potential future research work.

CHAPTER 2

PRINCIPLE OF MOVPE AND CHARACTERIZATION TECHNIQUES USED IN THIS STUDY FOR III-N MATERIALS

As discussed in the previous chapter, the III-N materials system has been shown to be an excellent candidate for solid-state lighting. Early investigation of the III-Nitrides was made at the beginning of the 20th century with the first tentative of AlN, GaN, and InN growth by Tiede in 1928 [81], by Johnson in 1932 [82], and by Juza and Hahn in 1938, respectively [83]. For instance, GaN was mostly obtained in the form of small needles and platelets by passing ammonia over hot gallium metal [82]. Few decades later, large area GaN was grown directly on sapphire by Maruska and Tietjen [84]. As these GaN layers suffer from very high background electron concentrations, further optimization was paramount and conducted to Yoshida's idea [85] to use an AlN intermediate layer. The process was then improved by Akasaki and Nakamura by using AlN and GaN nucleation layer grown at low temperature prior to the growth of high temperature nitride films [86, 87]. P- and n-type doping were also very important breakthrough for today's optoelectronics devices. Following the success of the III-N materials growth and doping, Nakamura's team demonstrated in the nineties the first high-brightness blue LED and UV LD [88].

Different techniques can be used to epitaxially grow semiconductor materials. One major technique is molecular beam epitaxy (MBE) which was invented in 1960 at Bell Laboratories by J.R. Arthur and A.Y. Cho [89]. The first growth of AlN and GaN single crystals using MBE was reported by S. Yoshida et al. at the Electrotechnical laboratory in Japan in 1975 and 1983, respectively [85, 90]. Taking advantage of its simple process, good uniformity, and abrupt interfaces, the technique was extensively

investigated in the following years. However, MBE has few limitations such as its low growth rate and its cost.

Hydride vapor-phase epitaxy (HVPE) is another modern growth technique for nitride compounds initiated by Maruska and Tietjen to grow the first GaN in 1969 [84]. This technique is amongst other widely used today to grow low dislocation density GaN substrates for overgrowth. However, this technique suffers from its complex process/reactor, the difficulty to have an accurate and reproducible composition control in nitride alloys layers, and the hazardous precursors it uses.

One additional major technique is MOVPE, which is an evolution of the HVPE technique. MOVPE technique was pioneered by Manasevit in 1968 who successfully demonstrated the deposition of several various materials onto semiconductors and insulators, such as GaAs, GaP, GaAlAs, AlN, and GaN [91, 92]. MOVPE technique has different drawbacks such as the toxicity and the spontaneous flammability of most precursors in contact with air. As not all the precursors molecules are converted during the growth, hazardous and flammable substances are merged to highly explosive hydrogen and then leave the reactor. Therefore, it is fundamental to filter, neutralize, and purify the mixture before it can be passed into the exhaust air [34].

Despite all the disadvantages explained above, thanks to various strengths, the MOVPE technique unquestionably displaces the other techniques in optoelectronic devices. The advantages include the versatility, the high growth rate of all III-V and II-VI semiconductor compounds, and the suitability for large-scale production. MOVPE has also proved to be the most economical technique, particularly for the production of devices requiring large areas, such as LEDs, photodetectors, transistors, and solar cells. Consequently, all the material and device structures developed during this thesis have been grown using MOVPE technique.

Various kinds of ex-situ characterization techniques are afterward required for proper understanding of the grown material and device, thereby, improving performance

of devices and increasing the yield. Therefore, the application of a desired structural, optical, chemical, and morphological characterization to each growth is critical. X-ray diffractometry (XRD) is performed to investigate a and c lattice parameters, relaxation, and structural quality. The surface morphologies and topographies are observed by scanning electron microscopy (SEM) and atomic force microscopy (AFM). Cathodoluminescence (CL), photoluminescence (PL), and ellipsoemtry are studied to characterize the optical properties. Fourier transform infrared spectroscopy (FTIR) and spectrophotometry were employed to measure the reflectance, transmittance, and absorption.

To investigate the microstructure in cross-section, the dislocation density, and interface quality, transmission electron microscopy (TEM) was applied. Secondary ion mass spectrometry (SIMS) and X-ray photoelectron spectroscopy (XPS) were finally performed to identify the different element incorporation and a quantitative measurement for boron content in III-N systems.

In this chapter, the basic principle of MOVPE will be discussed with an overview of the different III-N growths. The different characterization techniques employed in this study are described in the following sections.

2.1 Metalorganic vapor-phase epitaxy

2.1.1 The basic principle of MOVPE

The four basic building blocks for MOVPE systems are: (1) gas handling system, (2) reaction chamber where the growth takes place, (3) heating system, and (4) an exhaust and low pressure pumping system.

Different organometallic (OM) precursors in the gaseous form are introduced through a carrier gas into a reaction chamber containing a heated wafer. When the different precursors reach the substrate, they are decomposed. This thermochemical decomposition is called pyrolysis and leads to a sequence of chemical reactions between

the different species, which results in the deposition of thin layers. During the growth, the substrate is positioned on a rotating susceptor to enhance the layer homogeneity.

The metalorganic precursors exist in either liquid or solid form and are stored in an all welded stainless steel containers, commonly referred to as "bubblers", which are maintained in a bath at a constant temperature. Equation 18 illustrates the dependance between the equilibrium vapor pressure of metalorganic precursor and this bubbler temperature.

$$P_{sat} = 10^{(a-\frac{b}{T})}\frac{1013.25}{760}mbar, \tag{18}$$

where T is the bubbler temperature and a and b are the metalorganic precursor vapor pressure parameters. The different parameters leading to the vapor partial pressure of the different metalorganic precursors as a function of temperature is given in Table 4.

Table 4: Properties of group III precursors.

Precursors	a/b	Melting point(°C)	Boiling point(°C)
Trimethylgallium (TMGa)	8.07 / 1703	-15	56
Trimethylaluminum (TMAl)	8.22 / 2135	15	125
Trimethylindium (TMIn)	10.52 / 3014	88	134
triethylboron (TEB)	$log(P_{sat}) = 7.413 - \frac{1544.2}{T-27.42}$	-93	95

The flow of the appropriate metalorganic precursor molecules is achieved by passing a carrier gas (hydrogen or nitrogen) through the bubblers. It is fundamental that the precursors exhibit an appropriate volatility to enable a thermal decomposition in the growth chamber. The process is usually performed at a reduced pressure and the growth chamber's wall is cooled using cold water. The molar quantity of metalorganic compound

entering the chamber is governed by the bubbler temperature, the bubbler pressure, and the flow rate of carrier gas through the bubbler.

As mentioned earlier, the carrier gas can be either hydrogen or nitrogen. Excepting InGaN growth in which the presence of hydrogen is detrimental to the growth, (B,Al,Ga)N systems can use both gases. Hydrogen presents several advantages in comparison to nitrogen carrier gas such. For instance, the beneficial thermal conductivity and carbon-radical scouring properties make hydrogen very widely used. Most of the growth performed in this work used nitrogen as carrier gas, because hydrogen system was only installed few months ago.

2.1.2 Description of the used precursors

Trimethylgallium (TMGa or $Ga(CH_3)_3$), trimethylaluminum (TMAl or $Al(CH_3)_3$), triethylboron (TEB or $B(CH_3CH_2)_3$), and trimethylindium (TMIn or $In(CH_3)_3$) are commonly used as group III precursors in the III-Nitride epitaxy system. Triethylgallium (TEG), which has a much lower vapor pressure than TMGa, can also be used to produce Ga molecules. For instance, it can be used for quantum well structures, for which accurate thickness control is required.

All the precursors sources listed above are very air sensitive, which means they ignite spontaneously upon contact with air. In opposition to TMIn which is sublimate solid, TMAl, TEB, and TMGa are liquid sources at room temperature. The melting and boiling points of the different III element precursor sources are summarized in Table 4, and their molecular structures are presented in Figure 16. Because of the large difference between their atomic properties such as atomic radius, ionization energy, and electron affinity, the chemical properties of Ga/Al/In/B compounds are very different from each other.

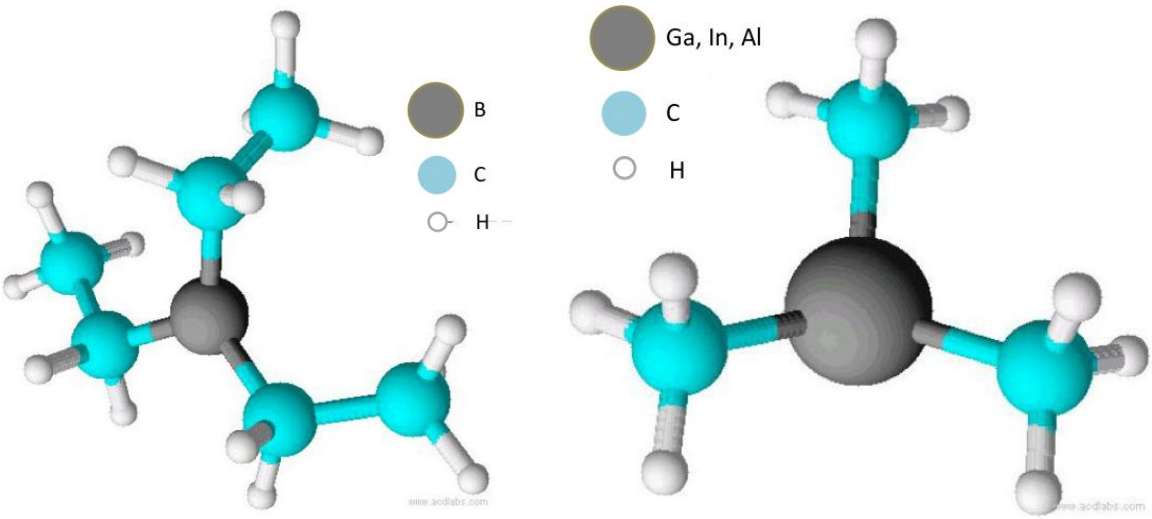

(a) (b)

Figure 16: Molecule representation of (a) TEB and (b) TMGa, TMAl, and TMIn.

The extremely low dissociation rate by the order of 10^{-16} of the dimer molecule of nitrogen at high temperatures limits the use of nitrogen as a group V precursor [93]. There are several nitrogen sources such as Dimethylhydrazine (DMHz) and Hydrazoic acid (HN_3). However, ammonia (NH_3) is unquestionably the most common source because of its decomposition rate of 4% up to 950°C [94]. As a direct consequence of the low ammonia cracking efficiency, a large amount of NH_3 has to be introduced for (B,Al,Ga)N growth (typical V/III ratio is 2000). In the case of GaN growth, when the pressure is too low, a Ga liquid phase can be formed, which leads to droplet formations in the surface [95].

2.1.3 MOVPE growth of III-Nitrides

To carry the different reactants, the carrier gas flows through two separate III and V run lines. The use of two separate run lines is fundamental since the OM sources used as column III precursors are Lewis acids; whereas ammonia, the primary column V source,

is basic [96]. Therefore any pre-mixing between the two sources leads to gas-phase reactions which are detrimental to the film growth process [97].

The general reaction to grow group III-Nitride layers is described by Equation 19.

$$R_3M + NH_3 \Longleftrightarrow MN + 3RH. \tag{19}$$

In this equation, R is an alkyl group, and M represents the group III metal such as gallium (Ga), aluminum (Al), boron (B), or indium (In). H is hydrogen, and N represents the group V element, which is nitrogen for our case. The general reactions for GaN, AlN, and AlGaN growth using TMGa, TMAl, and NH_3 can be expressed by the following equations.

$$(CH_3)Ga(g) + NH_3(g) \Rightarrow GaN(s) + 3CH_4(g). \tag{20}$$

$$(CH_3)Al(g) + NH_3(g) \Rightarrow AlN(s) + 3CH_4(g). \tag{21}$$

$$(x)(CH_3)Al(g) + (1-x)(CH_3)Ga(g) + NH_3(g) \Rightarrow Al_xGa_{1-x}N(s) + 3CH_4(g). \tag{22}$$

The MOVPE process is very complex with many parallel and series reactions steps. The growth process can be categorized into four processes: gas input, pyrolysis, diffusion, and surface reaction [28]. During the growth, different species diffuse in the carrier gas and are pumped away from the deposition zone towards the reactor exhaust. The schematic illustration of GaN epitaxial growth is illustrated in Figure 17.

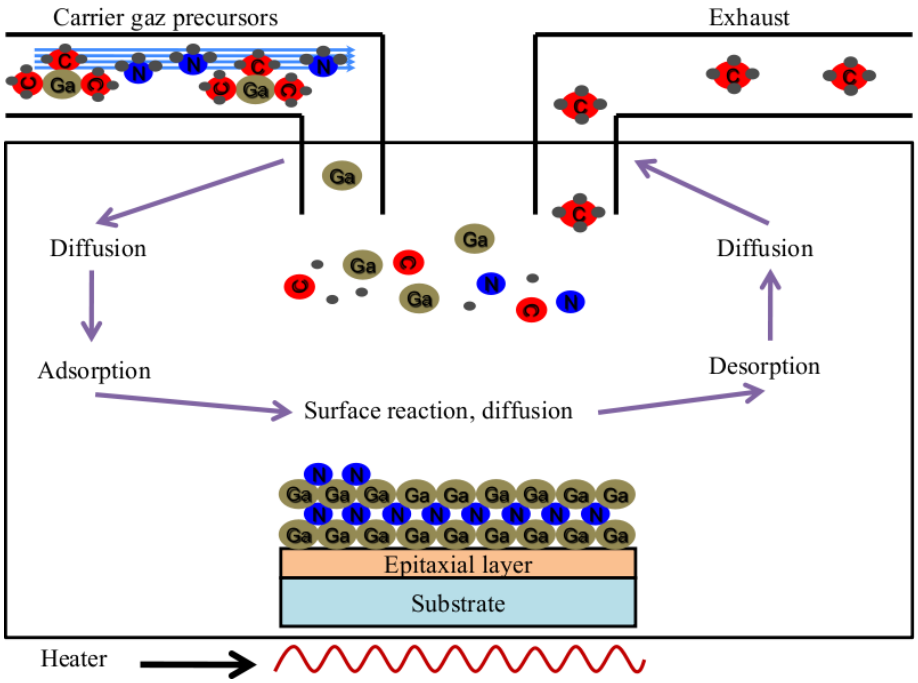

Figure 17: The schematic illustration of GaN epitaxial growth.

2.1.4 Description of the used MOVPE and in-situ reflectometry tool

All epitaxial materials and structures studied within this work were grown by MOVPE using a home made reactor system built by Prof. Abdallah Ougazzaden [98]. The T-shaped low pressure MOVPE reactor was installed in 2004. It was dedicated to classical III-V materials such as InP and GaAs, for which the temperature does not exceed 700°C. The MOVPE growth chamber has been reconfigured to reach the required temperature for wide bandgap III-N materials exceeding 1000°C. N_2 and H_2 can be used as carrier gases and TMAl, TMGa, TEB, and TMIn as sources of aluminum, gallium, boron, and indium, respectively. The gas panels were also upgraded to allow p-type and n-type doping. Biscyclopentadienyl magnesium (CpMg) and disilane (Si_2H_6) are available as precursors for Mg and Si, respectively. The growth temperature ranges from 400 to 1100°C, and the growth pressure can be varied between 75 and 750 Torr.

Pictures of the MOVPE system and the growth chamber are shown in Figure 18.

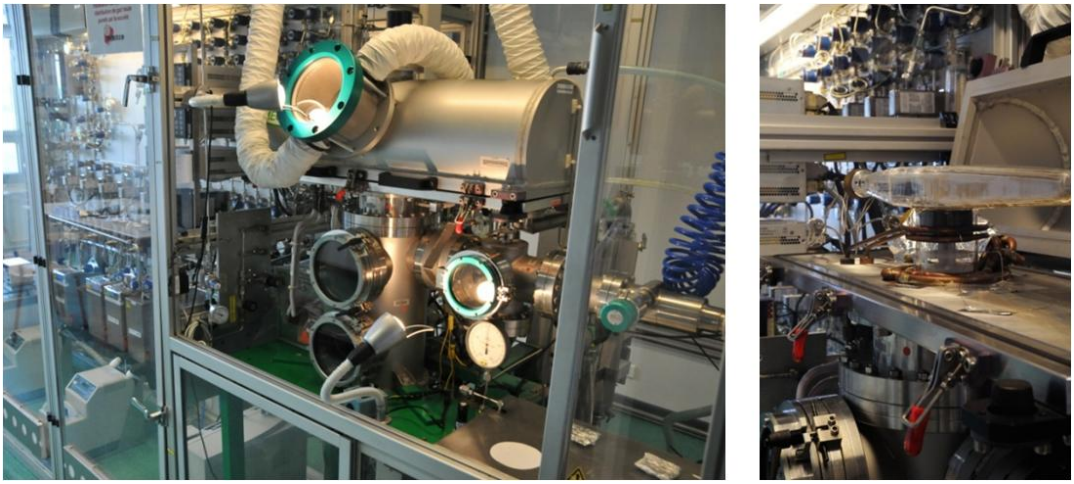

Figure 18: MOVPE setup and growth chamber.

The MOVPE system was also equipped with a home-built in-situ optical reflectivity monitor to provide accurate information on the growth rate and quality. The interference of two light beams reflected from the growing epilayer surface is detected by an optical detector. The light source used in our case is a laser with an emission wavelength of 670nm. Equation 23 illustrates the epilayers growth layer and thickness.

$$nd = m\frac{\lambda}{2}, \tag{23}$$

where λ is the laser wavelength, m is an integer, n is the layer refractive index at the growth temperature, and d is the thickness for which the maximum of Fabry-Perot oscillations occurs. The growth rate can be accurately calculated from the interval Δt between two maxima, as shown in Equation 24.

$$Growth\ Rate = \frac{\lambda}{2n\Delta t}. \tag{24}$$

As mentioned earlier, in-situ reflectometry oscillations are good indicators of the layer morphology. In fact, the intensity of reflectance measurements may be affected by the optical properties of the substrate or the growing layers and the growth conditions during the heteroepitaxy. For instance, the increase in surface roughness during the

epitaxy can be illustrated by a decrease in both maxima and minima of reflectance. In-situ reflectometry curve for a 900nm GaN growth is shown in Figure 19.

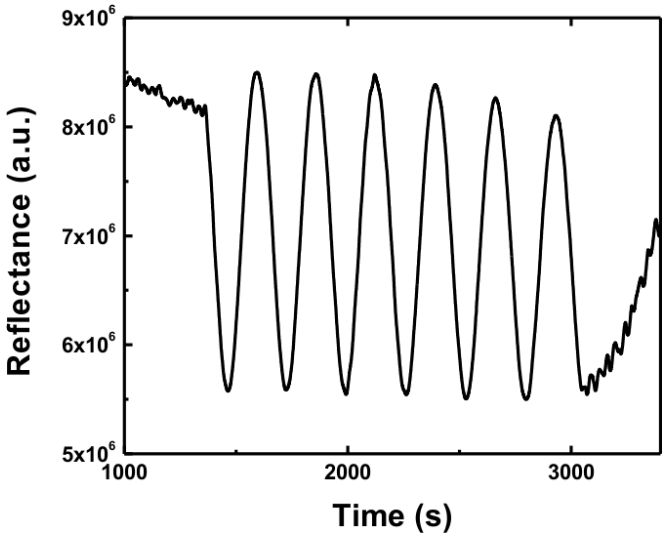

Figure 19: In situ reflectometry for a 900nm GaN film.

One of the key parameters during the epitaxial growth is the growth temperature. The growth temperature can affect the composition of ternary and quaternary alloys, the growth rate, the surface roughness, and the structural materials quality. Therefore, careful monitoring and accurate control of the growth temperature during the growth is fundamental. Consequently, the temperature is monitored by thermocouples.

2.2 Structural characterization techniques

X-Ray Diffraction: X-ray diffractometry is a non-destructive ex-situ technique giving accurate characterization of the structural properties of III-nitride layers. The basic principle of X ray diffraction is described by the dynamical theory of diffraction [99]. The tool is based on the diffraction patterns of the reflected X-ray beam after its interaction with a crystalline sample. This technique allows an accurate analysis of lattice parameters, alloys composition, thickness and uniformity of epitaxial layers, built-in strain, relaxation, and crystalline quality [100].

Our laboratory is equipped with High Resolution X'Pert PRO MRD (Material Research Diffractometer) from PANalytical. It is provided with a Cu-scaled anode in line-focus, hybrid monochromator consisting of a mirror and a 2-bounce channel Ge(220) crystal delivering a high intense $K_{\alpha 1}$ radiation (λ = 1.5405A), and a secondary optics plus detector. The hybrid monochromator delivers a beam with a height of 1.2mm and a resolution of ~ 12 arc sec. The height is adjusted with slits according to the size of the sample. Figure 20 illustrates the diffractometer movements where ω and 2θ are the incident and diffraction angles.

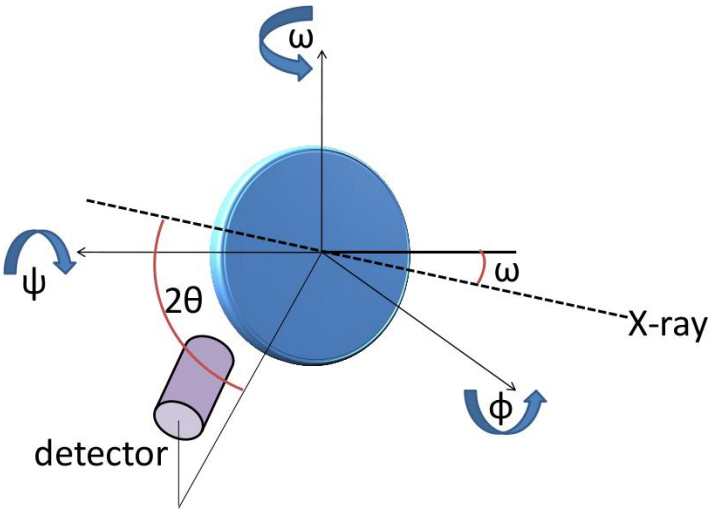

Figure 20: Angles associated with the diffractometer movements.

The Bragg's law (Equation 25) describes the diffraction of X-rays by different crystallographic planes in a crystal.

$$n\lambda = 2d_{hkl}\sin(\theta_B), \tag{25}$$

where d_{hkl} is the spacing between the lattices planes, (hkl) are the miller indexes presented in Chapter 1, θ_B is measured between the direction of the incident beam and the lattice plane under consideration, λ is the wavelength of the X-ray source, and n is an integer describing the order of diffraction. Figure 21 illustrates the X-ray diffraction at the Bragg wavelength in the case of parallel planes to the surface.

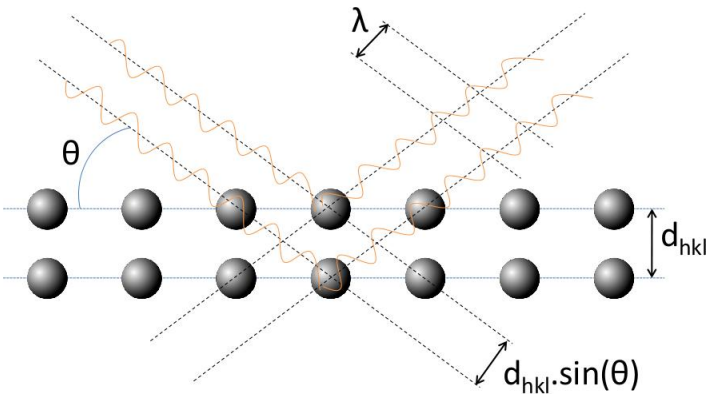

Figure 21: X-ray diffraction at the Bragg wavelength: the planes are parallel to the surface.

Each structural defect, dislocation, or alloy non-homogeneity in the crystal creates a local misorientation of the atomic planes, which slightly perturbs the broadness of the XRD peak. Consequently, the full width at half maximum (FWHM) of the diffraction peak gives a qualitative indication about the defect concentration in the crystal. This measurement is called the rocking curve (ω-scan). For group III-Nitrides, large degrees of mismatch exist. Therefore, rocking curve can be used to determine the relative crystalline quality of the different alloys [46].

For large lattice mismatch systems, one major limitation of the rocking curve is the reduced angular range, which can be transcended by performing ω- 2θ scans. In this diffraction condition, the detector moves at twice the angular rotation rate of the sample so that the measured diffraction angle remains equal to the incident beam angle [46].

Conversely to the rocking curve, reciprocal space maps (RSM) is performed [95] to separate the moscaicity (variation in ω) and lattice strain (variation in ω/2θ). The reciprocal space is basically a three-dimensional (3D) Fourier transform of the real space periodicity. This technique is categorized into two measuring types: an asymmetric RSM calculates both a and c lattice constants, while a symmetric RSM contains information about the crystalline quality of epitaxial films [26]. Figure 22 illustrates the observed tendencies of a diffraction peaks movement in the AlGaN system growth on GaN

substrates (symmetric plan (11.4)). The results give an accurate information on Al incorporation and relaxation.

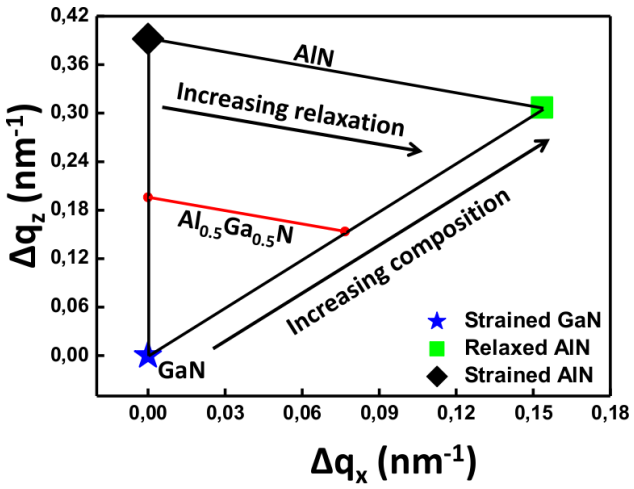

Figure 22: Influence of the relaxation and Al incorporation in the AlGaN system for (11.4) plan.

Transmission electron microscopy: TEM is a microscopy technique whereby a beam of electrons is transmitted through an ultra thin specimen. The interaction of the transmitted electrons forms an image with a significantly high resolution to examine details such as lattice defects in crystals and the interfaces quality in heterostructures.

After sample preparation performed by FIB (focused ion beam) at IEMN (Lille, France), all the TEM images presented in this work were performed using Philips CM20 transmission electron microscopy. All the samples were performed by Gilles Patriarche at LPN (Paris, France). The basic components of TEM are: the magnetic lenses, the diaphragms, and the phosphorescence screen. The system is equipped with a tungsten filament for electron emission into the vacuum by connection with high voltage source to accelerate the sources (typically 200 kV). In high resolution mode, it is possible through this microscope to enlarge the image up to 750000 times. The images are recorded digitally by CCD camera.

The system operates in either diffraction or imaging mode. The most used mode is imaging condition which selects and projects the image plane (located at the diaphragm

area) on the screen. In the diffraction mode, sometimes called "selected area diffraction", we look at the image formed in the focal plane of the objective lens. The diffraction pattern of electrons is projected on the screen using the projector lenses and yields a diffraction pattern of the sample.

The TEM system is noticeably combined with an energy dispersive X-Ray (EDX) spectroscopy allowing a chemical characterization and a quantitative compositional analysis in the case of ternary or quaternary alloys.

2.3 Imaging techniques

Nomarski optical microscopy: In this work, the Nomarski microscopy was used to investigate the layer morphology and observe cracks and defects. The main components of a basic light microscopy are: a light source to illuminate the sample, a nose piece to hold the different objectives used in changing the viewing modification, an aperture diaphragm to adjust the resolution and contrast, a field diaphragm to adjust the field of view, ocular lenses for magnification, and a sample stage manipulation [2].

The system uses the principle of interferometry of polarized light, which is laterally divided by a differential interference contrast (DIC) prism into two orthogonal light packets. These light packets hit the sample at two different positions and are then reflected and return to the prism through different paths. The differences between both reflected packets produces interference contrasts in the image [28]. Features such as surface defects, etch pits, and cracks can be clearly observed. The theoretical resolution R of an optical microscope is given by Equation 26 [101]:

$$R = \frac{0.61\lambda}{n\sin(u)}, \tag{26}$$

where n is the refractive index of the medium between the sample and objective, 0.61 is a coefficient associated with the Fraunhofer diffraction, λ is the wavelength of radiation, and u is the objective aperture. The resolution difference between optical and electronic

microscopy lies in the difference between both wavelengths. In fact, $\lambda_{photon} \approx 500$nm and $\lambda_e \approx 0.001$nm, which lead to $R_{photon} \approx 500$ nm and $R_e \approx 0.2$nm, respectively.

Nomarski microscopy is typically used to investigate the sample surface morphology. To investigate deeply the surface topography, the roughness, dislocation propagation, and different other features, scanning electron microscopy, atomic force microscopy and transmission electron microscopy should be performed.

Scanning electron microscopy: The high-resolution SEM images the sample surface by scanning it with a high-energy beam of electrons rather than light (optical microscopy). In addition to its large depth of field, SEM enables analyzing at nanometric scale the morphological and structural properties. The properties include growth mode, default density, and dislocation behavior. SEM also allows an accurate observation of wide bandgap materials such as BAlGaN alloys by using low accelerating voltages and the possibility to use a variable pression mode. Owing to its high resolution (1nm at 15KV), this equipment is also suitable for nano-material and devices.

Our model ZEISS Supra-TM 55/55 VP/55WDS with GEMINI COLUMN from Carl Zeiss SMT-Nano technology systems division offers the highest resolution available today. The main features of the instrument are an electron column containing the electron source (Figure 23) and the magnetic focusing lenses, the sample vacuum chamber, and the electronics console forming the control panel. The basic principle will be detailed in the following paragraph.

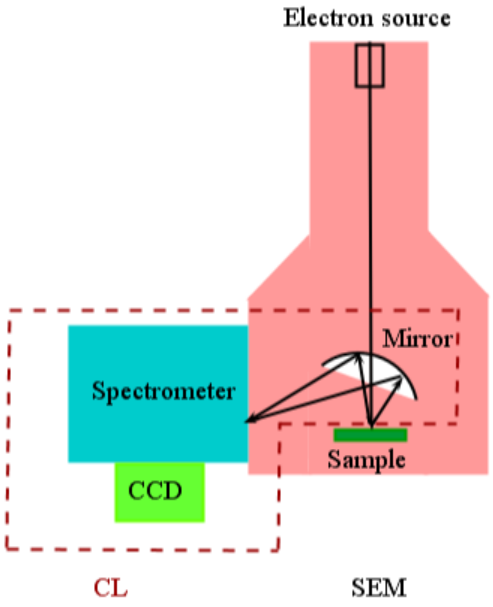

Figure 23: Scanning electron microscopy and cathodoluminescence systems.

A beam of electrons is produced by the electron source, also referred as the gun, by heating a metallic filament. The electron beam passes through the different lenses to focus the beam down towards the sample. When the primary electron beam hits the sample, the electrons lose energy by repeated random scattering and absorption. The interaction volume depends noticeably on electron's landing energy and the atomic number and density of the sample. After hitting the sample, high-energy electrons (backscattered or secondary) are ejected from the sample. These electrons are then collected by specialized detectors which convert them to a signal. The signal is then sent to a viewing screen producing the observed image [102].

A Jobin-Yvon cathodoluminescence system has been recently developed, and was mounted in SEM. Cathodoluminescence spectroscopy has emerged as a powerful tool for the micro-characterization of the electronic properties of luminescent materials. Major applications of CL include materials electronic band structures, measurements of the dopant concentrations and the minority carrier diffusion length, mapping of defects and densities, and analysis of stress distribution in epitaxial layers.

The CL spectroscopy is analogous to PL system (developed later). The atoms of a sample material are excited to a higher-energy state and then return to a lower-energy state or an equilibrium state by emitting that excess energy through a photon. One major difference is that the excitation energy is an order of magnitude higher for CL and slightly higher for PL than the luminescence energies. The difference in energy between the excited and equilibrium states is related to the energy of the emitted light.

Atomic force microscopy: Atomic force microscopy is a non-destructive technique which has been invented by G. Binning, C.F. Quate, and Ch. Gerber in 1986. AFM is typically used to observe high resolution tridimensional topographical analysis of a surface. AFM capabilities include 3D surface topography, detection of atomic scale features, surface roughness analysis, and defect study [103, 104]. A block diagram of the different components of an AFM is illustrated in Figure 24.

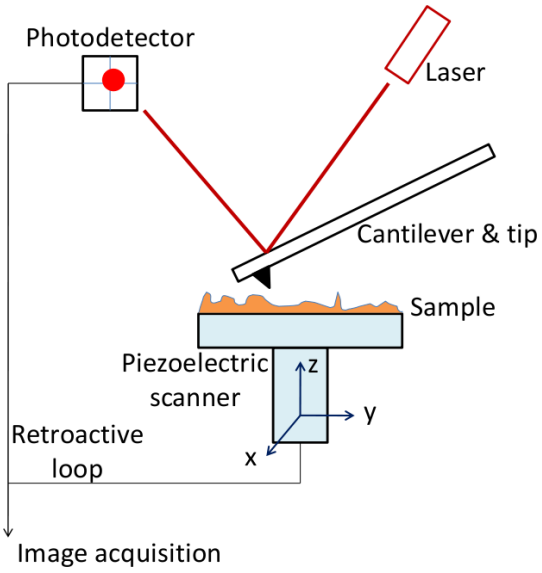

Figure 24: Schematic diagram of AFM and its components.

The principle is based on measurements of the interaction forces between atoms on the sample surface and a tip fixed on a cantilever. The sample surface is fixed on a piezoelectric support to move the tip in x, y, and z. Surface roughness leads to a variation of interaction forces leading to a variation of the distance between the tip and the surface

through the cantilever deflection, following Hooke's law. The reflection of a laser beam on the cantilever registers this bending. The signal is detected afterward by four photodiodes connected to a numerical acquisition system. The changes in the cantilever deflection or oscillation amplitude in the z direction are determined by differences in output voltages of the photodetector. The measurements lead to an accurate topography map.

There are 3 different modes:

- Tapping mode: The mode consists of oscillating the cantilever around its resonance frequency and lightly tapping on the sample surface during the scanning.
- Contact mode: The mode uses the repulsive forces based on Pauli exclusion principle. As the tip is raster-scanned across the surface, the cantilever deflects because of the surface roughness. The contact mode maintains a constant deflection to keep the force between the tip and the surface constant.
- Non-contact mode: Non-contact mode AFM does not suffer from tip or sample degradation when using contact-mode AFM. However, this mode uses the attractive forces which are quite low and require very low-noise environment.

For this work, a Veeco Dimension 3100 is used to investigate the surface morphology of nitride layers. All measurements were performed using the tapping mode. In addition to the sample surface topography, AFM allows roughness calculation through the root mean square (RMS) which is given by: $\sqrt{\frac{1}{N}\sum(z_i - \overline{z})^2}$. This parameter indicates the standard deviation of the sample height within the total surface.

2.4 Optical properties investigation

Spectroscopic ellipsometry: Spectroscopic ellipsometry (SE) is a non-destructive optical technique used for analysis and metrology. The technique allows the accurate

characterization of thin film layers through the calculation of the refractive index, extinction coefficients, alloy composition, anisotropy, roughness, and uniformity.

To investigate the optical properties of boron-based material, several samples have been analyzed with UVISEL phase-modulated ellipsometer (from HORIBA Scientific). The UVISEL ellipsometer instrument is shown in Figure 25 [8]. The basic components are: a Xenon lamp as a light source covering a large spectral range, a polarizer to establish a linear polarization, a photoelastic modulator to induce a modulated phase shift of the reflected beam, an analyzing polarizer to resolve its polarization state, a grating monochromator, and a detector [8].

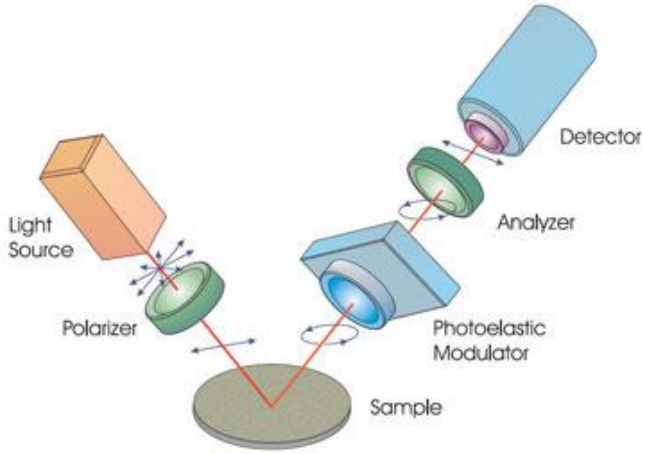

Figure 25: Optical setup of UVISEL ellipsometer [8].

Spectroscopic ellipsometry operates by measuring the change in the light polarization state before and after reflection upon a surface. The method measures two ellipsometric angles Ψ and Δ. They are related to the ratio of the Fresnel amplitudes reflection coefficients of the sample, as shown in Equation 27.

$$\frac{r_p}{r_s} = tan(\psi)\exp(i\Delta), \tag{27}$$

where (r_p, r_s) are the Fresnel reflection coefficients for parallel and perpendicular polarization of light, respectively. The Ψ and Δ refer to amplitude and phase changes of the ellipsometric ratio, respectively. Ψ and Δ depend on different parameters, such as the

layer thicknesses, the optical properties of each layer, and the incidence angle (usually taken between 65 and 75°). The used ellipsometer evaluates (I_s, I_c), which are linked to (Ψ, Δ), as shown in Equations 28 and 29.

$$I_c = sin(2\psi)cos(\Delta). \tag{28}$$

$$I_s = sin(2\psi)sin(\Delta). \tag{29}$$

The data measurement was performed over the range [250 - 800nm] under a 70° incidence and at room temperature.

This measurement technique is information-rich. However, it is indirect, which means that the measured quantities need to be compared or fitted to data generated from a model representing the sample. This modelisation was performed using DeltaPsi2 HORIBA Jobin Yvon software.

Photoluminescence: Photoluminescence spectroscopy is an extremely powerful optical analysis technique to measure the optical bandgap of semiconductor layers, their purity, and their crystalline quality.

Photoluminescence refers to the process of photon excitation followed by photon emission. In fact, a laser beam with an energy greater than bandgap energy is focused on the layer. The photons will be absorbed and thereby raise an electron from the valence band up to the conduction band, creating a hole in the valence band. In this process of photoexcitation, the electron loses its energy excess up to the lowest energy in the conduction band. The excess energy dissipation is presented in Figure 26 as the nonradiative relaxation. Then, the electron falls back down to the valence band through a radiative recombination involving a photon emission near the bandgap energy. The radiative process also involves defect levels with respect to nonradiative transition. The photoluminescence intensity can be used to identify the density defects. Reference [105] gives deeper details in photoluminescence measurements.

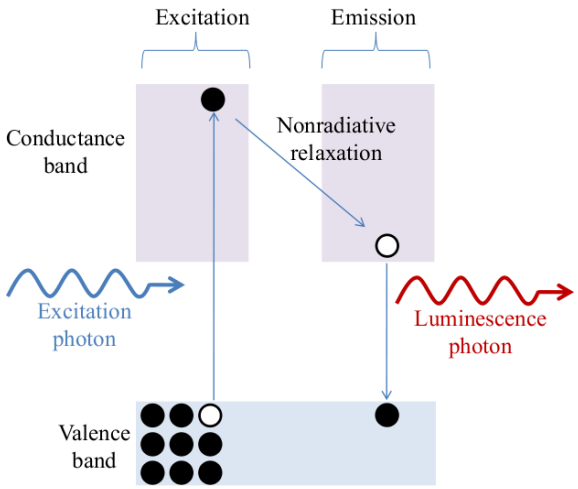

Figure 26: Schematic representation of photoluminescence principle.

All the PL measurements were performed in a continuous system. A CW Argon-Ion laser generates up to 2W light between 458 and 528nm. BBO crystals were used to produce deep-UV CW light. The light is focused onto the sample. The luminescence is analyzed using a spectrometer from Horiba Jobin Yvon equipped with a Synapse CCD detector and a photomultiplier tube. Additionally, a LN2-cooled cryostat from Janis Research can be used to perform low temperature measurements down to 66°K.

Fourier transform infrared spectroscopy: In comparison to dispersive techniques, for which each wavelength is detected at a time, fourier transform infrared spectroscopy is a fast and sensitive method to measure absorption in materials. FTIR can be noticeably very useful in Bragg mirrors reflectivity calculation or thin films transmission over a wide spectral range.

All the FTIR measurements presented in this project were performed by a Bruker Vertex 80V. The technique is based on the actively aligned UltraScan interferometer, which provides peak spectral resolution. The Vertex 80V is an evacuated optics bench that can eliminate atmospheric moisture absorptions for ultimate sensitivity and stability. That enables high resolution and UV spectral range measurements. The spectrometer

operates with three sources and three detectors enabling wide spectral range experiments (200nm - 10 μm) [106].

The basic principle of a FTIR spectrometer is explained as following: a light generated from a spectrally wide source passes through an interferometer. The specific frequency is absorbed when the interferogram signal is transmitted through a sample after few reflections and transmissions into the beamsplitter and the moving/fixed mirrors. As the detector interferogram cannot be directly interpreted, Fourier transform is applied. The raw data is represented by the absorbance (or transmittance) versus wavenumber.

Spectrophotometry: The DBR reflectivity analysis was performed on a dispersive dual beam UV/Visible Lambda 950 by Perkin-Elmer, which is more efficient than FTIR in the deep-UV region. The measurements of the film transmission and reflection were performed in the ultraviolet, visible, and near-infrared spectral range (200 - 900nm). The spectrophotometer is equipped with two different radiation pre-aligned sources: a deuterium UV lamp and a tungsten filament lamp for the visible and infrared spectral range, respectively. Depending on the spectral range to analyze, two detectors are used.

A photomultiplier R6872 is used for high energy in the whole UV/Vis wavelength range, and a peltier cooled PbS detector is applied for near Infrared (NIR). The spectral resolution are 0.2nm and 0.05nm in the NIR the UV/visible range, respectively. However, for all the performed measurements, one nm was used, which was widely enough.

This spectrophotometer can operate in transmission and reflection modes. Furthermore, the system can also be equipped with a universal reflectance accessory (URA) for variable angle specular reflection for thin layers films. A 150 mm integrating sphere can also be used for diffusive samples (in both reflection and transmission).

This system was mainly used for boron-based materials such as BGaN and BAlN with significant diffuse reflectance components. Therefore, using the integrating spheres was paramount. Samples are placed at the back of the sphere and the light is reflected

back off the sample and collected by the sphere. Measurements typically provide the total reflectance (Figure 27a) and the diffuse reflectance (specular excluded) portion (Figure 27b). Both total and diffuse reflectance can be measured independently. The latter measurement is achieved by allowing the specular component to exit the sphere through the open specular port [107]. The specular reflectance is measured by deducing the diffuse reflectance from the total data.

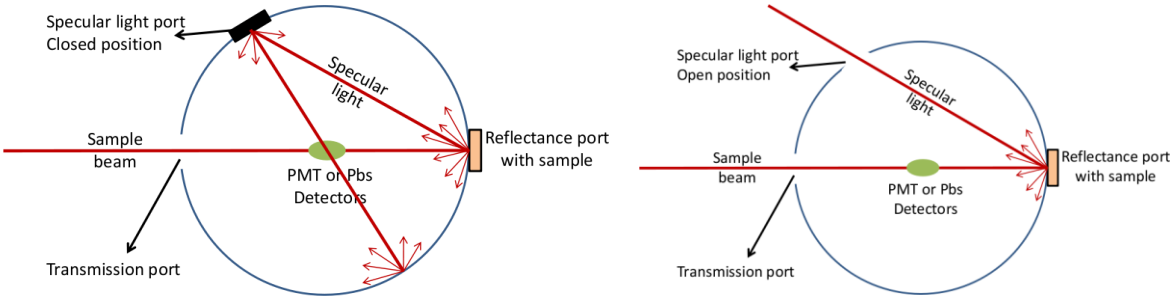

(a) (b)

Figure 27: Measurement of (a) the total reflectance and (b) the diffuse reflectance (specular excluded) using an integrating sphere.

Raman spectroscopy: Raman spectroscopy is a non-destructive technique based on the light inelastic scattering phenomenon generated from the excitation of vibrations in molecular and crystalline materials. Raman coupling with optical microscopy allows probing reduced volumes in the investigated sample. As is is not a resonant process, the probability that the transitions between the excitation and detected energies to occur is very low [108].

Despite the fact that the technique was first demonstrated in 1928 by C.V. Raman, it was only intensively used in the seventies thanks to the development of high-intensity lasers with excellent monochromaticity. As a matter of fact, a single line of a continuous laser source forms the excitation part.

Raman spectroscopy technique is very sensitive to molecular and crystal structure. That enables an accurate measurement of the crystallinity of the nitride layers,

identifying noticeably if the grown films are polycrystalline. This feature will be used for BAlN films (Chapter 5).

The basic principle of Raman spectroscopy is as following: regarding the investigated sample, an intense laser beam in the UV, visible, or infrared range impinges on the sample. This sample illumination generates an electric field distorting the sample electron clouds, leading to some energy storage. The energy will be then reradiated at the same frequency than that of the incident excitation light, referred as Rayleigh scattering. Another part of the stored energy is then transferred to the sample and leads to an excitation of the vibrational modes. The vibrational energies are deduced from the energy of the incident beam, and weak side bands appear in the spectrum forming the Raman lines [108].

2.5 Electron emission and mass spectroscopies

Secondary ion mass spectrometry: SIMS is a widely used analytical characterization technique for analysis of semiconductor alloys. The technique is a very sensitive surface analysis able to detect low concentrations of atoms such as impurities or dopants at the part-per billion (ppb) levels. It can also provide a wide range of elemental depth profiles by drawing different elements concentrations as a function of depth. Interface quality, and layer thickness can also be observed empirically.

SIMS operates by bombarding the sample surface with a primary beam of high energetic ions (1-30 KeV) such as O_2^+, Cs^+, Ar^+, or Ga^+ to produce physical damage and sputter charged and un-charged species. In opposition to high sputtering mode used for depth profiles, static SIMS is performed when the sputtering rate is extremely low. That enables the entire analysis to be performed while consuming less than a tenth of an atomic layer. Sputter rates mainly depend on sample material and primary beam intensity and fall in a range from 0.5 to five nm/s [109].

The ejected secondary ions are extracted, energy filtered, and fed into a mass spectroscopy system to count the ions at each step (in ions per second). The number of ejected ions per incident primary ion is called the secondary ion yield. At the end of the sputtering, the sputtered depth crater is measured to draw the depth profile.

SIMS can also be used for quantitative analysis by using relative sensitivity factors defined according to the following equation [109]:

$$\frac{I_R}{C_R} = RSF_E \frac{I_E}{C_E}, \tag{30}$$

where I_E and I_R are the secondary ion intensity for the element of interest and a reference element. C_E and C_R are the concentration of the element of interest and the reference element. RSF_E is the relative sensitivity factor for element E which needs very accurate calibration.

SIMS is extremely powerful technique and widely used for thin films materials. However, it presents few limitations:

- The technique is locally destructive.
- The exact incorporation in the ternary or quaternary alloys is very difficult to obtain.
- The technique suffers from mass interference problems.

X-Ray photoelectron spectroscopy: The major purpose of the non-destructive Photoelectron spectroscopy is to study the composition and electronic state of a sample. The technique is based on photo-ionization and analysis of the kinetic energy distribution of the emitted photoelectrons.

The basic components of XPS tool are an X-ray source of fixed-energy, an electron energy analyzer, electronic controls, and a high vacuum system to avoid surface reactions and contaminations. XPS technique uses monochromatic sources of radiation and is based upon a single photon in / electron out process. The X-rays penetrate the sample reaching a depth of a micrometer, and the emitted photon is absorbed by an atom in the sample. That results on the ionization and the emission of a core-level (inner shell)

electron. The number of emitted photoelectrons as a function of their kinetic and binding energy refers to the kinetic energy distribution. It can be measured using an appropriate electron energy analyzer and enable the determination of the photoelectron spectrum.

In addition to the energy analysis of the emitted photoelectrons, the analysis of auger electrons can also be performed in XPS. In fact, an outer electron fills the core hole when the core electron is ejected by the X-ray radiation. Consequently, an Auger electron is emitted to balance the energy of this transition [110, 111].

All the XPS measurements performed in this study were carried out in LGEP in Paris.

CHAPTER 3

THEORETICAL STUDY OF THE DBR STRUCTURES IN THE UV RANGE

3.1 Distributed Bragg reflectors

Since the DBR reflectivity and bandwidth determine the VCSEL performances, the basic parameters and equations governing the DBRs characteristics are summarized in this section.

Originally known as "quarter-wave mirrors", this structure was renamed to "distributed Bragg reflector", referring to the Bragg's law that describes the diffraction of X-rays at atomic planes (Equation 25). The Bragg's law was introduced in Chapter 2 to describe the interference pattern of X-rays scattered by crystals. The diffraction can be applied with any beam: electrons, ions, protons, and neutrons. In the case of DBRs, photons are interacting with periodic interfaces in heterostructures. The sum of the reflected part of the incident electromagnetic waves on the different interfaces gives the reflectivity of the DBR structures [34]. A more detailed description of the calculation of the DBR reflectivity will be presented in next sections.

A DBR is a periodic multilayer structure with a unit cell formed by two quarter-wave layers, alternating layers of low (n_L) and high (n_H) refractive index material.

The reflectivity of a mirror is a function of the refractive index variation between both layers forming the stack and the number of periods (m). A simple formula can be used to calculate the DBR theoretical reflectivity, as shown in Equation 31.

$$R_{Th} = |r_{Th}|^2 = \left(\frac{1 - \left(\frac{n_H}{n_L}\right)^{2m}}{1 + \left(\frac{n_H}{n_L}\right)^{2m}}\right)^2. \quad (31)$$

This theoretical calculation assumes that the different layers forming the DBR stack are quarter wavelength (λ/4n thick). This feature guarantees constructive

interferences and leads to a maximum reflectivity value. The above equation for peak reflectivity is true at a normal incidence and at the central wavelength λ_{Bragg}. The experimental reflectivity is usually lower than the theoretical calculation as the layers absorption, the interfaces quality, and the surface roughness affect the real measure. A detailed calculation of the reflectivity simulation as a function of the wavelength and the number of periods will be given in Section 3.2.1.

As mentioned in the previous chapters, because of their short amplification lengths, VCSEL devices require reflectivity exceeding 99% to overcome the different losses and reach the threshold. The high reflectivity can be achieved either by increasing the number of periods or by selecting materials with high refractive index contrast Δn. Consequently, intensive efforts will be performed in next chapter to study the optical properties of boron-based materials. These materials can present an efficient solution for new-generation DBR structures in the UV range.

Given the difficulties in growing a uniform active region, a DBR structure with a wide bandwidth is fundamental for a better efficiency of the laser device structure. In fact, the electroluminescence peak of the active region has to be aligned with the DBR reflectivity within its stopband [41]. The bandwidth is complicated to express and use analytically, because it depends on many parameters. The parameters include the number of layers, the central wavelength, and mainly the refractive index of both materials. The spectral width of the stopband can be approximated by the Equation 32.

$$\Delta\lambda_{stopband} = \frac{4\lambda_{Bragg}}{\Pi} arcsin\left(\frac{n_H - n_L}{n_H + n_L}\right) = \frac{2\lambda_{Bragg}\Delta n}{\Pi n_{eff}}, \tag{32}$$

where n_{eff} is given by:

$$n_{eff} = 2\left(\frac{n_{high}n_{low}}{n_{high} + n_{low}}\right). \tag{33}$$

Another important parameter that has to be taken into consideration is the penetration depth of the optical mode. The penetration depth defines the partial

penetration of the optical wave in the reflector. This parameter significantly increases the cavity length and cavity order and consequently the mode spacing [41]. Equation 34 gives the penetration depth into the reflector:

$$L_{eff} = r\frac{\lambda}{4\Delta n}. \tag{34}$$

To reach a high reflectivity in distributed Bragg reflectors, it is of prime importance that there is no residual light absorption of the incident wave within the structure. Therefore, a good choice of the materials selection is fundamental in the DBR design.

In addition to VCSEL devices, the realization of highly reflective nitride Bragg reflectors is a first step toward the development of other optoelectronic devices. They include Fabry-Perot modulators, high finesse microcavities, and resonant-cavity light-emitting diodes (RCLEDs). In fact, DBRs can be used to improve the light extraction efficiency of light-emitting diodes and obtain narrow and directional emission. The mirrors can be multilayered-dielectric or epitaxially-grown DBRs.

3.1.1 Epitaxial DBRs

A state-of-the-art of the nitride DBR structures was summarized in Section 1.4. The different nitride systems that can be used to develop mirrors in the UV range were reported. In fact, the most conventional system is undoubtedly AlGaN/AlGaN system. However, the demonstration of a highly reflective structure with a broad bandwidth in the UV range has been proved to be challenging.

The basic dynamic in AlGaN-based structures is that material quality is affected by large lattice mismatches. Nevertheless, reduced lattice mismatches result in a large number of periods and also a limited bandwidth. The introduction of the boron-based DBR structures can overcome some of the issues related to the limited refractive index contrast and reduced bandwidth.

This research will be largely detailed in the following sections. In fact, the growth and study of optical properties of the boron-based materials and their integration in DBR stacks will be described in Chapter 4 and Chapter 5, respectively.

3.1.2 Dielectric DBRs

In contrast to the bottom DBR, the top mirror is conventionally a dielectric one. These materials take advantage of their relative ease of deposition and their high refractive index contrast. A plasma-enhanced chemical vapor deposition reactor (PECVD) is generally used for the deposition of dielectric materials. The large refractive index contrast leads to thin structures since only few periods are needed to reach 99% reflectivity. In the optical pumping configuration, a laser pumping through the dielectric mirror is fundamental. To limit the reflectivity of the pump wavelength, a specific design of this dielectric mirror may be necessary.

As mentioned in the first chapter, the typical round-trip gain in a VCSEL cavity is of the order of few percents. To achieve the lasing threshold, the total cavity losses, including the mirror losses, have to be maintained below this value. Assuming a 99.9% bottom epitaxial mirror, and negligible intra-cavity loss, at least ~ 98% reflecting dielectric DBRs are required for the top UV-mirrors. The high reflectivity implies that the extinction coefficient k of the amorphous dielectric materials must be very low at the emission wavelength.

From the first dielectric DBR structure which was developed in the early 1950's in the visible range using ZnS/MgF system, intensive efforts were performed to reach highly reflective DBRs. The conventional SiO_2/SiON system has been already proposed and proved to be efficient to fabricate planar microcavities in the 340nm - 390nm wavelength range [112, 113, 114]. Other dielectric systems can also be used for UV DBRs such as SiO_2/HfO_2, SiO_2/Si_3N_4, and SiO_2/ZrO_2 systems. The SiO_2/HfO_2 and SiO_2/Si_3N_4 systems are often used to realize low-loss highly reflective mirrors, mostly at

wavelengths above 300nm [34, 115, 116]. Only few reports of DBR structures were reported in the 250nm-300nm range. A reflectivity close to 99% has been reported at 250nm wavelength using SiO_2/HfO_2 material system [117]. Therefore, this system can be applied to fabricate VCSEL devices at deep-UV range.

While the semiconductor-based mirrors are expected to present very low optical losses, the extinction coefficient of HfO_2 may reach 10^{-3} in the 200nm - 300nm UV-range. This feature can be explained by the deposition of a sub-stoechiometric (O/Hf < 2/1) material. In addition to SiO_2/HFO_2 system, SiO_2/Al_2O_3 and MgF_2/Al_2O_3 systems can also offer highly reflective mirrors. These systems are interesting alternatives, as they will be less prone to optical absorption in comprison to the previous system. This feature can be explained by the wide bandgap of the considered materials [118]. However, in comparison to SiO_2/HFO_2, the refractive index contrast of these systems is smaller, which leads to a narrower mirror stopband. Therefore, a larger number of pairs to achieve 98% reflectivity is required.

Table 5 summarizes the properties and the potential performances of the different materials that can be employed in the final structure for DBR structures at 280nm.

Table 5: Performances of dielectric DBR mirrors.

Low-index material (refractive index, n@280nm)	High-index material (refractive index, n@280nm)	Number of pairs for R>99% at 280nm
SiO_2 (n=1.5)	$Hf0_2$ (n=2.1)	8 pairs
SiO_2 (n=1.5)	Al_2O_3 (n=1.8)	15 pairs

In conclusion, according to the preliminary simulations, HfO_2/SiO_2 is one good solution to develop the top dielectric Bragg mirror. Several other candidates can be

employed in the final structure as well. However, in this dissertation, the dielectric mirrors won't be developed further.

3.2 Software design and realization

To estimate the level of performance of the various components of a VCSEL structure, computer simulations are used in the design of the final device. For this purpose, various commercial software such as Pics3d or Silvaco were tested. However, their lack of flexibility makes them difficult to use. In fact, with these commercial software, it is very difficult to add the experimental parameters of boron-based materials such as refractive index and energy-bowing parameter. Therefore, the development of a local software was fundamental. Toward this end, the Matlab environment was used. Furthermore, in contrast to commercial software, making our own numerical models and software offers us a deeper understanding of the physics involved.

3.2.1 III-N-match software

The first developed software is named III-N-match. It gives (a) the lattice mismatch of all ternaries and quaternaries III-N materials with respect to all available substrates, (b) the relaxation critical thickness, (c) the refractive index, (d) the X-ray diffraction expected diffraction peaks, and (e) the bandgap of the different alloys using up to date experimental energy-bowing parameters [33]. Furthermore, the software performs the reciprocal calculations. This means that starting from the measured bandgap of any ternary or quaternary III-N alloy, XRD peak, or lattice parameter, III-N-match is able to calculate the corresponding materials compositions. A schematic of the III-N-match software is shown in Figure 28. The equations used to calculate the various parameters in this software are extracted from [31, 35, 119].

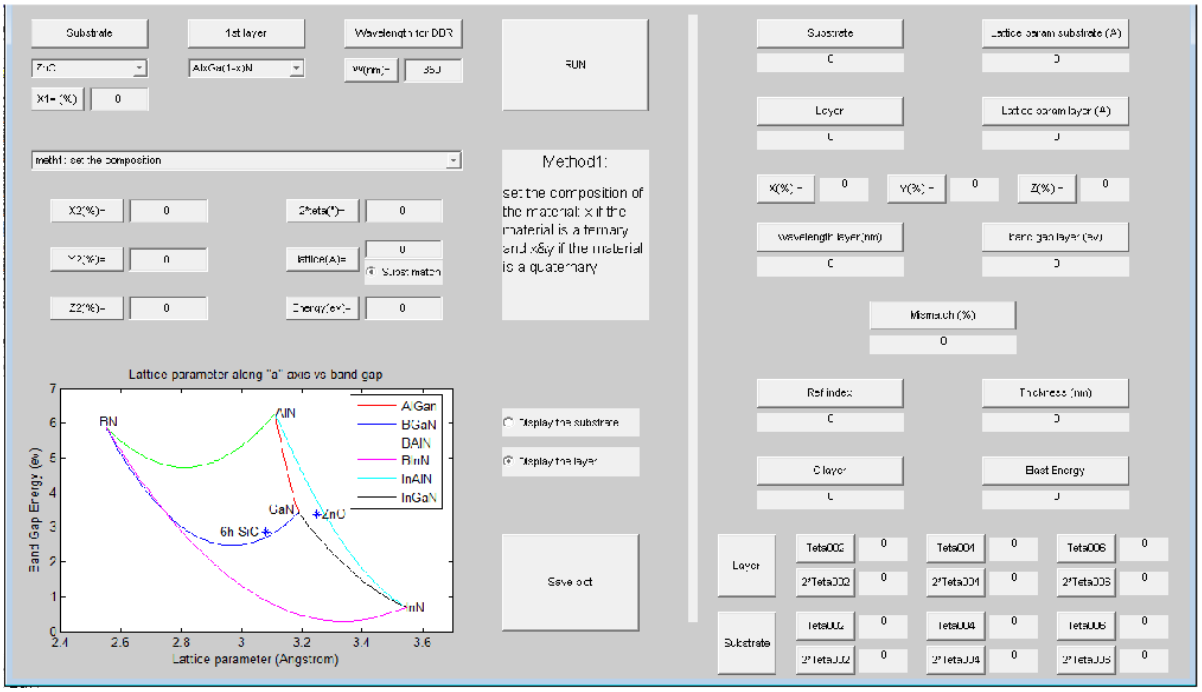

Figure 28: Designed software III-N-match.

For instance, different methods were reported to calculate quaternary alloy bandgap parameters from those of the underlying binary and ternary materials. The interpolation approach was used to guarantee good results. The approach was introduced by Glission *et al.* [120]. This approximation can be applicable to all III-nitrides quaternaries. Equation 35 illustrates the bandgap calculation for $B_xAl_yGa_{1-x}N$ quaternary [31].

$$Eg_{BAlGaN}(x,y) = \frac{xyEg_{BAlN}(u) + y(1-x-y)Eg_{AlGaN}(v) + (1-x-y)xEg_{BGaN}(w)}{xy + y(1-x-y) + (1-x-y)x}, \quad (35)$$

where $u = \frac{1-x-y}{2}$, $v = \frac{2-x-2y}{2}$, and $w = \frac{2-2x-y}{2}$. The ternaries bandgaps have to take into consideration the different nitride bowing parameters, which were summarized in Table 3.

3.2.2 Reflector software

The simulation of the DBR reflectivity and bandwidth is of great importance to characterize the behavior of the overall VCSEL structure. The reflectivity was simulated using the standard transmission matrix theory through a second software called Reflector. A more detailed description of the calculations is given in [121, 122]. The method is based on a matrix formulation of the boundary conditions, derived from Maxwell's equations. Starting from a multilayer structure with different refractive indexes, the sum of the intensities of electromagnetic field at the i-th boundary is equal to the sum of the field intensities at the next boundary multiplied by the phase shift. These two expressions give the refraction (Equation 36) and the phase (Equation 37) matrices.

$$W_{i-1,i} = \frac{1}{2}\begin{pmatrix} 1+\frac{Y_i}{Y_{i-1}} & 1-\frac{Y_i}{Y_{i-1}} \\ 1-\frac{Y_i}{Y_{i-1}} & 1+\frac{Y_i}{Y_{i-1}} \end{pmatrix}, \tag{36}$$

$$U_i = \begin{pmatrix} exp(j\varphi_i) & 0 \\ 0 & exp(-j\varphi_i) \end{pmatrix}, \tag{37}$$

where the optical admittance at the i-th layer is Y_i, and φ_i is the phase shift caused by the transmission of the field through the i-th layer. In fact, each layer is described by a phase matrix and each interface by a refraction matrix. The optical transfer function of the DBR is given by the product of the different phase and refraction matrices (Equation 38).

$$\begin{pmatrix} E_{R1} \\ E_{L1} \end{pmatrix} = W_{0,1}U_1W_{1,2}U_2...W_{k-1,k}U_kW_{k,k+1}\begin{pmatrix} E_{Rk+1} \\ E_{Lk+1} \end{pmatrix} = \begin{pmatrix} s_{11} & s_{12} \\ s_{21} & s_{22} \end{pmatrix}\begin{pmatrix} E_{Rk+1} \\ 0 \end{pmatrix}, \tag{38}$$

where E_R and E_L present the right- and left-going waves (Figure 29) and S (s_{ij}) is the optical transfer matrix.

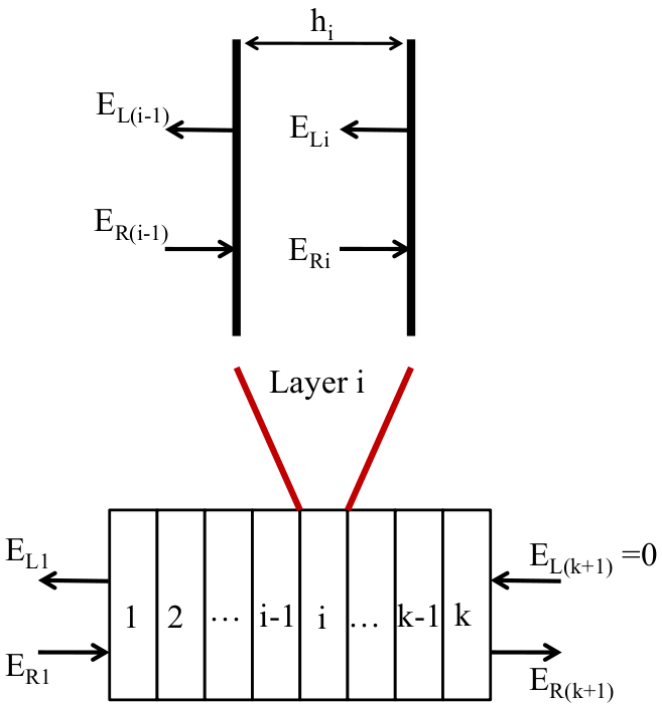

Figure 29: Electromagnetic wave incidenting on the DBR structure.

Finally, the reflectivity is given in Equation 39.

$$R = |\frac{E_{L1}}{E_{R1}}|^2 = |\frac{s_{21}}{s_{11}}|^2. \tag{39}$$

To achieve high reflectivity in conventional AlGaN-based DBRs, it is fundamental to have a large refractive index contrast between the layers forming the DBR. However, as mentioned in the previous chapters, the DBR design must carefully balance competing trade-offs when using conventional AlGaN materials between refractive index, materials absorption, and lattice mismatch. But, one major factor that has to be taken into account is the in-plane lattice, as it induces dislocations and cracks in the structure. Consequently, designing strain-free mirrors is of paramount importance for VCSEL devices. The different zero-stress approaches were investigated. The calculations were based on J. Zhang *et al.* article [123] and J.M. Bethoux PHD thesis dissertation [124]. They investigated the concept of strain balance for a two-layer system by studying the in-plane stress from an elastic theory.

For a specific layer, the elastic energy by unit surface is given in the following equation:

$$\frac{E_{elas}}{S} = M.h.\varepsilon, \tag{40}$$

where h is the thickness, ε is the deformation of the layer (Equation 41), and M is the biaxial module of the material as a function of the different stiffness coefficients, as shown in Equation 42. The stiffness coefficients are presented in Table 9 (Appendix A).

$$\varepsilon = \frac{a_0 - a_1}{a_1}. \tag{41}$$

$$M = C_{11} + C_{12} - \frac{2 * C_{13}}{C_{33}}. \tag{42}$$

According to the elastic energy theory, the elastic energy of the whole structure is the sum of the energy for each layer. The minimum strain is obtained when the energy is minimized, which requires that the derivative of E_{elast} is equal to 0.

The minimum strain is achieved when the structural quality of the DBR is maintained by compensating the compressive and tensile stress. Equation 43 describes the relationship between the lattice parameter of the relaxed substrate, the first layer (a1), and second layer (a2), to get a strain-free structure. Using this approach, the software allows an accurate calculation of the different lattice parameters and as a further step the required alloys content to obtain strain-free structure.

$$a_0 = a_1 a_2 \frac{(m+1)M_1 h_1 a_2 + m M_2 h_2 a_1}{(m+1)M_1 h_1 a_2^2 + m M_2 h_2 a_1^2}. \tag{43}$$

Some DBR simulations were also performed to investigate asymmetric DBR structures. For instance, for the development of AlN/GaN DBR structure on AlN template, structures using 3λ/4 AlN and λ/4 GaN layers were proposed by Ng *et al.* [65]. However, the peak reflectivity and the stopband width are reduced in these asymmetric structures.

Consequently, a large number of periods is needed to achieve highly reflective DBRs, which makes this solution not very efficient. This approach is further described in Section 3.3.1.

Figure 30 presents the Reflector software. Starting from the calculated refractive index for BGaN, BAlN, and AlGaN, the software is able to predict the different thicknesses, the expected reflectivity, and the DBR bandwidth. Furthermore, the software allows the development of strain-free DBR structures by selecting the optimum alloys compositions of the two layers forming the DBR stack. This feature will be further developed in Chapter 5 when BAlN/AlGaN DBRs will be introduced.

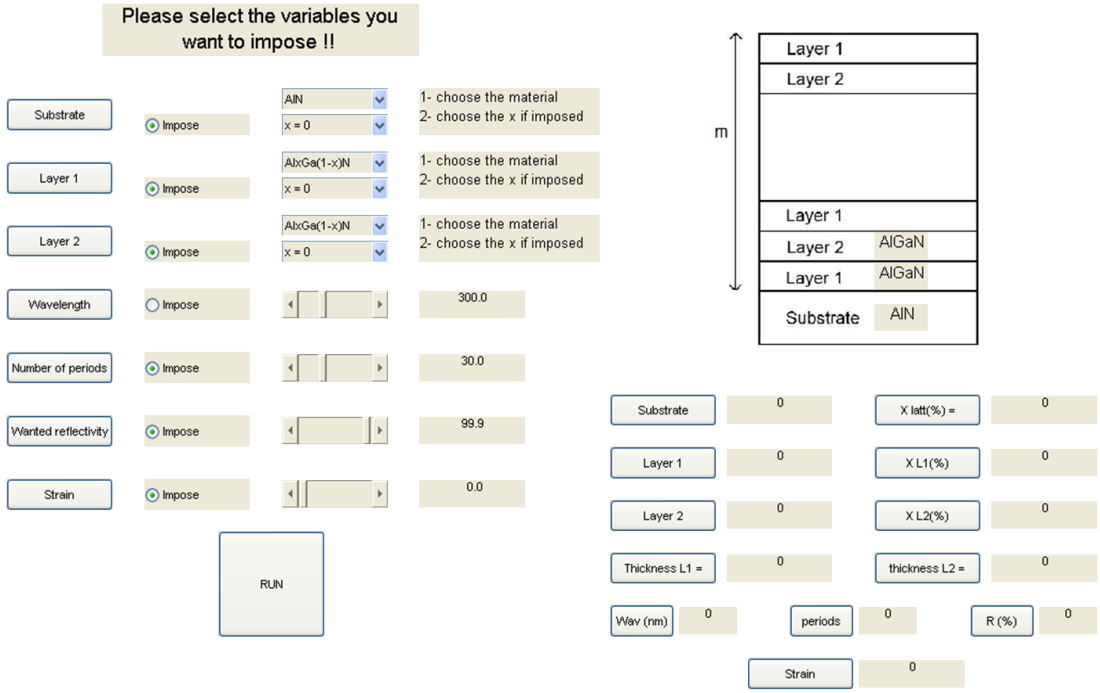

Figure 30: Designed software for strain-free mirrors.

3.3 Simulation of the epitaxial distributed Bragg reflectors

As explained earlier, because of the limited relaxation thickness, the number of periods is limited in the AlGaN-based structures. The highly reflective structures suffer usually from cracks and dislocations. Therefore, several solutions were proposed. The first

solution is to use multiple AlN interlayers to compensate for the tensile strain in GaN/AlGaN Bragg mirrors. This approach has shown a good efficiency and 99% reflectivity was achieved at 410nm [67]. Another interesting solution was the insertion of AlN/GaN superlattice stacks in the reflector structure. Several positions for these SL insertion stacks have been reported with good results: either prior to the growth [125] or periodically in the whole Bragg mirror structure [126]. The latter solution allowed the development of the first GaN-based electrically-pumped VCSEL structure emitting near 462nm and operating in continuous wave at 77K [61]. However, in these structures, fully-strained compounds are difficult to achieve. This relaxation would affect the surface quality of the mirror especially if a regrowth of an active region is planned.

One additional important approach is to use asymmetrical design. In fact, previous works have shown that asymmetrical design could be an efficient solution for the realization of Bragg mirrors using highly lattice-mismatched materials [9, 127]. Such asymmetrical design should avoid the crystal relaxation and therefore results in the development of a high-surface quality adapted for epitaxial regrowth. In this section, asymmetrical designs were investigated to realize AlGaN/GaN mirrors without relaxation. Based on the critical thickness, several AlGaN/GaN mirror structures were simulated with various Al content and degrees of asymmetry. Such calculations showed the possible design of highly reflective fully-strained $Al_xGa_{1-x}N$/GaN mirrors in the near-UV wavelength range. Finally, because of the combination between refractive index and critical thickness evolution, the best suited Al molar fraction in AlGaN alloy changes with the operating wavelength.

3.3.1 Asymmetric AlGaN-based DBR designs

When materials used in a Bragg mirror are lattice-matched, there are no particular crystalline limitations for its development, and the total thickness would not present any issue to reach the aimed reflectivity. However, for strained materials system, the critical

thickness prevents the achievement of crack-free high-reflectivity structures. The critical thickness will be described in Section 4.3.2. To overcome this issue, asymmetrical DBR designs were proposed few years ago [9, 127] wherein the total optical length of the pair of layers is kept equal to λ/2. Within a pair, an asymmetry factor (t) is introduced to minimize the strain by adapting the thicknesses to keep light reflections in phase at each pair interface. A schematic description of such asymmetrical design is given in Figure 31.

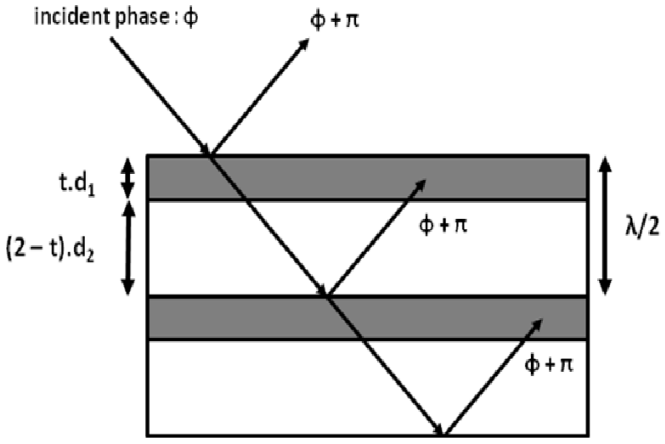

Figure 31: Schematic description of an asymmetrical DBR (from [9]). t (0<t<1) is the asymmetry factor. d1 and d2 are the quarter-wavelength optical thicknesses of the strained material and the lattice-matched one, respectively. The total optical thickness is λ/2.

If d1 and d2 are the quarter-wavelength thicknesses, the optical thicknesses e1 and e2 of the materials in the asymmetrical structure will be the following:

$$e1 = t * d1, \tag{44}$$

$$e2 = (2 - t) * d2. \tag{45}$$

Asymmetrical DBRs exhibit a lower maximum reflectivity and a smaller bandwidth than conventional symmetrical quarter-wavelength mirrors with the same number of periods. These properties can be essentially explained by the fact that the light reflections, occurring at the interfaces between strained and lattice-matched layers, are not in phase with others, as illustrated in Figure 31.

The AlGaN refractive index is a function of the wavelength and the Al molar fraction. The dispersion of such index values depending on the aluminum content is extracted from [5].

The higher is the Al molar fraction, the higher is the index contrast with GaN. Moreover, AlGaN alloys are tensively strained on GaN, and their critical thickness decreases rapidly when the Al molar fraction increases. Therefore, it is fundamental to find the best compromise between refractive index contrast and strain to maximize the optical performances of the asymmetrical AlGaN/GaN DBRs. Bragg mirror reflectivities were calculated by taking into account the AlGaN refractive index dispersion and absorption.

Figure 32 presents the maximum reflectivity that can be theoretically obtained as a function of the asymmetry factor for different AlGaN/GaN DBRs with different Al content, i.e. 15%, 20%, 30%, and 40%. The structures were centered at λ_B = 450nm. The choice of 450nm was imposed to prevent any absorption coming from the GaN layers, suggesting more accurate simulations. Although the $Al_{0.4}Ga_{0.6}N$/GaN system exhibits the largest index contrast, it is also the one that requires the lowest asymmetry factors to achieve equivalent reflectivity compared to the other materials stacks. Consequently, it appears that $Al_{0.4}Ga_{0.6}N$/GaN is the least suitable materials couple among the different systems shown in Figure 32. Similarly, $Al_{0.15}Ga_{0.85}N$/GaN and $Al_{0.3}Ga_{0.7}N$/GaN systems appear to be less suitable than $Al_{0.2}Ga_{0.8}N$/GaN for this application. Indeed, for R = 80%, t is equal to 0.13 and 0.14 for $Al_{0.3}Ga_{0.7}N$/GaN and $Al_{0.15}Ga_{0.85}N$/GaN, respectively, while it is equal to 0.15 for $Al_{0.2}Ga_{0.8}N$/GaN. Similar results are found regardless the desired maximum reflectivity at 450nm. Indeed, for R = 60%, the t values increase, i.e. 0.18, 0.19, and 0.20, for $Al_{0.15}Ga_{0.85}N$/GaN, $Al_{0.3}Ga_{0.7}N$/GaN, and $Al_{0.2}Ga_{0.8}N$/GaN, respectively. Therefore, we conclude that the combination between critical thickness and refractive index contrast leads to different optimum Al molar fractions as a function of the central wavelengths.

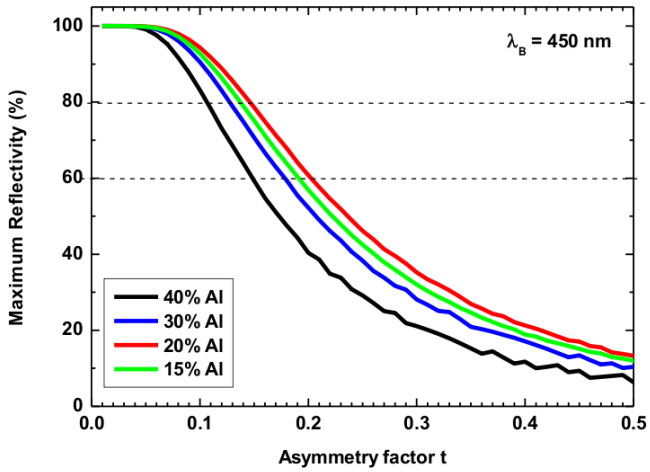

Figure 32: Theoretical maximum reflectivity of asymmetrical strained AlGaN/GaN DBRs centered at 450nm as a function of asymmetry factor t for four different Al compositions: 15%, 20% , 30%, and 40%.

The evolution of the asymmetrical factor required to achieve a given reflectivity at different wavelengths as a function of the Al molar fraction in AlGaN was then studied. Results obtained for R = 80% and R = 60% at two different centered wavelengths λ_B = 450nm and λ_B = 400nm are presented in Figure 33. This figure clearly illustrates that there is a best suited Al molar fraction in AlGaN depending on the DBR center wavelength. This fraction decreases with the wavelength. For instance, for λ_B = 450nm, the largest asymmetrical factors are obtained for an Al fraction of 20%, whereas this value is lowered to 12% at λ_B = 400nm. As expected, the asymmetrical factors for $Al_{0.12}Ga_{0.88}N$/GaN materials couple are larger than those for $Al_{0.2}Ga_{0.8}N$/GaN. This feature indicates that the asymmetrical design of AlGaN/GaN DBRs is more appropriate for short wavelengths.

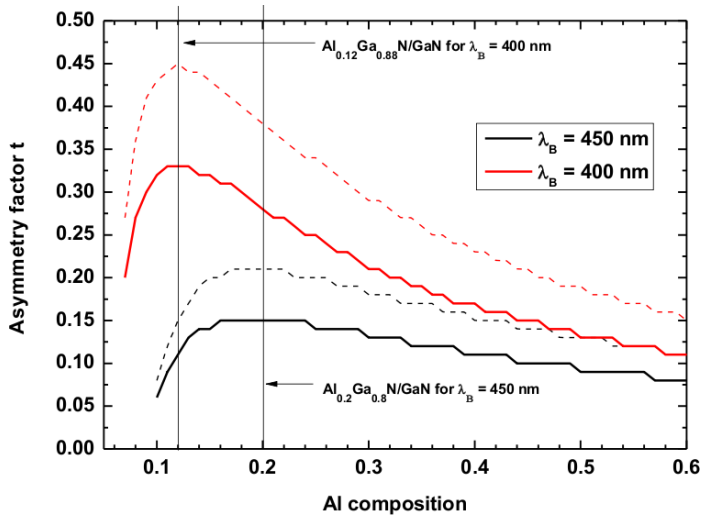

Figure 33: Asymmetry factor necessary to achieve reflectivities of 60% (dashed lines) and 80% (solid lines) in asymmetrical fully-strained AlGaN/GaN DBRs centered at λ_B = 450nm and λ_B = 400nm as a function of Al molar fraction in AlGaN. The best suited Al molar fraction (corresponding to the larger asymmetriy factor) is different depending on the centering wavelength of the mirror but remains constant with the maximum reflectivity expected.

The last parameter studied in this work was the bandwidth. This value was investigated using the transfer matrix model and was defined earlier. Figure 34 presents the variations of the bandwidths of $Al_{0.12}Ga_{0.88}N/GaN$ and $Al_{0.2}Ga_{0.8}N/GaN$ fully-strained asymmetrical DBRs centered at 400nm and 450nm, respectively, as a function of the asymmetry factor. The central wavelength was chosen as the best suitable value for each materials system, as determined in Figure 33. As expected, the bandwidth is strongly influenced by the asymmetry factor and dramatically decreases with the asymmetry. However, because of the limited AlGaN critical thickness grown on GaN, the greater the asymmetry factor is, the lower the number of pairs is. This feature results in a low maximum reflectivity. The two best suitable asymmetrical factors for both previously defined material systems are also reported in Figure 34. However, the calculated bandwidths are still very low (< 5nm), which is the major handicap of these fully-strained asymmetrical AlGaN/GaN DBRs. Another important handicap is the significant number of periods required to reach highly reflective DBR structures, which makes this approach unrealistic. In conclusion, this solution can not be efficient in the development of high-

reflectivity DBRs in the UV range. Therefore, the investigation of new boron-based materials is fundamental. This innovative approach is presented in next section.

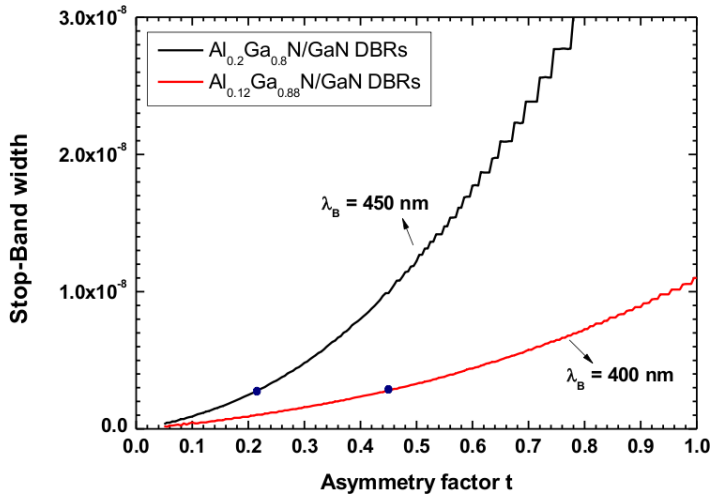

Figure 34: Stopband width as a function of asymmetry factor for GaN/$Al_{0.2}Ga_{0.8}N$ and $Al_{0.12}Ga_{0.88}N$/GaN DBRs. The centeral wavelengths are 400nm for $Al_{0.12}Ga_{0.88}N$/GaN and 450nm for $Al_{0.2}Ga_{0.8}N$/GaN as the best suitable determined in Figure 33. The full circles represent the bandwidth of R =60% DBRs.

3.3.2 Symmetric boron-based structures

In the previous section, the asymmetrical DBR design is presented to overcome the issue of the limited refractive index combined to the limited AlGaN critical thickness. However, this approach cannot be applied because of the significant number of periods required to achieve high-reflectivity structures and the limited bandwidth.

Therefore, in this section, different nitride systems are investigated for the development of DBR structures in the near-UV and UV region. First, the conventional AlGaN-based structures are described. Then, boron-based structures will be investigated using the Reflector software. All the simulations performed in this study use experimental refractive index values, which will be described in next chapter.

AlGaN-based DBRs: As mentioned earlier, the AlGaN-based structures suffer from high dislocation density and cracks because of the large lattice mismatch between GaN and AlN materials. In the near-UV region, the AlGaN/GaN is undoubtedly the most common system. However, the limited refractive index limits the peak reflectivity. Figure 35

presents the required aluminum content in the $Al_xGa_{1-x}N$ layer as a function of the number of periods to achieve 99.9% reflectivity at 400nm.

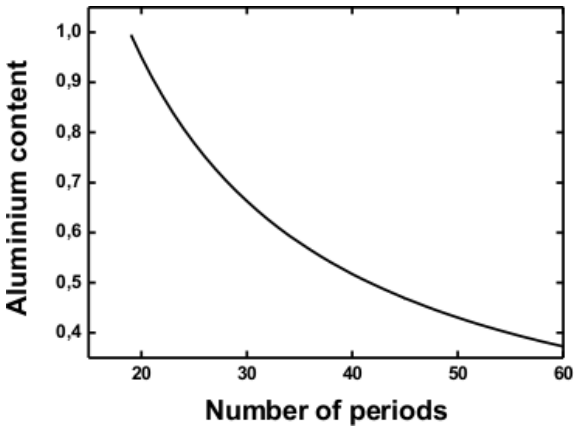

Figure 35: Required aluminum content in $Al_xGa_{1-x}N$/GaN DBRs versus number of periods to reach 99.9% reflectivity at 400nm.

The DBR simulations, shown in Figure 35, do not take into consideration the large lattice mismatch. This issue will be deeply described in next chapter by introducing the AlGaN critical thickness grown on GaN template. With the difficulty to develop thick AlN/GaN structures, it is fundamental to use low aluminum content. However, the number of periods to achieve 99.9% reflectivity will be very high. For instance, 42 periods are theoretically required to achieve 99.9% reflectivity using $Al_{0.5}Ga_{0.5}N$/GaN system.

To reach short wavelength, GaN materials are too absorbent and cannot be used anymore. Therefore, AlGaN/AlN systems are required. Figure 36 presents the required aluminum content in the $Al_xGa_{1-x}N$ layer as a function of the number of periods to achieve 99.9% reflectivity at 280nm. The theoretical calculation does not take into consideration the attenuation caused by the surface roughness or by the presence of cracks and dislocations.

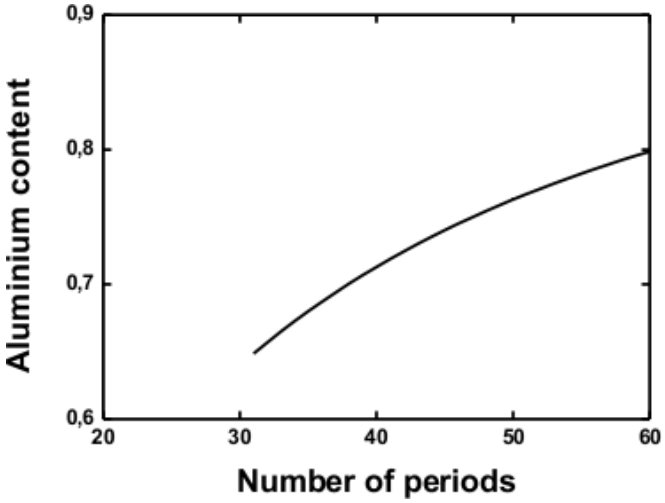

Figure 36: Required aluminum content in $Al_xGa_{1-x}N$/AlN DBRs versus number of periods to reach 99.9% reflectivity at 280nm.

It is observed that it is impossible to achieve 99.9% reflectivity with less than 30 periods. For instance, using $Al_{0.7}Ga_{0.3}N$/AlN system, 40 periods are required to achieve 99.9% at 280nm. Figure 37 presents the theoretical reflectivity as a function of wavelength for a 40-pair $Al_{0.7}Ga_{0.3}N$/AlN DBR structure centered at 280nm. In addition to the issues related to cracks and dislocations, one major issue is related to the limited bandwidth. In fact, the bandwidth does not exceed 13nm in such systems.

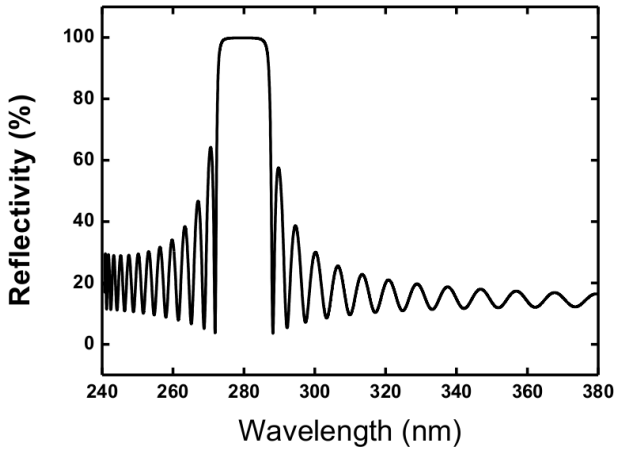

Figure 37: Simulated reflectivity spectrum of 40-pair AlN/$Al_{0.7}Ga_{0.3}N$ DBR at 280nm.

Toward the difficulty to reach high-reflectivity large-bandwidth DBRs with high structural quality in the UV region, the development of new boron-based materials is fundamental.

BGaN/GaN DBRs: First, BGaN materials were associated with GaN materials to achieve high-reflectivity structures. These structures take advantage of the previously reported large refractive index contrast [7]. Figure 38 presents the theoretical maximum reflectivity for $B_{0.013}Ga_{0.987}N$/GaN DBR calculated using the measured BGaN dispersion model. It is compared to $Al_{0.22}Ga_{0.78}N$/GaN and lattice-matched $Al_{0.82}In_{0.18}N$/GaN [79] structures. This figure illustrates the possible use of BGaN/GaN DBRs as an alternative of the conventional AlGaN/GaN structures.

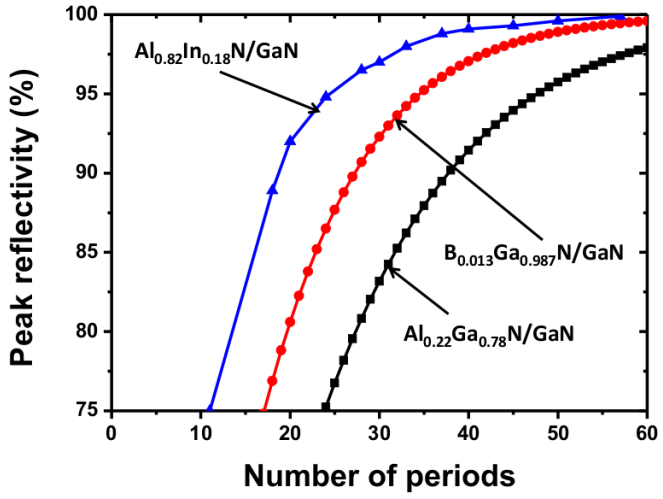

Figure 38: Theoretical maximum reflectivity for $Al_{0.82}In_{0.18}N$/GaN, GaN/$B_{0.013}Ga_{0.987}N$, and $Al_{0.22}Ga_{0.78}N$/GaN as a function of number of pairs.

In fact, as confirmed in the simulations, the BGaN/GaN systems can displace the conventional AlGaN/GaN structures with low aluminum content. It is observed that with only 1.3% boron incorporation in the GaN layers, higher reflectivities in comparison to the $Al_{0.22}Ga_{0.78}N$/GaN system with equivalent number of periods are achieved. Additionally, thanks to the low lattice mismatch which does not exceed 0.2%, these structures suffer less from crack and dislocation issues. However, the BGaN based structures can not achieve the performances that can be reached using lattice-matched

$Al_{0.82}In_{0.18}N$/GaN systems. That is explained by the fact that their refractive index contrast is higher than in BGaN/GaN system. Nevertheless, the AlInN based structures are not practical, mainly because of the different growth temperatures between materials forming the stack. This feature makes the development of such mirrors too time-consuming.

BAlN/AlN DBRs: The BGaN-based structures can theoretically achieve highly reflective DBR structures with a small number of periods, as shown in Figure 38. However, because of their low bandgap energies, these material systems cannot be used in the deep-UV region. Driven by the demonstrated large refractive index contrast with the boron incorporation in the AlN layers and the BAlN transparency, BAlN materials can be used to develop DBR structures in the deep-UV range. In this chapter, no information about the boron content in the solid phase will be given, as this study will be detailed in next chapter. Indeed, the boron content will be only reported in the gaseous form. Figure 39 presents the theoretical reflectivity as a function of the number of periods for BAlN/AlN DBRs for different TEB/III ratios. The central wavelength is 280nm.

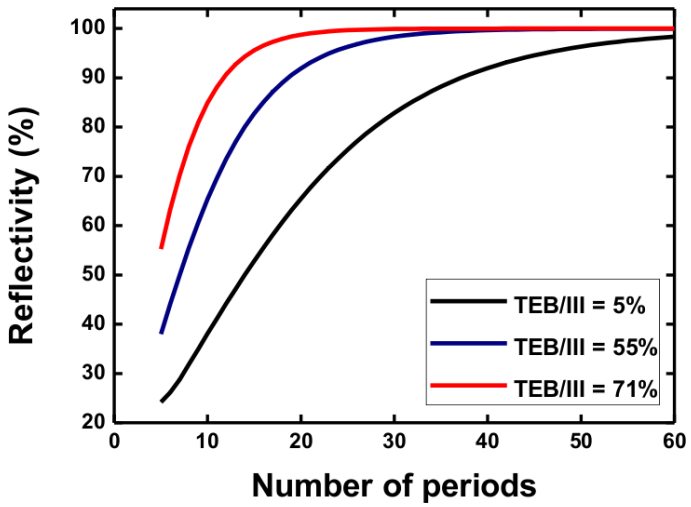

Figure 39: Simulated reflectivity versus number of periods for a BAlN/AlN DBR for different TEB/III ratio. The central wavelength is 280nm.

It is shown that a high reflectivity can be theoretically achieved using this material technology. For instance, with only 10-pair BAlN/AlN DBR, 90% reflectivity

can be achieved. These high reflectivities, combined to the BAlN transparency in the deep-UV region, confirm the possible use of BAlN-based structures for deep-UV DBR applications. The theoretical reflectivity dispersion of a 30-pair BAlN/AlN DBR centered around 280nm is shown in Figure 40. It is shown that 99.9% reflectivity can be theoretically achieved with only 30 periods. The large bandwidth of such structures is another major advantage. For instance, the bandwidth exceeds 22nm in the following BAlN/AlN structure. This study illustrates the potential of the BAlN materials in the development of DBR structures in the UV range. The simulations show better results than AlGaN/AlN system in both numbers of periods and bandwidth.

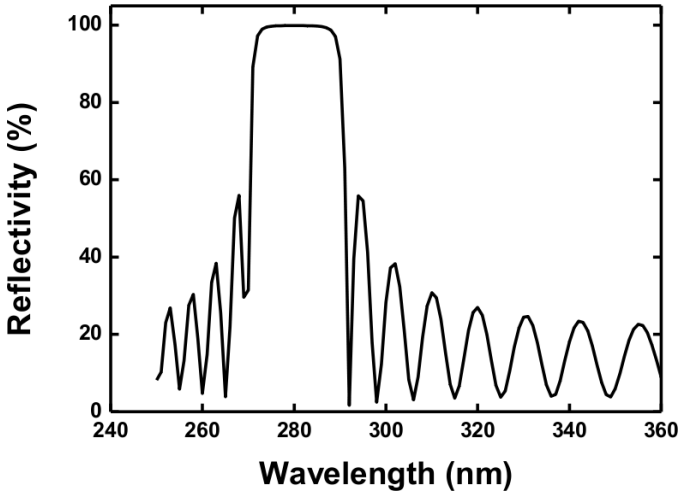

Figure 40: Simulated reflectivity spectrum of a 30-pair AlN/BAlN DBR at 280nm.

BAlN/AlGaN DBRs: Upon the demonstration of interesting theoretical results using BAlN/AlN systems, AlGaN/BAlN systems have been also investigated to take advantage of two major features. They concern the high refractive index contrast and the possible strain compensation in such structures. These features enable high reflectivities with a small number of periods. To confirm this tendency, the reflectivity was simulated as a function of the number of periods for a BAlN/AlGaN DBR for different aluminum incorporation (Figure 41). The central wavelength is 250nm in the different curves. The BAlN experimental refractive index presented in Chapter 4 and the AlGaN refractive

index reported by Brunner *et al.* [5] (Figure 7a) were used. A maximum reflectivity of 90% can be achieved with only 10 periods using BAlN/$Al_{0.7}Ga_{0.3}N$. Depending on the boron content, a specific aluminum content can be applied to develop a strain-free compensated DBR structure.

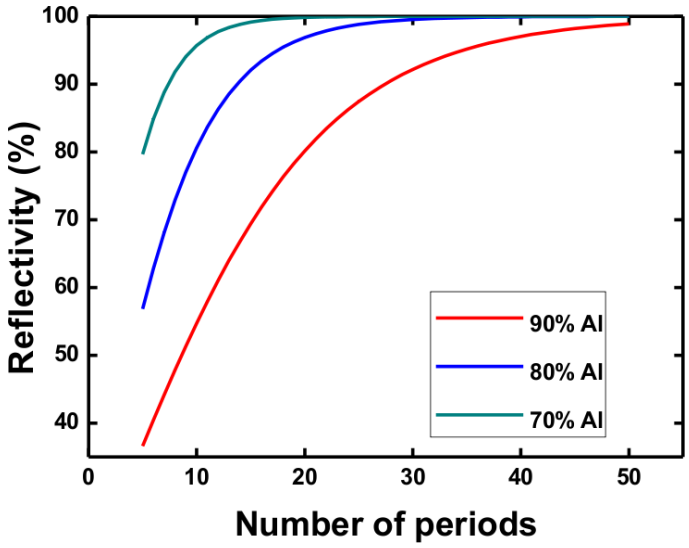

Figure 41: Simulated reflectivity as a function of the number of periods for a BAlN/AlGaN DBR for different aluminum incorporation. The central wavelength is 250nm.

Figure 42 presents a simulated reflectivity of 10-, 20-, and 30-pair BAlN/$Al_{0.8}Ga_{0.2}N$ DBR structures centered at 250nm. A maximum reflectivity of 97% with only 20 periods can be theoretically achieved at 250nm. The bandwidth is 15nm, which is much higher than values in conventional AlGaN/AlN DBRs. Additionally, these theoretical high reflectivities cannot be achieved using conventional AlGaN materials in the deep-UV region.

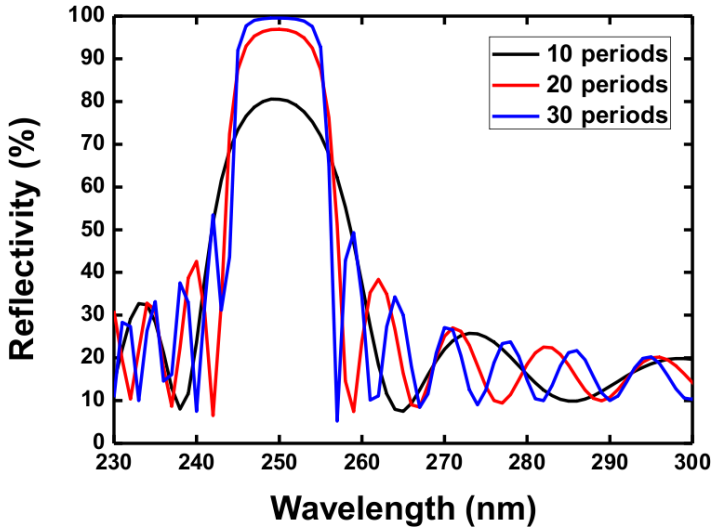

Figure 42: Simulated reflectivity spectrum of 10/20/30-pair $Al_{0.8}Ga_{0.2}N$/BAlN DBR at 250nm.

BAlN/GaN DBRs: Following the promising simulations using BAlN/AlGaN and BAlN/AlN systems, BAlN/GaN systems were also investigated to take advantage of the extremely large refractive index contrast between these materials. However, despite this advantageous feature, the lattice mismatch is also very high, which would affect the structural quality of the DBR stack. Additionally, because of the strong absorption of GaN materials below 370nm, this system can be only used in the near-UV range. Figure 43 illustrates the simulated reflectivity as a function of the number of periods for a BAlN/GaN DBR for different boron content. The simulations use 400nm as a central wavelength. A maximum reflectivity of 99% can be achieved with less than 10 periods. Additionally, this system exhibits more than 70nm bandwidth, suggesting this system as an efficient candidate in the development of near-UV VCSELs.

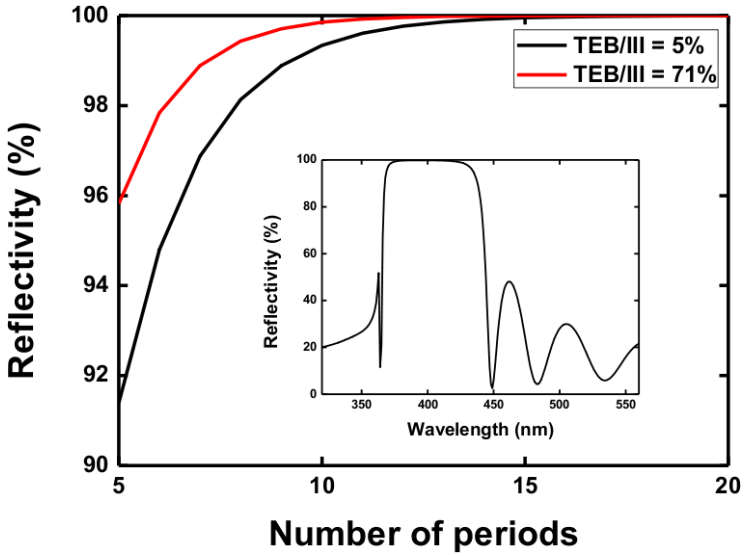

Figure 43: Simulated reflectivity versus number of periods for a BAlN/ GaN DBR for different boron incorporation. The central wavelength is 400nm. The inset figure presents the simulated reflectivity for a 10-pair BAlN/GaN structure using 71% as a TEB/III. The bandwidth exceeds 70nm.

As a general conclusion, the potential of BAlN-based materials was demonstrated in this section as a possible replacement of the conventional AlGaN materials. It was shown that the achieved reflectivities using BAlN-materials are much higher than those achieved using conventional systems. Additionally, conversely to the limited bandwidth in conventional DBRs, the bandwidth is much higher using boron-based structures. The development of monolithic growth of the VCSEL device can also be considered through the replacement of the conventional dielectric mirrors with the boron-based structures. To confirm this tendency, a deep material characterization of (B)AlGaN materials will be described in next chapter toward their use in the distributed Bragg reflectors operating in the UV range. The DBR experimental results will be discussed in Chapter 5.

CHAPTER 4

MOVPE GROWTH STUDY AND MATERIAL CHARACTERIZATION OF (B)ALGAN ON GAN AND ALN TEMPLATE SUBSTRATES

This research was motivated by experimental results that provided some evidence of strong refractive index modification by a few percent boron incorporation in AlN and GaN layers [7]. This research was also driven by some challenges in the development of highly reflective and large-bandwidth DBRs in the UV region. Therefore, we studied more thoroughly the refractive index of boron-based materials, and we argued for the potential use of this material system for the development of versatile DBRs. Additionally, the boron-based materials present several unique properties. The properties include high hardness, excellent chemical stability, and optical transparency over a wide spectral range [128]. Therefore, boron-based nitride alloys have been recently proposed for purposes such as lattice matching to available substrates and applications involving bandgap engineering [129, 130].

The increasingly interest for boron-based alloys has highlighted the need to improve our understanding of the properties of BGaN and BAlN epilayers.

The research work presented in this dissertation is divided in three parts. First, the DBR reflectivity has been simulated by taking into account the experimental refractive index dispersion of the nitride alloys (Chapter 3). Second, the growth and characterization of the wide-bandgap B(Al,Ga)N material systems have been investigated (this chapter). Finally, following the success in achieving unique optical properties of boron-based materials, the boron-based highly reflective DBRs have been grown and characterized for the first time (Chapter 5).

4.1 MOVPE growth conditions study

For the purpose of UV-VCSEL development, we have first focused this study on the optimization of growth conditions of AlGaN, BGaN, and BAlN alloys through MOVPE. Then, to evaluate their application in DBR structures operating in the UV range, deep structural and optical study were combined

Afterward, the boron incorporation in GaN and AlN materials was noticeably investigated. Boron-based materials benefit from several unique properties making them suitable for DBR structures operating in the UV range. However, there are several challenges involving the growth of B(Al,Ga)N alloys including spinodal decomposition [131] and phase separation [132]. In fact, because of the low solubility of boron in GaN and AlN [133], and the fact that BN is highly dissimilar to GaN and AlN in terms of lattice constant, it is commonly accepted that single phase B(Al,Ga)N alloys are not attainable above a few percents of boron [131].

All the epitaxial growths were performed at 1000°C at a total pressure of $133*10^2$Pa (100 Torr) using 100% nitrogen as carrier gas. All growths were carried out on 0.9µ m thick AlN and 3.5µm thick GaN on sapphire template substrates.

The surface morphology of the grown B(Al,Ga)N layers was analyzed by optical-contrast microscopy, atomic force microscopy, and scanning electron microscopy. Double-crystal X-ray diffraction was used to analyze the strain and structural quality. XRD analysis also enabled the calculation of the boron composition in the solid-phase layers using X'Pert Epitaxy software.

Boron distribution along the growth direction in the B(Al,Ga)N layers was evaluated by SIMS. The optical properties (refractive index, absorption coefficient, and optical bandgap) have been extracted using both spectroscopic ellipsometry and light transmission/reflection measurements.

4.2 Study of the growth conditions of GaN materials

In this section, the different growth conditions performed on the GaN layers to obtain a good structural and morphology quality are described. Toward this study, the temperature, the pressure, and the V/III ratio were varied in a series of GaN layers grown on GaN template. It was observed that increasing the thickness of the GaN layers increases the V-pit size and deteriorates the GaN surface morphology. Therefore, the same 300nm film thickness was used in all samples.

In a first step, the growth temperature was kept constant, and the pressure and the V/III ratio were varied, as shown in Figure 44.

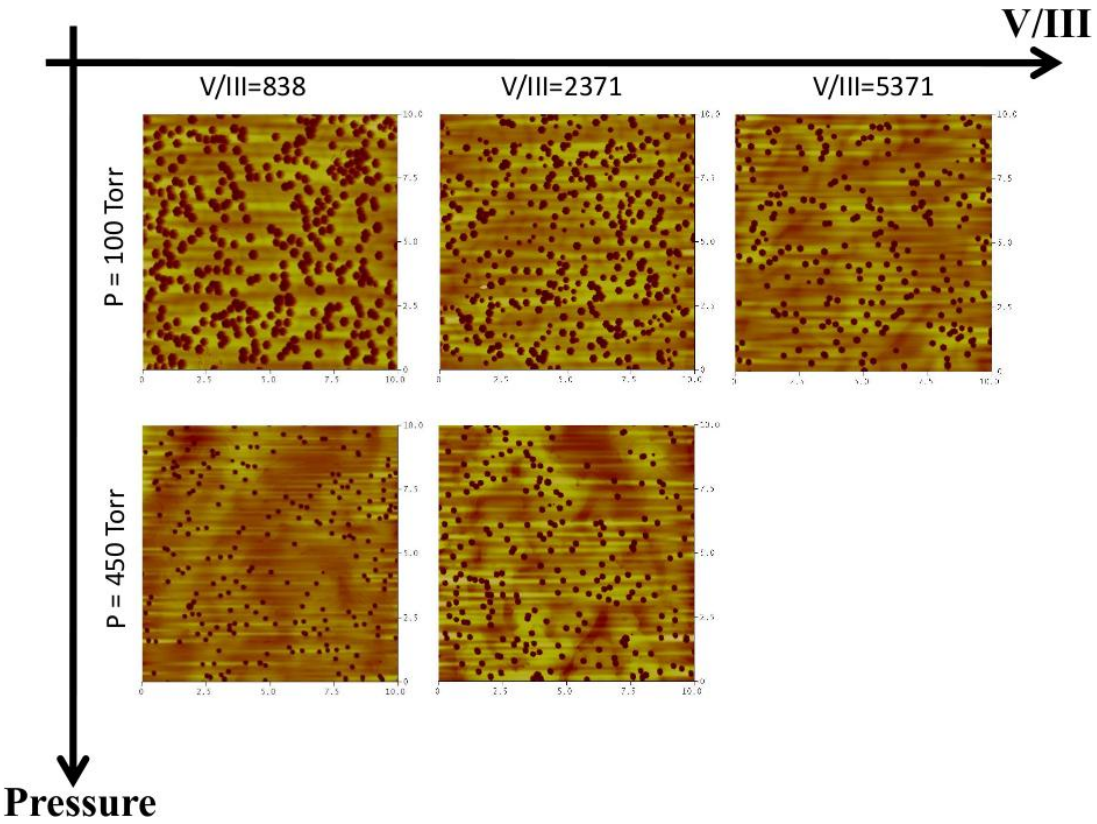

Figure 44: AFM surface morphology of GaN layers grown using different P and V/III growth conditions.

The V/III ratio and the growth pressure have a strong influence on the surface morphology of the GaN layers. In fact, the surface morphology of the high-pressure GaN exhibits a much smoother surface than that of low-pressure GaN. In fact, at a V/III ratio

of 2371, the surface roughness goes from 8nm to 2nm when the GaN growth pressure is increased. Additionally, the low-pressure layers exhibit low V-pit size and density. Similarly to the growth pressure, a clear reduction of the V-defects size and density was observed when we increase the GaN V/III ratio from 838 to 5371. The defect density decreases from $3.7*10^{8}cm^{-2}$ to $2.4*10^{8}cm^{-2}$.

To investigate the impact of the growth temperature, two GaN layers were afterward grown at 1000°C and 1040°C, respectively. Both layers were grown at a pressure of 450 Torr and 838 V/III ratio. The surface morphologies of GaN films with an increasing growth temperature are shown in Figure 45. Similarly to pressure and V/III ratio, we concluded that temperature was critical in obtaining good surface morphology. In fact, low growth temperature leads to an increased surface roughness and large V-pit densities. In fact the RMS and the dislocation density were decreased from 0.7nm and $2.25*10^{8}cm^{-2}$ to 0.2nm and $1.8*10^{8}cm^{-2}$, respectively.

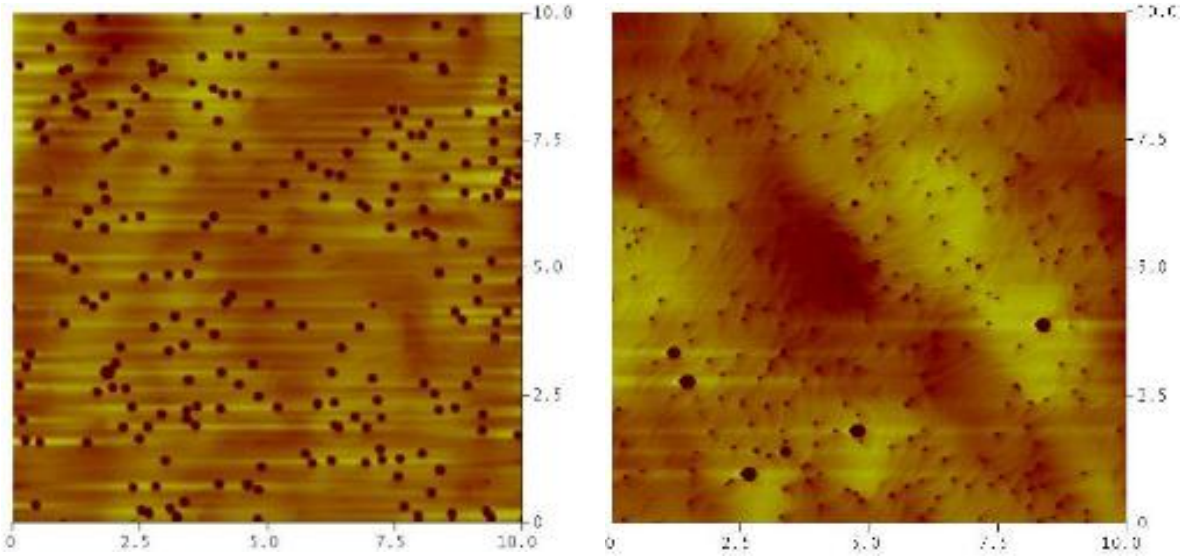

(a) (b)

Figure 45: AFM surface morphologies of GaN films grown at (a) 1000°C and (b) 1040°C.

In conclusion, the influence of growth temperature, pressure, and V/III ratio on the surface morphology of the GaN layers was described in this section. This study of the

different growth conditions was the starting point in the growth of the different ternaries. For heterostructures such as distributed Bragg reflectors, it is also important to take into consideration the optimum growth conditions of the different layers in the superlattice. That leads to a difficult compromise, noticeably in the case of boron-based structures. In fact, it was demonstrated that the optimum growth temperature and pressure for boron based materials are 1000°C and 100 Torr, respectively. The V/III ratio will be adjusted accordingly the boron content.

4.3 Aluminum gallium nitrides materials

4.3.1 MOVPE AlGaN growth

In comparison to boron-based materials, the epitaxy of AlGaN layers is well mastered, and a conventional growth temperature is around 1000°C. However, the AlGaN growth suffers from the large lattice mismatch reaching 2.5% with GaN and AlN templates. The lattice mismatch limits the Al content and the thickness of the AlGaN layers. For instance, grown on GaN template, thick $Al_{0.3}Ga_{0.7}N$ layers exhibits 0.8% lattice mismatch, and consequently tend to relax by the formation of dislocations and cracks. Cracks can be observed above 50nm thickness.

Toward this study, a series of $Al_xGa_{1-x}N$ films with a wurtzite structure and variable growth conditions (temperature, pressure, V/III ratio, gas flow, solid-phase aluminum composition, etc...) were grown on GaN substrates. The thickness of the grown AlGaN layers varies from few nm to one µm.

The Al content in the solid phase in AlGaN varies linearly with the TMAl/(TMAl+TMGa) ratio, as shown in Fig. 46. Additionally, the AlGaN growth rate, depicted in the inset of Fig. 46, is linearly governed by the total III elements flow (TMAl+TMGa). This linear variation of Al content suggests a reduction of the parasitic reactions during the AlGaN growth, and that the growth conditions were optimized to achieve both composition and thickness control.

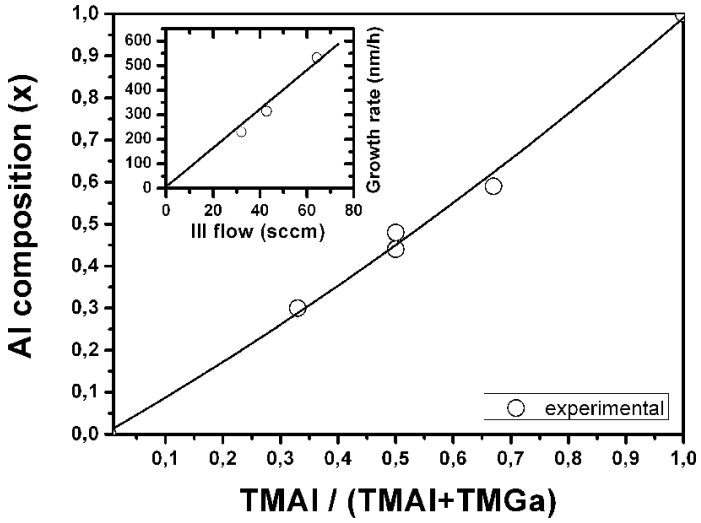

Figure 46: Al composition plotted as a function of TMAl/(TMAl+TMGa) ratio.

4.3.2 AlGaN relaxation critical thickness

As mentioned earlier, low-dislocation density and crack-free AlGaN films are one of the key elements in obtaining efficient UV light emitters. In fact, the presence of dislocations or cracks is highly detrimental in DBRs and VCSELs. Therefore, because of the lattice mismatch between AlGaN and nitride substrates, there is a certain thickness that cannot be exceeded to avoid relaxation strain.

Despite the extensive research to develop native substrates including GaN, AlN, and their alloys as free-standing wafers, none has reached the stage of commercial availability with reasonable price and wafer size. Therefore, it is fundamental to accurately determine the critical thickness to study the thickness limit of the DBR structures. Toward this purpose, different theoretical models such as Griffith, Matthews and Blakeslee, Merwe, People, and Fisher models [134, 135, 136, 137] were tested. Since these models were not all developed for AlGaN/GaN multi-layers, the models were applied in the AlGaN configuration by modifying the different intrinsic parameters (Poisson ratio, burger vector, and lattice parameters). However, a large difference between the different models was noticed. Therefore, obtaining an experimental critical thickness curve is fundamental.

To draw the AlGaN experimental critical thickness, the critical thickness curve of AlGaN has been calculated for two Al incorporations of 36 and 16%. The Al composition and film thickness were determined using both (00.2) 2θ-ω scans and (11.4) RSM maps. Figure 47 presents the RSM measurement for the two different fully-strained AlGaN layers, for which the thickness is below the critical thickness. RSMs are dominated by the AlGaN and GaN peaks, which are not offset in the horizontal direction, suggesting no relaxation in the total film. By increasing the film thickness by few nm, cracks and relaxations were observed by optical microscopy and RSM measurements, respectively.

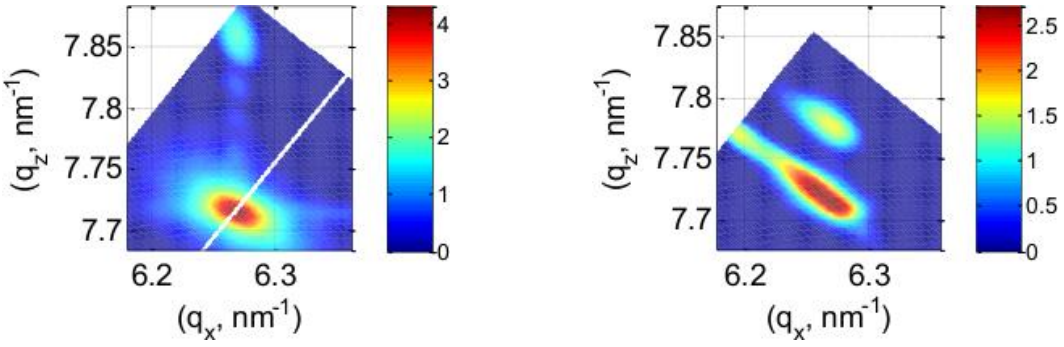

(a) (b)

Figure 47: RSM measurements for (11.4) reflection of (a) $Al_{0.16}Ga_{0.84}N$ and (b) $Al_{0.36}Ga_{0.64}N$ films grown on GaN template.

Figure 48 presents optical microscopy images of different $Al_{0.36}Ga_{0.64}N$ samples with different thicknesses. In contrast to the 56nm, films which doesn't exhibit any cracks, cracking appears when exceeding the critical relaxation thickness. The 56nm AlGaN film is fully strain-free, as shown in Figure 47b.

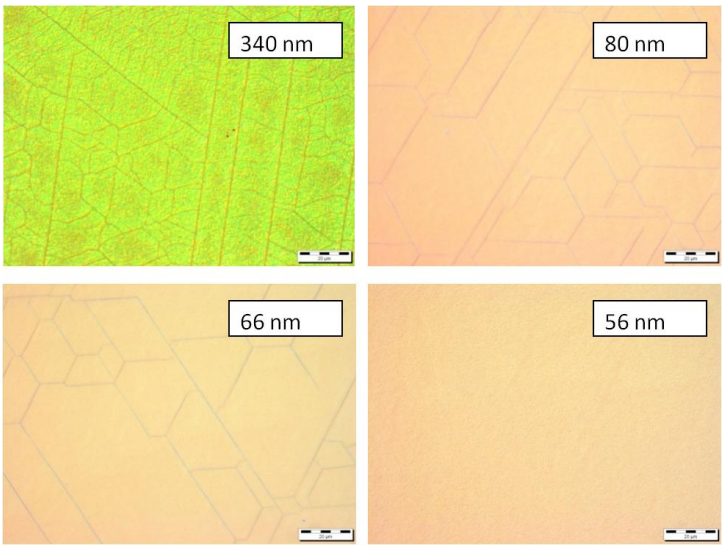

Figure 48: Optical microscopy images of different $Al_{0.36}Ga_{0.64}N$ samples with thickness varying from 340nm (presence of cracks) to 56nm (no cracks).

To draw the final experimental curve, the starting point was the Griffith model [134]. The model was then adjusted accordingly to the experimental achieved points (16 and 36%) through the modification of the intrinsic parameters. The Griffith model is governed by Equation 46.

$$H_c = \frac{\Gamma}{Z.M.\varepsilon^2}, \tag{46}$$

where Γ is the surface energy of the crack plane, M is the biaxial modulus, Z is a coefficient related to the decrease of the elastic energy, and ε is the misfit parameter.

The experimental AlGaN critical thickness as a function of aluminum molar fraction is shown in Figure 49. In this figure, several critical thickness measurements previously published in the literature are reported together with the experimental curve for comparison. A good agreement between all these values is found. Therefore, the curve can be used in a confident way to evaluate the critical thickness of AlGaN on GaN template.

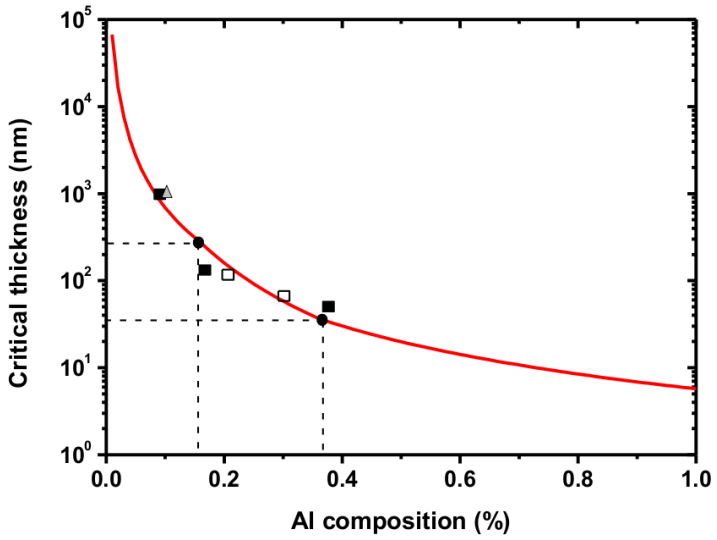

Figure 49: The experimental critical thickness for AlGaN layers grown on GaN templates. Experimental data are added: (●) from this work, (Δ) from [10], (■) from [11], and (□) from [12].

The obtained curve was afterward validated by growing a 60nm $Al_{0.3}Ga_{0.7}N$ material. The film was fully strained and crack free. Cracks were observed when few nanometers were added while keeping the same aluminum content. Therefore, the experimental critical thickness is reliable.

4.3.3 AlGaN/AlN multi-quantum wells

As mentioned earlier, because of the large strain between AlN and GaN materials, Al rich AlGaN/GaN superlattices grown on AlN templates can induce cracks and high dislocation density [11]. Consequently, light-emitting devices using AlGaN/GaN MQWs suffer from low output optical power and short carrier lifetimes [138]. Furthermore, absorption in the underlying GaN reduces the external quantum efficiency of UV light emitters. A large number of publications has reported the growth of thick crack-free AlGaN layers on sapphire using AlGaN/AlN buffer structures, but only few publications have addressed the growth of AlGaN/AlN MQWs on AlN template substrates [139, 140, 141] or on bulk AlN [142]. Such UV transparent AlN template substrates enable the growth of Al-rich structures with a reduced global structure strain. Al-rich AlGaN alloys

have the capability of emitting at short wavelengths down to 210nm, which makes them very useful for the active region of UV VCSELs [143]. Additionally, since the Al compositions in the wells and barriers are close in AlGaN/AlN MQWs, the structures are favorable for abrupt interfaces in comparison to conventional AlGaN/GaN structures. In this study, AlGaN/AlN MQWs have been grown at low pressure and with 100% nitrogen as a carrier gas.

Several MQWs structures were grown on thick AlN templates. In this section, the results related to two samples (T251 and T252) are presented. The MQWs consisted of 5 periods of AlGaN/AlN grown without any interruption between the wells and barriers with an aluminum well ratio of 44% and 48%, respectively. They were designed to achieve deep-UV luminescence at 280nm and 270nm, respectively. High-resolution XRD measurements were applied to determine the nominal thickness and crystallography of the AlGaN/AlN MQW samples.

Figure 50 presents 2θ-ω scans for samples T251 and T252 measured in the vicinity of the (00.2) reflection of AlN. Diffraction profiles are dominated by the strong peak from AlN pseudo-substrate. Superlattice peaks associated with the presence of MQWs structures can be seen for both samples. The interstitial N-1 fringes (minima), where N=5 is the number of quantum wells, are also visible. The fringes indicate a good interface quality between AlGaN wells and AlN barriers in the MQWs.

MQW periods were determined for these samples by measuring the separation between adjacent SL peaks. The global MQW strain was determined from the separation between the 0-th order SL peak and the AlN substrate peak. The strain is expressed in terms of the d-spacing mismatch in (00.1) direction and is calculated with respect to AlN pseudo substrate layer.

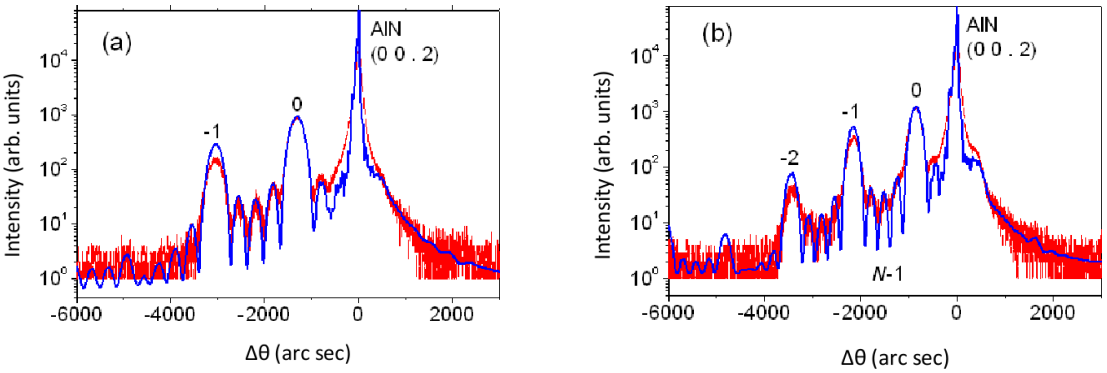

(a) (b)

Figure 50: XRD 2θ-ω scans for AlGaN/AlN MQWs (a) T251 and (b) T252 structures. Strong diffraction peak in the center of the map corresponds to the (00.2) reflection of the AlN pseudo bulk substrate. Red curves correspond to experimental data, and blue curves are results of simulations.

The structural quality of the grown MQW structures has been assessed by RSM. RSM was measured for symmetric (00.2) (Figure 51a) and asymmetric (11.4) reflections (Figure 51b). The FWHM of the rocking curve for the AlGaN layer peak, which is approxiamtely 0.05 deg, is close to that of the AlN substrate. The relative orientation of the AlN and MQW peaks in the asymmetric RSMs indicates that the in-plane lattice parameters of the MQWs and the substrate are the same within the accuracy of the low-resolution measurement. Therefore, we confirm that the MQWs are elastically strained with respect to AlN substrates.

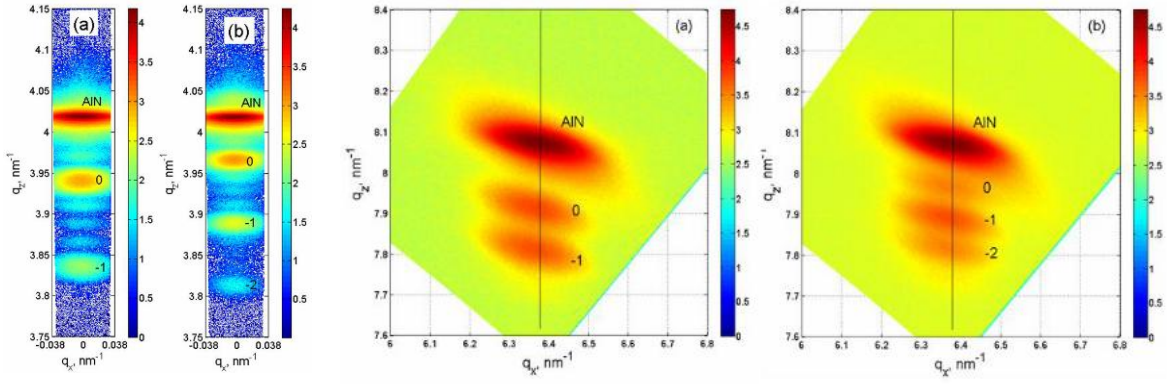

(a) (b)

Figure 51: (a) High-resolution RSM for (00.2) reflection and (b) Low-resolution RSM for (11.4) reflection of AlGaN/AlN MQW T251 and T252 structures.

From the XRD and RSM measurements, thicknesses and composition of the wells and barriers were accurately determined. The resulting parameters of the MQW structures are summarized in Table 6.

Table 6: Samples parameters extracted from XRD measurements.

Sample ID	Well Al ratio (x)	Well thickness (nm)	Barrier thickness (nm)	Well strain in the (00.1) direction (%)
T251	0.44	6.2	3.3	3
T252	0.48	6.2	6.67	2.7

Optical characterization using white light transmission and photoluminescence was performed on samples T251 and T252. Results are shown in Fig. 52 for both samples. To extract the optical bandgap values from transmission profiles, experimental data was fitted using the O'Leary-johnson-Lim model for interband transitions in disordered materials [144]. The optical bandgaps were determined to be at 288nm for T251 and 280nm for T252. The bandgap difference for the two structures is approximately 0.123 eV.

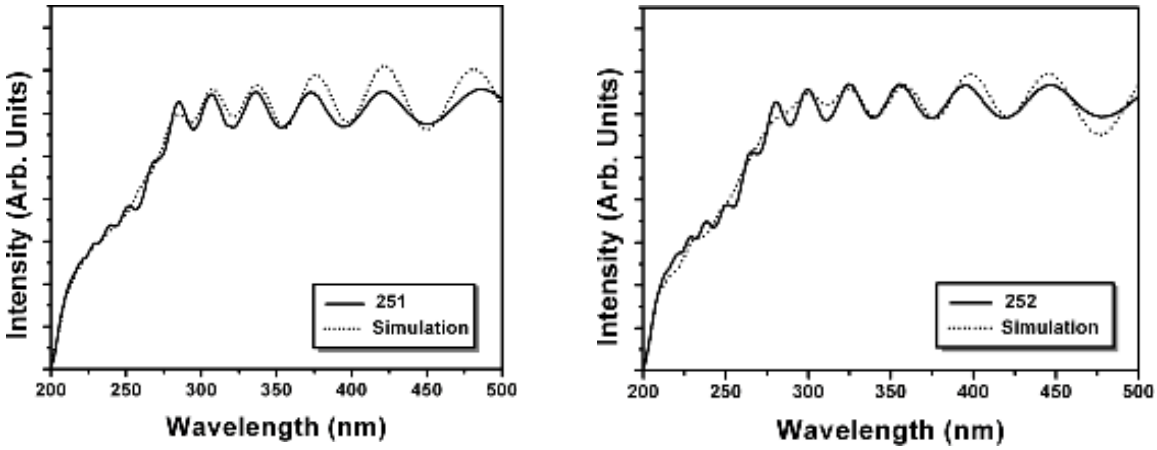

(a) (b)

Figure 52: Transmission spectra of sample (a) T251 and (b) T252. Solid curves are the experimental data, and dotted ones are simulations.

The photoluminescence spectra of the MQWs at room temperature are shown in Figure 53. From these observations, the PL transitions are 280nm and 273nm, respectively. The maximum PL intensity is slightly blue-shifted in comparison to the transmittance edge. This blue shift can be explained by the photo-excited carrier screening effect caused by the high excitation power.

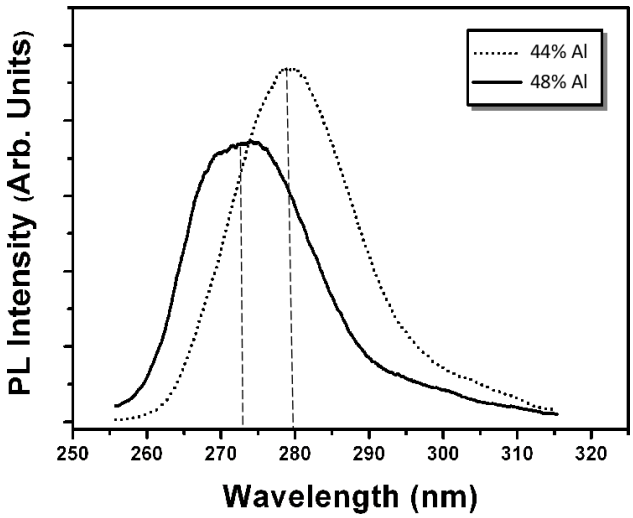

Figure 53: PL spectra of MQW samples with an excitation by the 5th harmonic (213nm) of a mode-locked Nd:YAG laser.

To compare the PL measurements to the theoretical values, the QWs transition energies were extracted from envelope function calculations [145]. In this model, both piezoelectric field and exciton binding energy are included. The calculated variation of PL transition versus piezoelectrical field is shown in Figure 54. For comparison, the measured bandgaps from both PL and transmission of samples T251 and T252 (horizontal lines) are plotted in the same figure. A good fit between the simulation and measurements is obtained for the field value of 900 and 930 kV/cm, respectively. S. Marcinkevicius *et al.* [145] reported similar values of electric field for AlGaN MQW. However, these numbers are much smaller than the electric field obtained from the theoretical calculations. This difference has been reported by several authors [145, 146]

and has been attributed to the uncertainty of the theoretical calculations because of strains, spatially localized exciton states, or impurities in investigated materials.

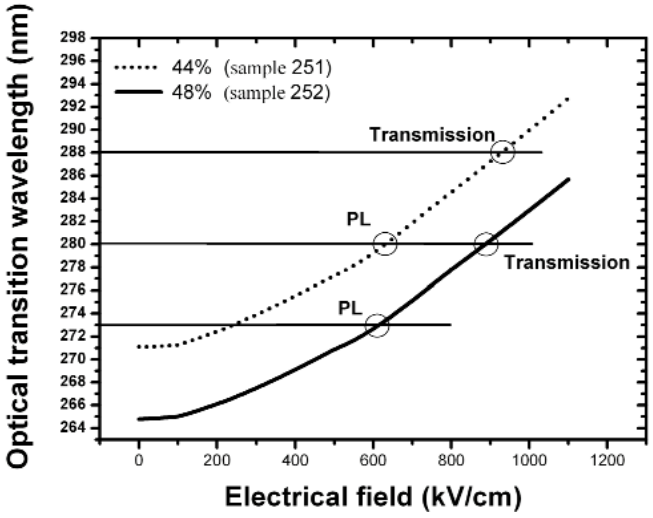

Figure 54: PL transmission wavelength plotted as a function of piezoelectrical field in the MQWs. Dotted line corresponds to sample T251, and solid one to sample T252. Horizontal lines present transmission bandgap positions for both samples.

In conclusion, the preliminary results achieved using AlGaN/AlN MQWs are summarized in this section. The obtained results show the possibility to grow high-quality AlGaN/AlN MQW structure. This AlGaN/AlN MQW is a good candidate for the active region of a VCSEL device operating in the UV range.

4.4 Boron gallium nitrides materials

4.4.1 MOVPE BGaN growth

Despite their attractive properties, boron-based materials have not been intensively studied in comparison to AlGaN alloys. This is mainly explained by the fact that the growth of high-quality material is generally hampered by phase separation and spinodal decomposition issues, also referred to "unstable mixing region". Therefore, the growth of high structural and morphological quality BGaN alloys remains nowadays challenging. Figure 55 presents the number of publications per year concerning the

different nitride alloys. The figure illustrates the weak interest of the nitride scientific community for boron-based materials research in comparison to conventional AlGaN, InGaN, and to a lesser extent AlInN materials (source: Web of science).

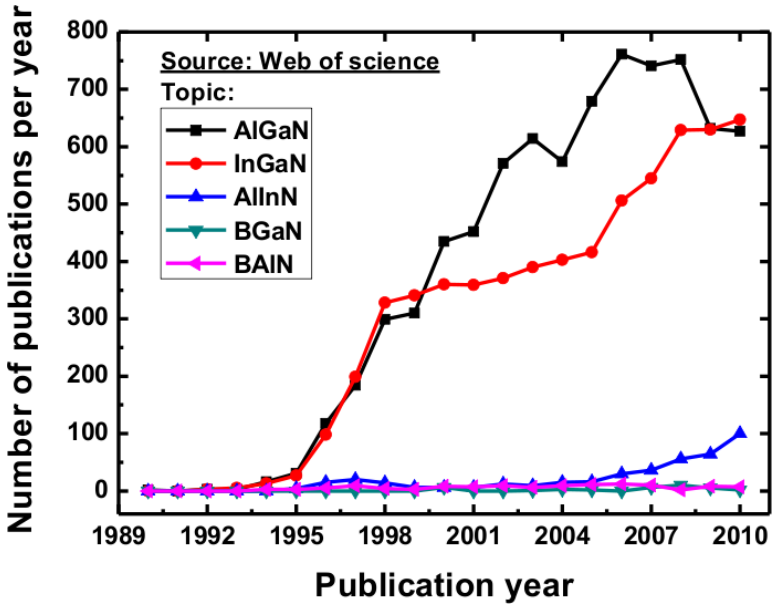

Figure 55: Number of publications for the different ternaries in the nitride system (source: Web of science).

Toward this study, a series of $B_xGa_{1-x}N$ films with a wurtzite structure and different solid-phase boron composition were grown on c-axis oriented 0.9µm thick AlN on sapphire template substrates. The typical thickness of the grown BGaN layers, deduced from in-situ laser reflectometry measurements, was approximately 160 nm. The AlN template enables the optical characterization of BGaN layers, which would otherwise experience an overlap with the bandgap and lattice parameters of conventional GaN/sapphire substrates. When increasing the boron content, the $B_xGa_{1-x}N$ growth rate remains nearly constant around 1200nm/h, as the growth rate is dominated by the gallium flow.

Figure 56 illustrates the relationship between the boron content in $B_xGa_{1-x}N$ in solid phase and the ratio of $\frac{TEB}{TEB+TMGa}$ in gas phase. The B content of $B_xGa_{1-x}N$ epilayers at the given ratio in gas phase deviated from the linear dependance (y=x). This linear line represents the maximum incorporation efficiency of 100% to form $B_xGa_{1-x}N$ in solid phase with no pre-reaction in gas phase.

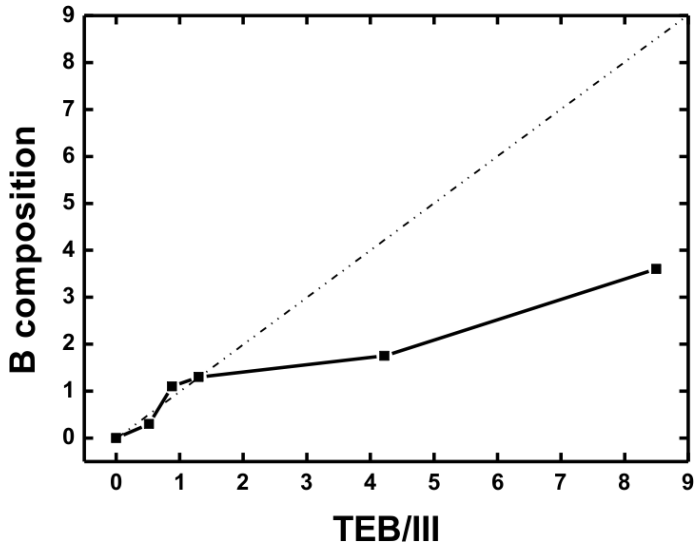

Figure 56: Boron incorporation of $B_xGa_{1-x}N$ in solid phase versus TEB/(TEB+TMGa) ratio in gas phase.

To evaluate the boron distribution along the growth direction, SIMS analysis was carried out on a BGaN film grown on GaN template. The concentration of boron and gallium as a function of the layer depth is shown in Figure 57. The profile of boron concentration is constant in the BGaN layers, indicating an excellent distribution of the boron along the growth. The abrupt drop of boron profile corresponds to the BGaN/GaN interface. The shift-phase variation of boron profile with respect to gallium underlines that the boron element sets well in the Ga site.

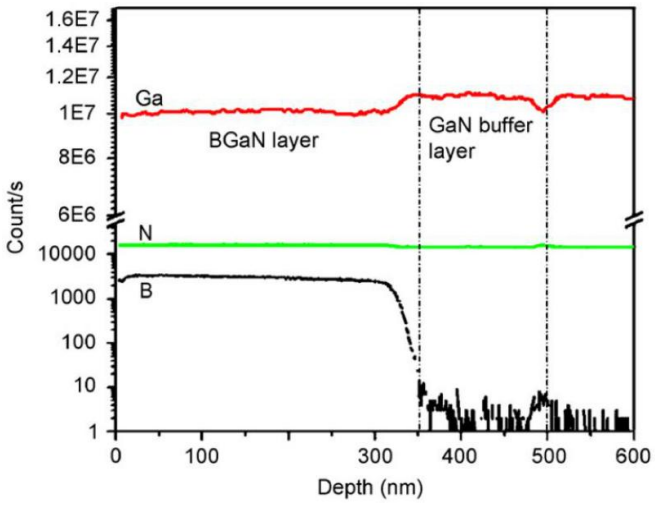

Figure 57: SIMS profile of a BGaN layer grown on GaN substrate.

4.4.2 Morphological and structural characterizations

A 2θ-ω scan of a BGaN film for symmetric reflection is shown in Fig. 58a. The angular separation between the two peaks corresponds to the out-of-plane lattice mismatch between the BGaN layer and AlN template. The measured RSMs for the (11.4) asymmetric reflection is shown in Figure 58b. RSMs are dominated by the BGaN and AlN peaks, which are offset in the horizontal direction, with the shift corresponding to the degree of relaxation. That suggests a fully relaxed BGaN layer with respect to AlN. The average boron content in the ternary BGaN films was calculated using Vegard's law [27] and varies between 0 and 1.7%.

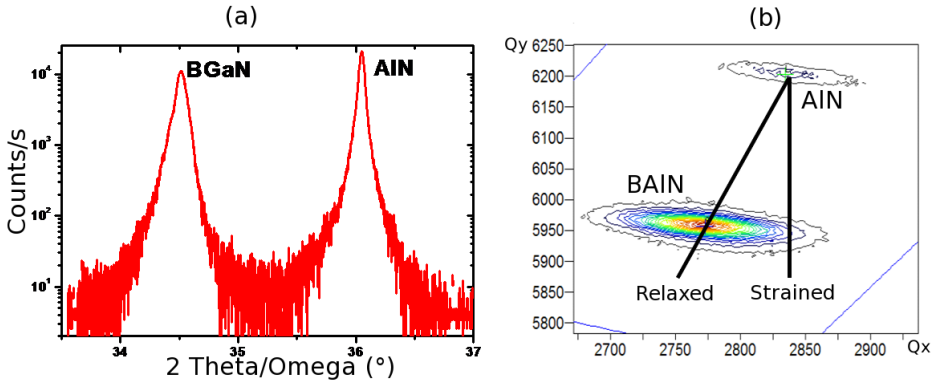

Figure 58: (a) XRD 2θ-ω scans and (b) low-resolution RSM for (11.4) reflection for BGaN films.

Figure 59 presents AFM images of the surface of the $B_xGa_{1-x}N$ materials for 0%, 0.3%, 1.1%, and 1.3% of boron content. The images show that the BGaN surface exhibits a 3D morphology. The root-mean square roughness of the surface for the different samples decreases from 14 to 4nm as the B content in BGaN increases. The roughness will be taken into consideration in the following study related to the calculation of the BGaN optical properties through ellipsometry.

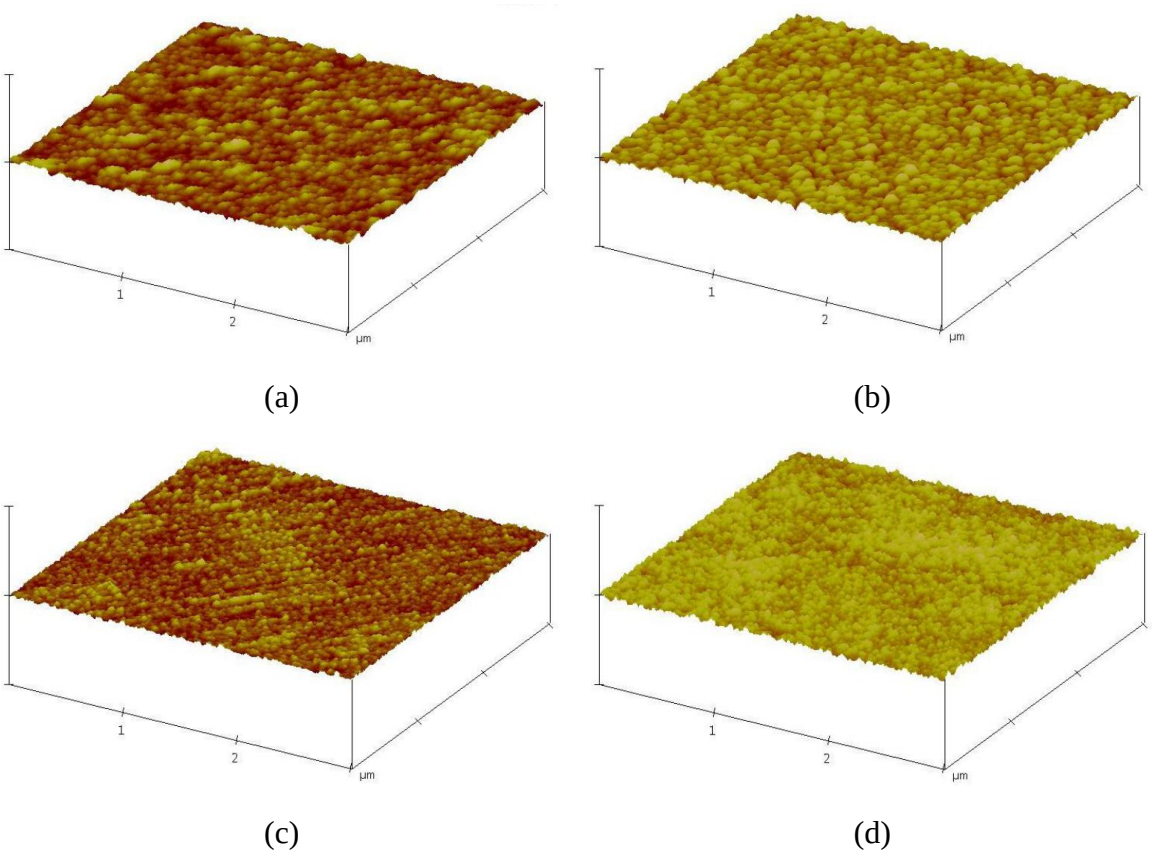

Figure 59: 3D AFM images of BGaN films grown on AlN templates with different boron content (a) 0%, (b) 0.3%, (c) 1.1%, and (d) 1.3%.

Figure 60a presents a HAADF-STEM image of a BGaN film containing 0.7% of boron. HAADF was used to take advantage of its sensitivity to the local atomic number of the atoms. For clarity, GaN template substrate layer has been marked on the figure. A columnar structure is observed in the figure. Each column consists of a grain of

approximately 100nm width. The lateral size of the grains measured on this sample is in good agreement with AFM measurements, confirming the 3D growth. The contrast of the BGaN layer is relatively homogeneous and comparable to the GaN layer, suggesting no compositional inhomogeneity in the layer. Nevertheless, clear lines perpendicular to the growth direction are observed on the entire width. To investigate the nature of these defects, atomic resolution HAADF images have been realized on the $B_{0.007}Ga_{0.993}N$ layer (Figure 60a). As observed in the Fourier transform pattern given in Figure 60b, the different spots correspond to the superposition of both Zinc-Blende and wurtzite patterns. By selecting the cubic phase reflections and then applying an inverse Fourier transform, the original image was re-constructed. The obtained image is highlighted in Figure 60c, and it only shows the contribution of the ZB phase. The ZB structured insertions were found to be from a few monolayers to two monolayers thick, which correspond to the elementary ABC atomic stacking characteristic of the cubic phase.

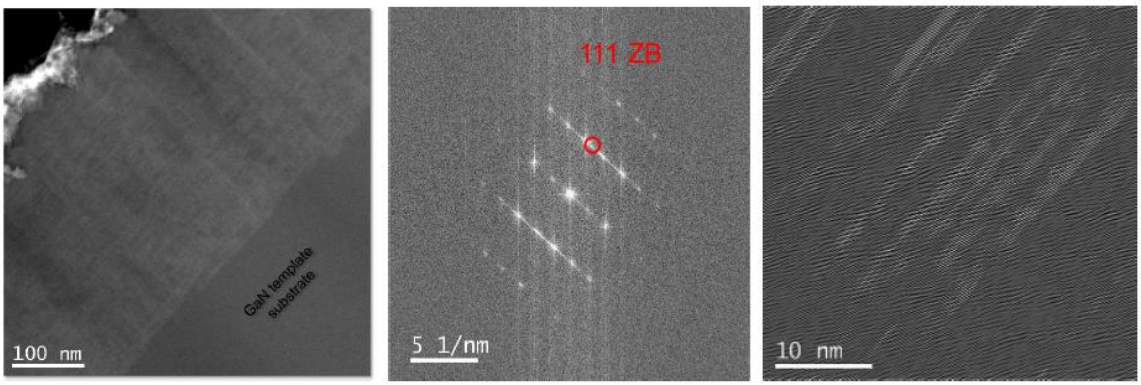

Figure 60: (a) HAADF STEM picture of a 400nm thick BGaN layer containing 0.7% of boron. The zone axis is <11-20>. (b) 2D Fourier transform pattern of the HAADF-STEM image. The wurtzite reflections and the Zinc-blende ones are present. The specific 111 ZB is circled in red. (c) The BGaN layer image reconstructed by mean of inverse Fourier transform evidences Zinc-blende insertions in the BGaN material.

The $B_{0.017}Ga_{0.983}N$ layer was analyzed using a similar procedure. The HAADF-STEM image, shown in Figure 61, presents a columnar growth of the material. The

lateral size of the columns is 100nm. The lateral size of the grains was also confirmed by the surface measurements performed by AFM.

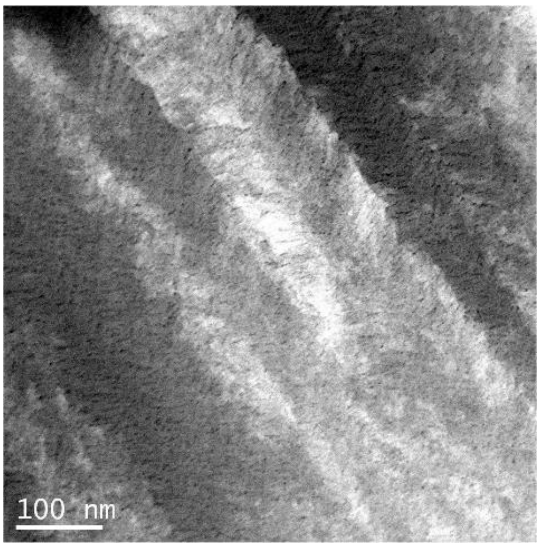

Figure 61: HAADF STEM picture of a thick BGaN layer containing 1.7% of boron.

In addition to the columnar growth that has already been observed at a boron content of 0.7%, the $B_{0.017}Ga_{0.983}N$ sample contains numerous nano-sized clusters. Figure 62a, which presents a HAADF-STEM image, depicts one isolated nano-sized cluster. The clusters distribution is uniform in density along the growth direction. They are homogeneous in size, with a mean lateral size of ~ 3nm. The density of clusters has been estimated to be $10^4 \mu m^{-3}$. Consequently, the ratio of the volume occupied by the clusters over the total crystal volume represents approximately 5%. The individual structural and chemical nature of the clusters was investigated by means of HAADF-STEM and Energy-dispersive X-ray spectroscopy (EDX), as illustrated in Figure 62.

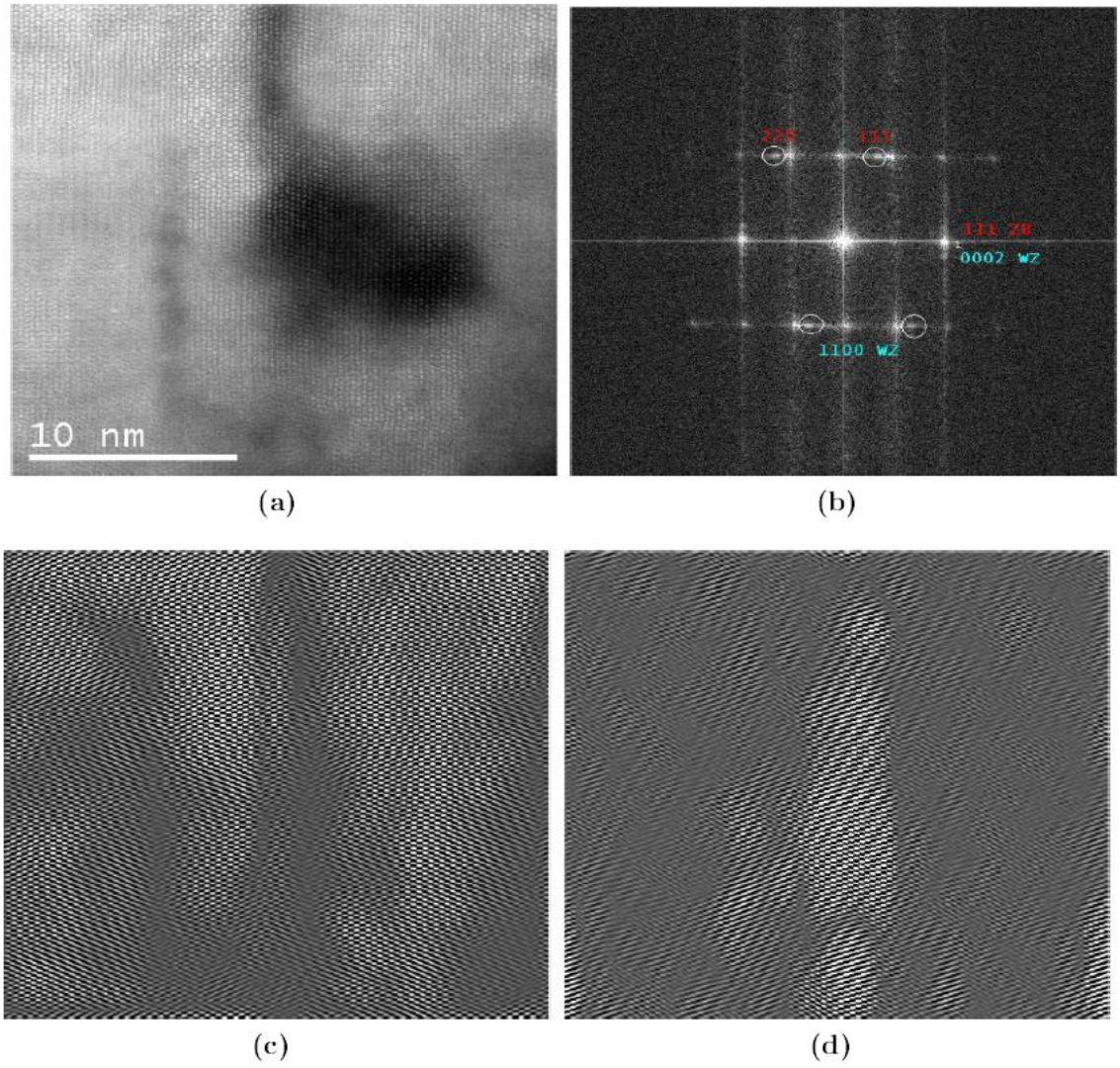

Figure 62: (a) HAADF STEM picture of a single cluster in a 1000nm thick BGaN layer containing 1.7% of boron. The zone axis is <11-20>. (b) Diffraction pattern of the image. Wurtzite pattern and Zinc-blende are present. (c) Inverse Fourrier transform image realized with the specific wurzite spots 1100 and 11-20. (d) Inverse Fourrier transform picture obtained with the cubic -1-11 and 220 spots.

Direct Fourier transform was applied to the image to reveal the reflections of the crystal structure. Results are shown in Figure 62b. Both wurtzite and Zinc-blende phase patterns were identified. It is important to note that the Zinc-blende insertions and clusters are coherent with the surrounding wurtzite matrix. In fact, the 111 reflection of the cubic phase is perfectly aligned with the 0002 refection of wurtzite hexagonal phase along the growth axis. Figures 62c and 62d were reconstructed by singling out the

specific wurtzite and Zinc-blende reflections. The figures represent the contributions of the wurtzite and the Zinc-blende phases, respectively. The contributions are materialized on each picture by the brighter areas. We concluded that the clusters were composed by ZB-BGaN, coherently embedded in the W-BGaN material.

The dark contrast detected by HAADF STEM on the cubic cluster, observed in Figure 62a, suggests that the local equivalent atomic number (Z) changes dramatically to lower values. That would be consonant with high boron incorporation in the lattice. EDX analysis was then used to clarify the origin of the HAADF contrast. As no particular impurities (O, C, nor Si) that could be responsible of the HAADF dark contrast were detected. The contrast was attributed to the presence of boron. In fact, this light element cannot be detected by EDX. The composition was afterward estimated by measuring the gallium and considering the stoichiometry between the III and V elements. Within the accuracy of this method, the composition was approximately 20 ± 2% of boron inside the cubic clusters.

4.4.3 Optical properties investigation of BGaN materials

The optical properties of BGaN films are investigated in the following study. The properties include the complex refractive index dispersion and the bandgap-bowing parameter calculation.

Figure 63 depicts the photoluminescence signals of the BGaN films considered in this study, compared to a pure GaN reference (black curve). The luminescence of the $B_{0.007}Ga_{0.993}N$ layer occurred at 366nm (red curve) and confirmed a red-shift compared to GaN at 362nm. This red-shift illustrates a decrease of the bandgap, which is in good agreement with previous work [33]. The low PL intensity observed for the $B_{0.007}Ga_{0.993}N$ layer peak ($2*10^3$ versus $1.5*10^4$ for GaN) can be explained by the presence of numerous stacking faults that were identified in the matrix [147]. Increasing the boron content to

1.7% caused the luminescence intensity to vanish. This is likely caused by additional defects in the lattice.

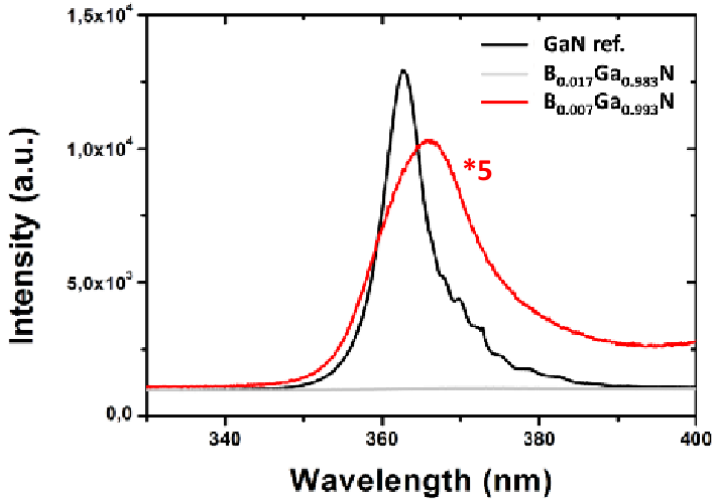

Figure 63: Photoluminescence spectra of BGaN/GaN samples used for this study.

To confirm the red-shift tendency observed in the PL measurements, optical spectroscopy was used to investigate the bandgap variation in the different BGaN films with boron content from 0 to 1.3%. Absorbance spectra $\alpha^2(\lambda)$ have been calculated from transmission and reflection data, as shown in Equation 47.

$$\alpha(\lambda) = \frac{1}{d}\ln\left(\frac{1-R(\lambda)}{T(\lambda)}\right), \tag{47}$$

where d is the BGaN thickness.

The extrapolation of the linear section of α^2 to zero absorption corresponds to the optical bandgap, as illustrated in Figure 64.

The determined bandgap values do not support the interpolated linear dependence between the bandgaps of w-GaN and w-BN and can be only understood by adding a bowing-parameter energy. The calculated experimental bandgap values confirm a strong energy-bowing parameter of BGaN ternary system with b=8 eV [148], which is comparable to experimental and theoretical reported results [33, 149]. The accurate

knowledge of this parameter is very important for bandgap engineering of optoelectronic devices based on BGaN, and also updating the III-N-match software parameters.

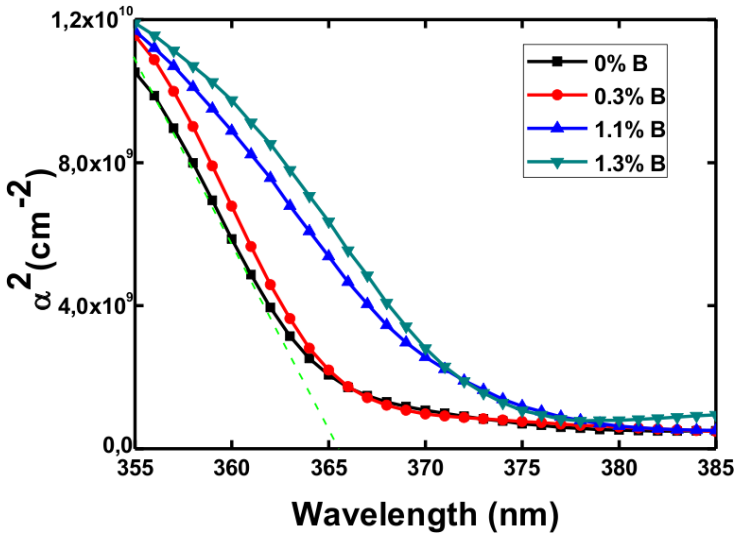

Figure 64: Absorbance spectra of the $B_xGa_{1-x}N$ films for the different samples.

The complex refractive index of the BGaN films is measured using Tauc Lorentz dispersion model. This model has been proved to be a very efficient model when interpreting the spectroscopic ellipsometry spectra [150, 151]. We have also dealt with effective medium theories such as the Bruggeman approximation [152] to take into consideration the measured surface roughness by AFM (Figure 59).

Note that the thickness of the BGaN layers is largely higher than the critical thickness as the growth was performed on AlN templates. While this may rise some concerns with the morphological and structural film quality, such thick layer is required to observe sufficient interference fringes on the reflectivity and ellipsometric spectra.

The investigated refractive indexes are derived from a two-step approach. First, the refractive index dispersion model is extracted by fitting the ellipsometric data by minimizing the mean square error (χ^2) using the Levenberg-Marquadt algorithm. Indeed, minimizing χ^2 leads to the best fit between the experimental ellipsometric/reflectance spectra and the data calculated from the physical model described as a five-phase

(Al_2O_3/AlN/BGaN/Surface roughness/air) system. Second, the obtained index model is smoothed and slightly corrected to fit the interference fringes of the experimental reflectance spectra. Figures 65 and 66 present the experimental and calculated ellipsometric data (Ic and Is) and the reflectance data (R) at different wavelengths.

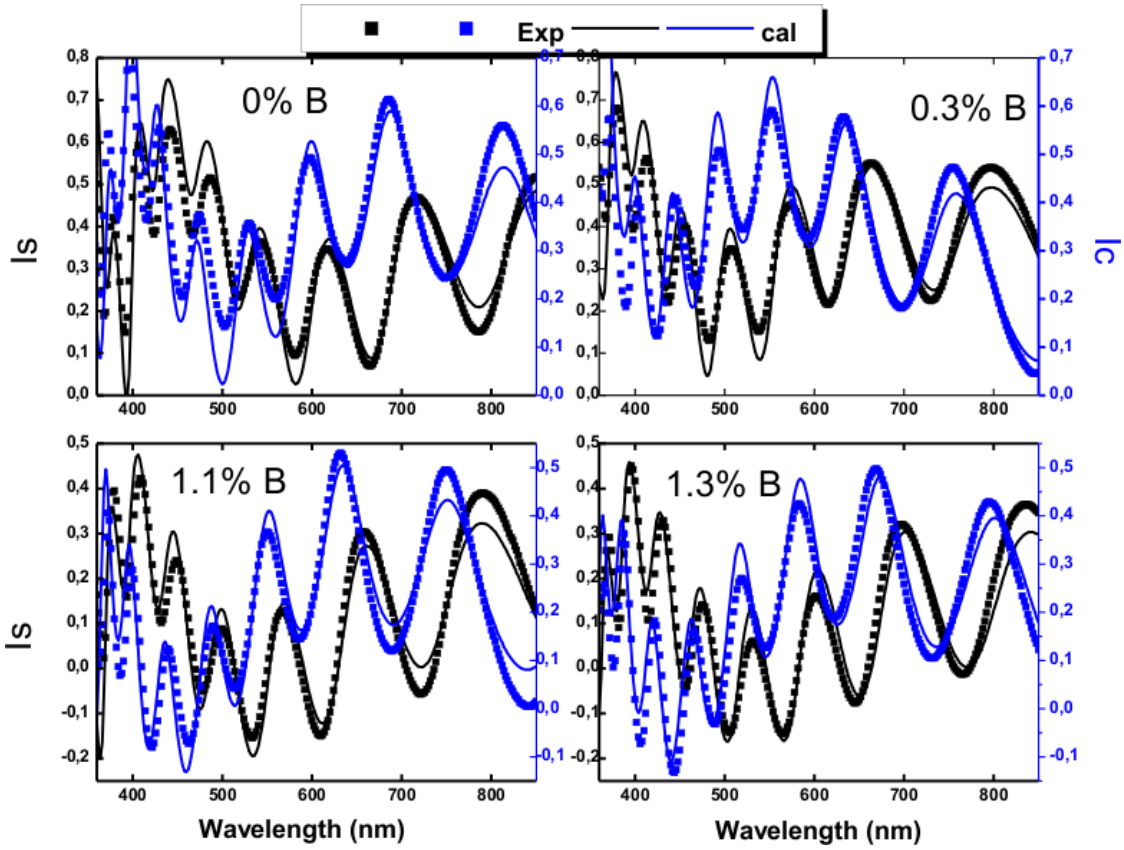

Figure 65: Comparison between measured (dotted lines) and calculated (solid lines) ellipsometric spectra (Is and Ic) for different boron incorporations.

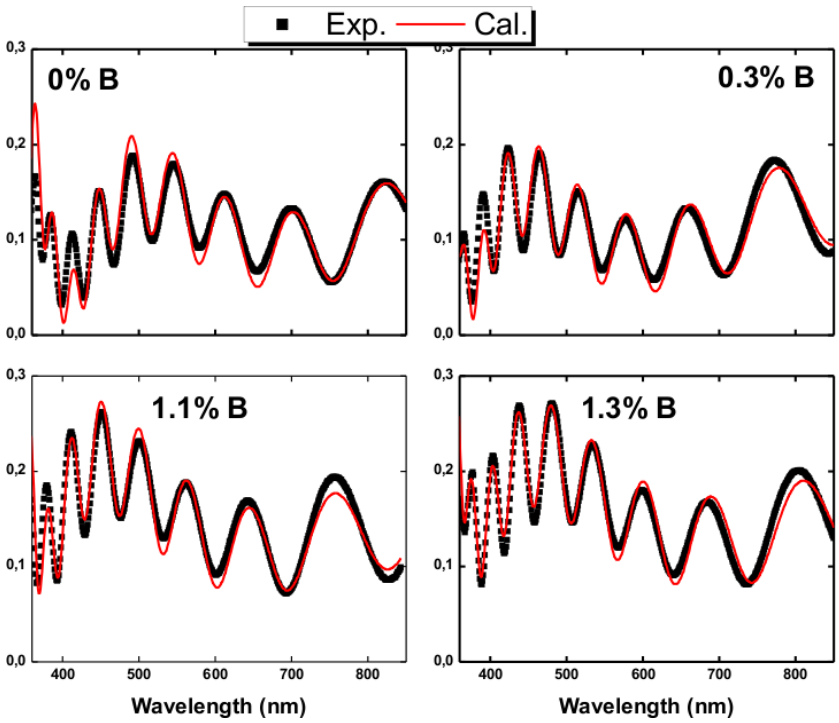

Figure 66: Comparison between measured (dotted lines) and calculated (solid lines) reflectance spectra for different boron incorporations.

The good agreement between calculated (solid lines) and experimental (dotted lines) spectra and the reasonable chi-square value indicate that the assumed model and the obtained optical results are reliable.

Figure 67 presents the resulting refractive indexes and extinction coefficients data for BGaN films for different boron incorporations. It is observed that the refractive index contrast between GaN and BGaN is very high in the range of 0-1.3% boron content. Indeed, by adding only 1% of boron in the BGaN layer, the BGaN/GaN multilayer structure has a refractive index contrast of more than 0.1. The contrast is equivalent to that of AlGaN/GaN with Al=22%, based on AlGaN refractive index data reported by Brunner *et al.* [5]. The obtained large refractive index variation as a function of boron composition can enable the development of highly reflective DBRs with a minimum number of periods. Consequently, with the BGaN/GaN system, a fewer number of

periods is needed to achieve highly reflective DBRs in comparison to conventional AlGaN/GaN DBRs.

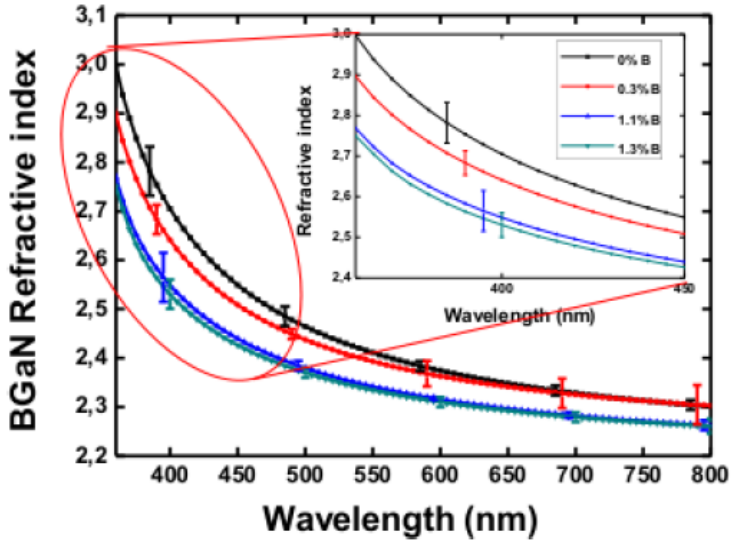

Figure 67: (a) Refractive index and (b) extinction coefficient of $B_xGa_{1-x}N$ film for different boron content.

Additionally, the lattice mismatch between $B_{0.01}Ga_{0.99}N$ and GaN is only 0.2%. Consequently, the crystalline quality of the epitaxial materials for DBR should not bring about the issue of cracking problems associated with AlGaN-based mirrors. Therefore,

the nearly-lattice-matched structure can enable the growth of a high-quality active region. These unique properties can be very interesting for research and development of novel semiconductor DBR with simultaneously high reflectivity and good structural quality. BGaN-based DBRs will be developed in Chapter 5.

4.5 novel Boron aluminum nitride materials

4.5.1 MOVPE BAlN growth

As mentioned in the previous chapters, BAlN is a novel material and only one study has explored its refractive index [7]. Indeed, an accurate knowledge of the optical properties is essential for DBR and laser design. This knowledge is derived from a systematically grown series of samples in which the TEB/III molar ratio in the vapor phase was varied between 0% and 71%. The typical thickness of the grown BAlN layers, deduced from in-situ laser reflectometry measurements, was approximately 150nm.

Depth concentration profiles for Al, B, and N were measured by SIMS, as illustrated in Figure 68. The SIMS profile exhibits a uniform boron distribution along the growth direction, while the Al concentration varies anti-phase with boron. This is an indication that the mixing of Al and B atoms occurs on the sub-lattice of III sites to form an alloy.

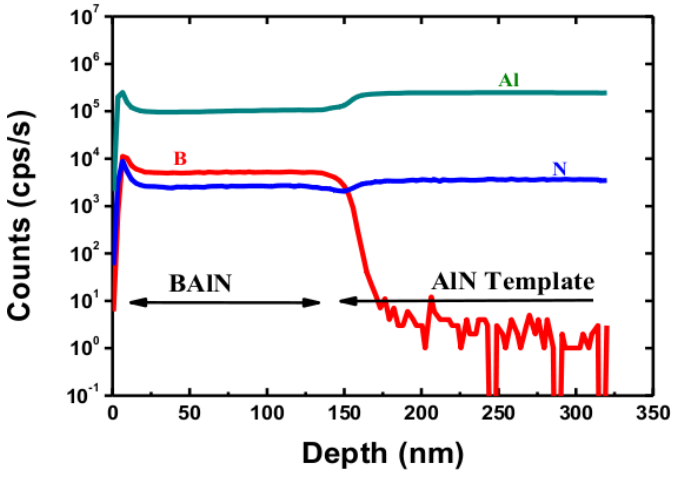

Figure 68: SIMS elemental concentration depth profiles for the B, Al, and N signals for the BAlN layers on AlN template substrates.

4.5.2 Surface morphology and structural characterizations

In this section, the surface morphology of the BAlN layers grown on AlN templates is investigated through AFM and SEM. The samples were investigated first with SEM measurements, as shown in Figure 69.

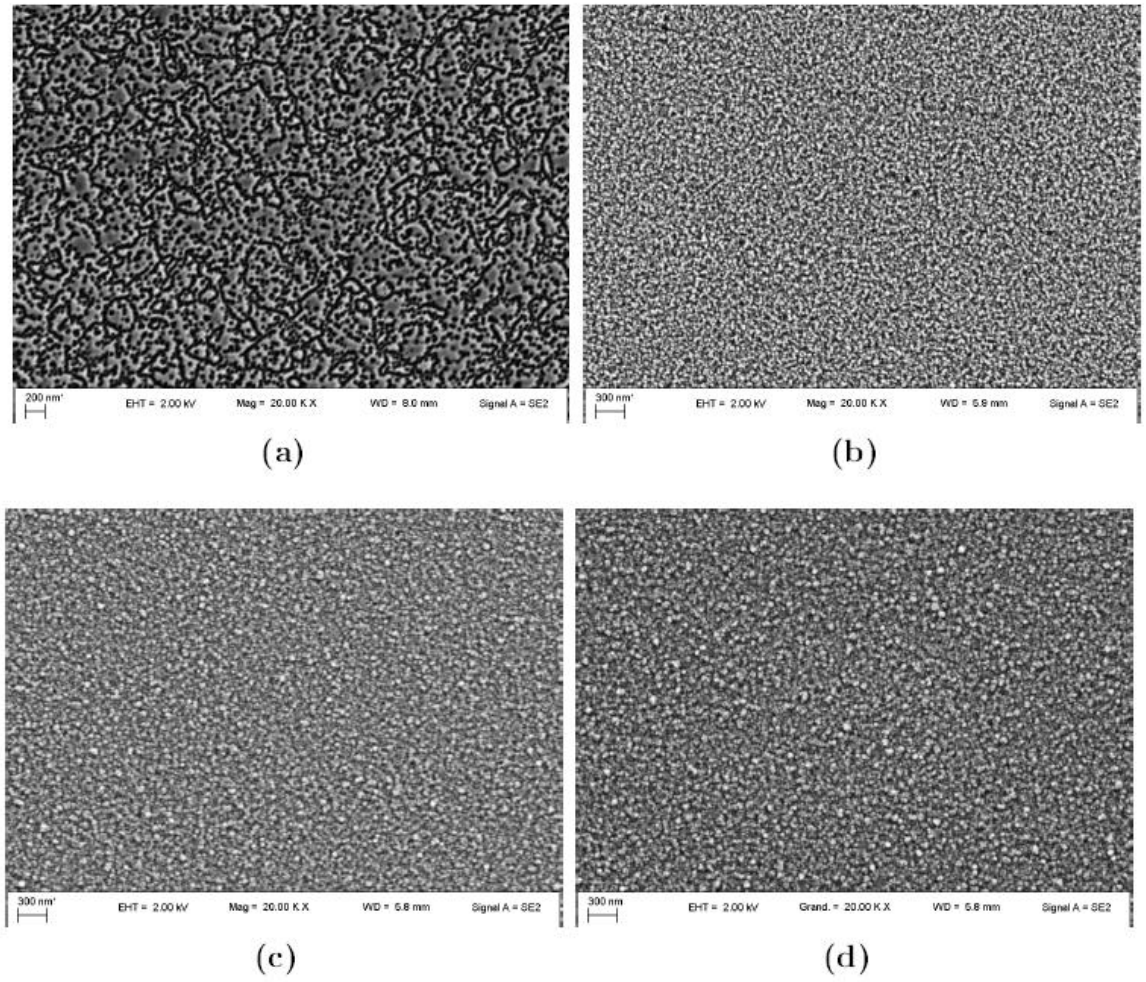

Figure 69: SEM images of the BAlN films grown on AlN templates with different boron content (a) 0%, (b) 3.5%, (c) 26%, and (d) 28%.

Lots of small unshaped grains in different sizes can be observed in the BAlN SEM images. Despite a strong similarity between the different BAlN films, the grains size and density increase when the boron content increases. In fact, the highest boron content film exhibits more distant and bigger grains than the other films.

In Figure 70, 3D AFM images exhibit the surface morphologies of the different BAlN films for different boron content. The measured RMS of the different samples is approximately 4nm, which is comparable to the BGaN films.

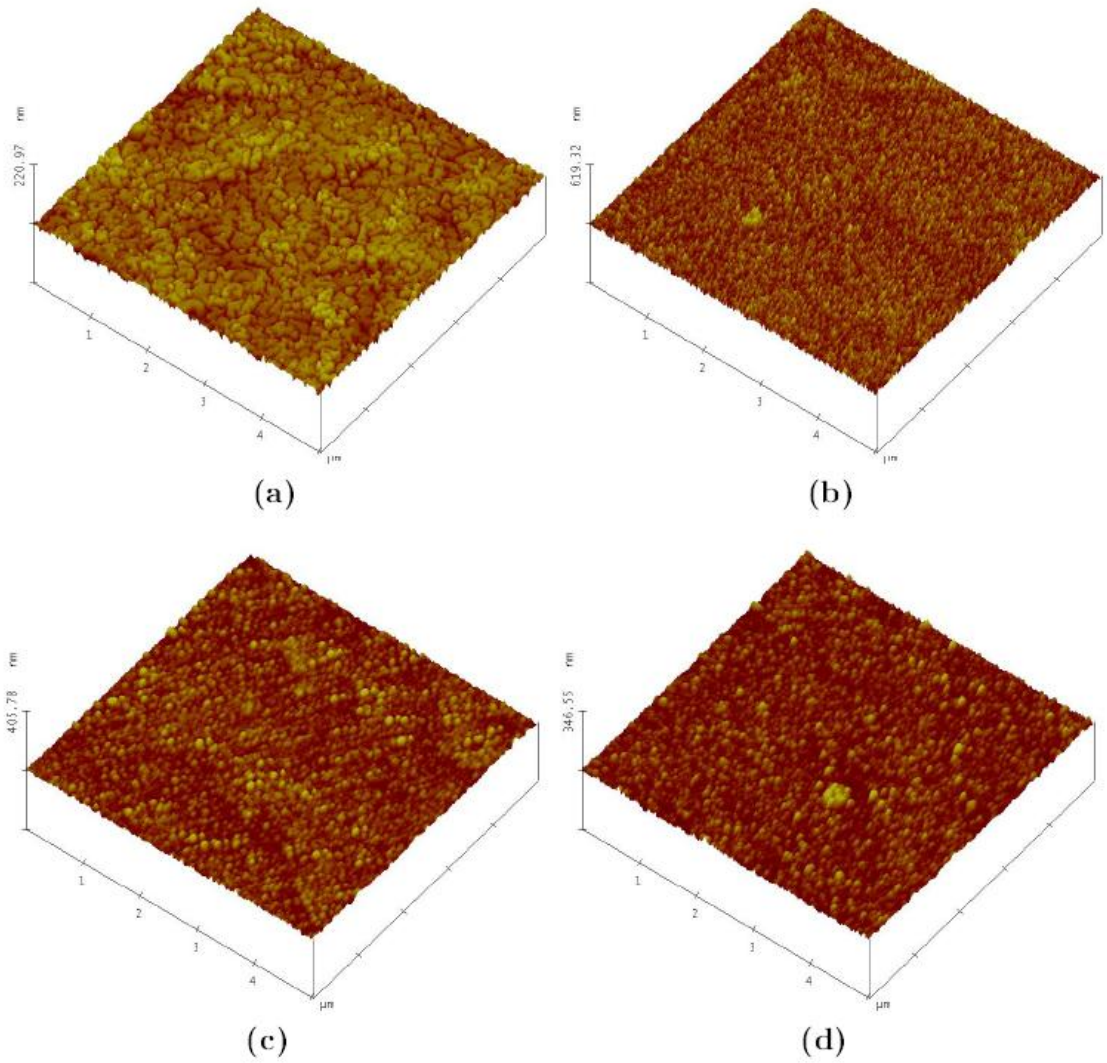

Figure 70: Atomic force microscopy of the BAlN films grown on AlN templates with different boron content (a) 0%, (b) 3.5%, (c) 26%, (d) 28%.

To investigate the structural characterization and evaluate the boron content, XRD measurements were afterward performed on the different BAlN layers. However, the XRD scans did not exhibit any XRD peak related to the BAlN layers. The BAlN structural characterization will be further investigated in Chapter 5 through Raman spectroscopy and electron diffraction pattern.

4.5.3 Boron incorporation analysis using XPS and EDX

The absence of BAlN peak in the XRD scans prevents an accurate measure of the solid phase composition in the BAlN alloys. Therefore, additional analysis techniques were required to measure the boron content, such as XPS and EDX.

In a first approximation, the boron content was investigated using EDX in a BAlN/AlN superlattice with a TEB/III ratio of 38% in the BAlN layers. In fact, although the light boron element could not be detected by EDX, the composition was estimated by measuring the aluminum and considering the stoichiometry between the III and V elements. Within the accuracy of this method, the boron composition was calculated with 2-3% percent error.

Toward this goal, the first AlN layer was used as a reference. Therefore, the stoichiometry ratio of this first AlN was used as a reference for the Al/N ratio in the BAlN ternaries. Consequently, using the BAlN stoichiometry, the boron content can be extracted if we consider that the III/V ratio in solid phase is equal to 1. Experimentally, a series of 6 points in the AlN reference have been first selected, as illustrated in Figure 71. The same measurements were afterward performed on the following BAlN and AlN layers. A strong lack of aluminum in the BAlN layers was observed, suggesting a BAlN alloy. This approach estimated the boron content to be equal to 27-28% with a standard deviation of 3%.

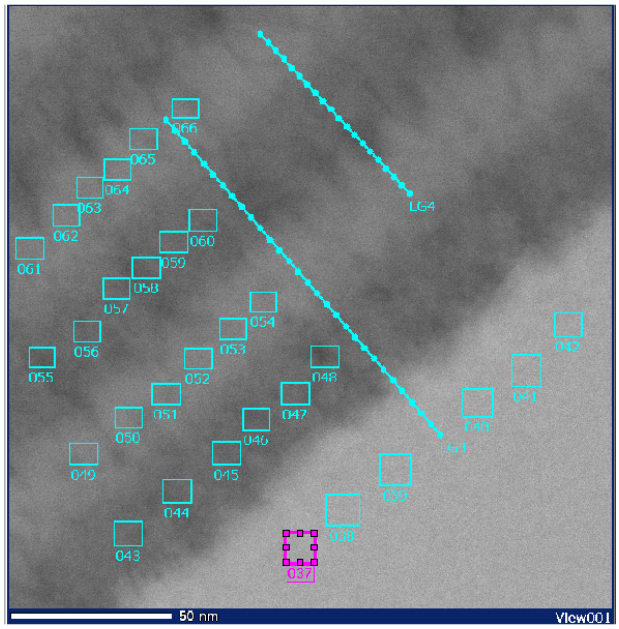

Figure 71: EDX analysis on the BAlN/AlN superlattice.

Then, the behavior of boron incorporation into AlN has been studied by in-depth X-ray photoelectron spectroscopy in the different BAlN samples. In fact, the characteristic peak for the B1s core level at 188 eV could be detected by XPS. The quantification of the different atomic level such as B, Al, and N in the film was estimated using relative sensitivity factors for the used instrument. The tool took into consideration both the transmission function of the spectrometer and the X-ray cross section.

Figure 72 illustrates the photoelectron spectra of BAlN samples in the range 0-1200eV. The X-axis energies were adjusted by the incident X-ray energy. The adjustment took into consideration the reflection of the binding energy of the detected core-shell electron. Several main peaks associated to the different elements indicative of the Al2p, B1s, and N1s core energy levels were observed.

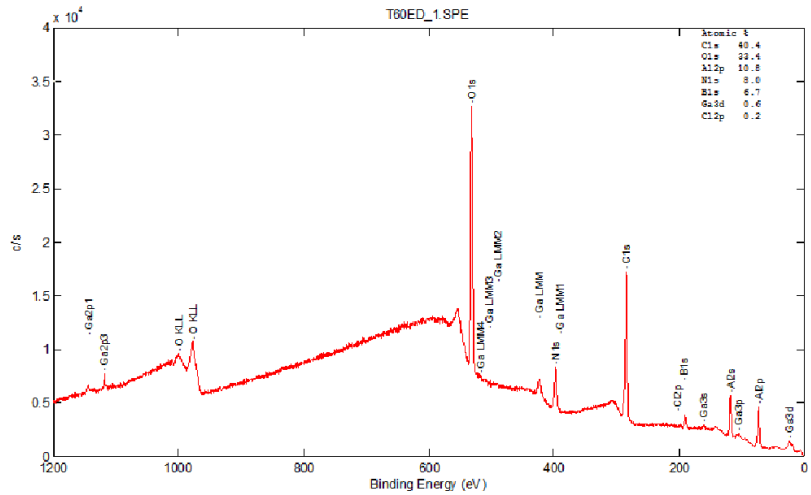

Figure 72: An illustrative over electron-binding energies characteristics of core shell energy levels of the different elements present in the BAlN sample.

A careful in-depth examination of the peak position and shape gives their evolution as a function of the thickness (referred as the sputter time). For instance, the B1s-related XPS peak is observed at 190 eV in Figure 73. The B1s peak is very close to the binding energy of boron in BN, which is equal to 189-190 eV. The figure presents the evolution of the boron concentration as a function of the thickness, enabling the determination of the boron composition in the solid phase.

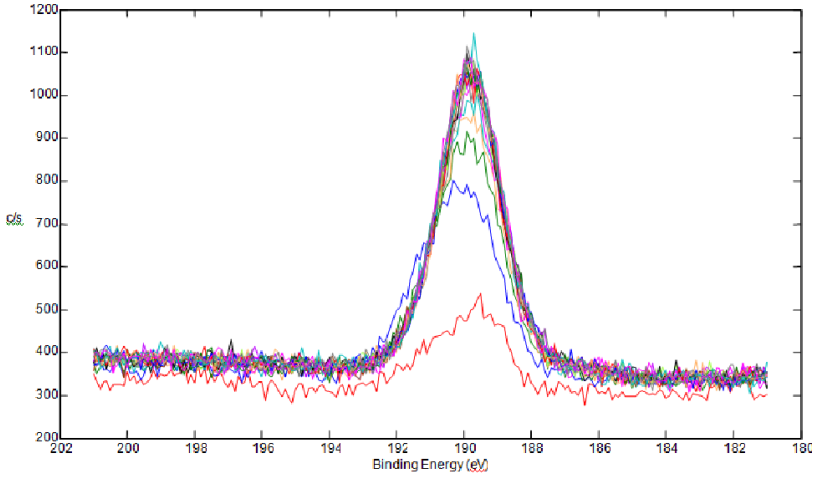

Figure 73: B1s spectra extraction from XPS depth profiles of a BAlN sample corresponding to different sputter depths.

Figure 74 presents the XPS atomic concentration depth profiles of a high-boron content BAlN film (71% of TEB/III in the gas phase). The evolution of the different species present in the film as a function of the sputter time is illustrated. At 6-7 min sputter depth, the Al signal from the BAlN layer increases, while the B signal decreases, suggesting the interface between the BAlN film and the AlN template. The XPS in-depth composition study shows a good homogeneity of the boron content in the film. The depth profile study also shows that the thickness of the grown BAlN layers is approximately 150nm. The measure takes into account the calibrated sputtering speed for such alloys. This estimate of the thickness of the BAlN layer agrees very well with that inferred earlier from in-situ measurements.

Additionally, taking into consideration the atomic concentration of the III and V elements, the boron content in the solid phase was estimated to be 47%. Surprisingly, the boron surface composition was estimated at a particularly high value in comparison to the TEB/III ratio. That suggests a 66% efficiency of the boron incorporation.

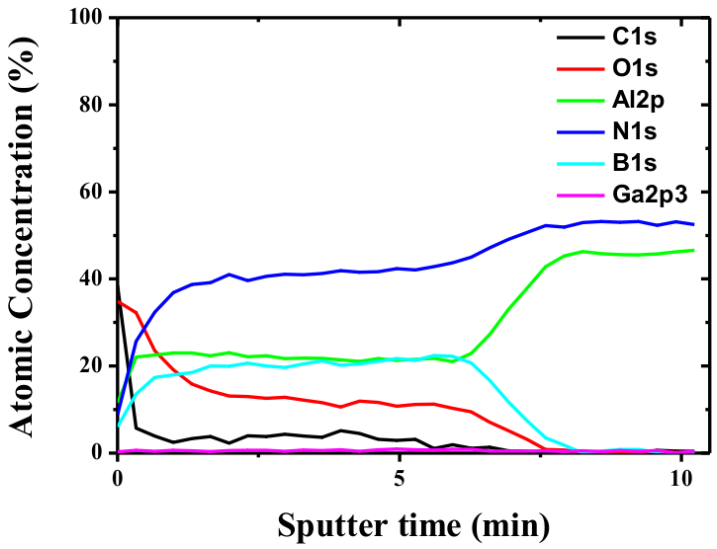

Figure 74: XPS sputter depth profiles of a BAlN film grown on AlN template.

By processing similarly the other BAlN samples, the boron compositions in the solid phase are summarized in Table 7 as a function of TEB/III ratio in the gas phase. The demonstrated values were in agreement with previous calculation using EDX technique.

Table 7: Boron content in the BAlN solid phase as a function of the TEB/III ratio in the gas phase.

TEB/III ratio	0%	5%	38%	55%	71%
Boron content in the solid phase	0%	3.5%	26%	35%	47%

4.5.4 Optical properties investigation of BAlN materials

The BAlN optical properties investigation is undifferentiated from that in the previous BGaN study (cf Section 4.4.3). Similarly to BGaN, the accurate determination of the optical properties of BAlN films is fundamental. It is required to obtain the optimal thickness of the layers in the DBR structure and calculate the required number of periods to achieve a certain reflectivity. In fact, the ellipsometric spectra are analyzed using DeltaPsi2 software to extract the experimental values of refractive index and optical bandgap. The thickness of the deposited BAlN films was chosen to give a sufficient number of interference fringes, which makes the modelisation much easier. The thicknesses were accurately determined beforehand through in-situ reflectometry to get good accuracy of the different parameters listed above. Figure 75 presents the experimental and calculated Ic and Is at different wavelengths for different BAlN samples.

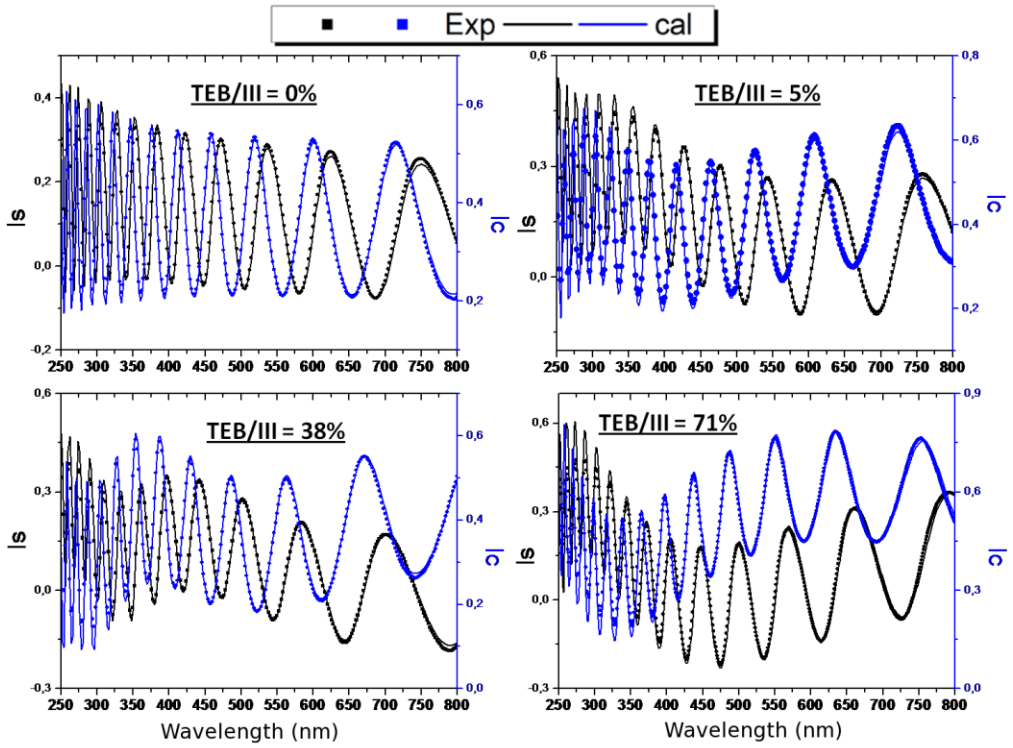

Figure 75: Comparison between the measured (dotted lines) and the calculated (solid lines) ellipsometric spectra (Is and Ic) for different boron incorporations.

The excellent agreement between the calculated (solid lines) and experimental (dotted lines) spectra indicates that the assumed model and the obtained refractive index data are reliable. Figure 76 presents the resulting refractive index data for the BAlN films as derived from the ellipsometry fit. The TL parameters used to draw the refractive index curves are summarized in Table 8. E_g (eV) is the optical bandgap, E_0 (eV) is energy of the absorption peak, C (eV) represents the broadening term associated to the absorption peak, A (eV) is the oscillator strength which is originally linked to density of material, and ε_∞ (dimensionless) is the high-energy dielectric function.

Table 8: Summary of the different Tauc Lorentz parameters extracted from the fit.

TEB/III (%)	E_g	E_0	C	A	ε_∞
0	6.28	7.72	0.22	440.5	1.99
5	6.06	7.03	0.21	521.58	2.14
38	5.80	6.54	0.22	596.21	2.24
55	5.68	6.05	0.25	792.95	2.60
71	5.62	6.63	0.18	240	2.30

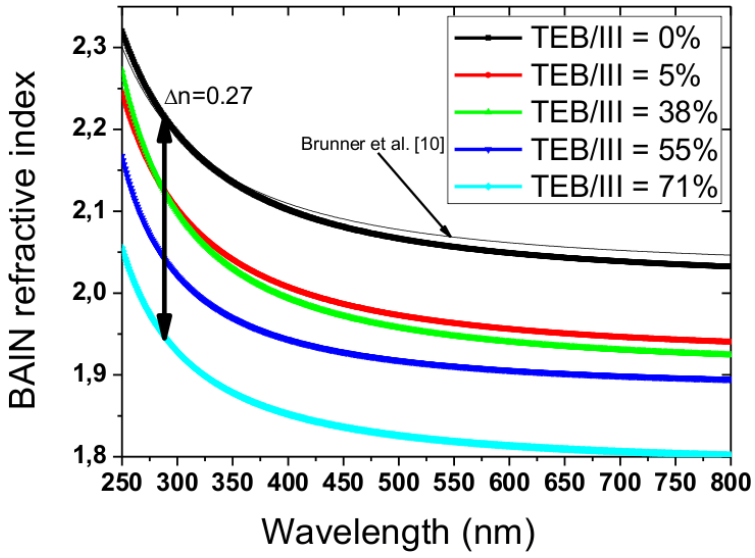

Figure 76: Refractive index versus wavelength of $B_xAl_{1-x}N$ for different samples.

As expected, the refractive index contrast between BAlN layer and AlN template increases with the TEB/III ratio, and the AlN refractive index is in excellent agreement with the previously reported data [5]. At 300nm, the BAlN/AlN structure grown for a TEB/III ratio of 71% can achieve a refractive index contrast Δn of more than 0.25. The achieved contrast is higher than in $Al_{0.5}Ga_{0.5}N$/AlN structure based on AlGaN refractive index data reported by Brunner *et al.* [5].

As a result of the high refractive index contrast and the BAlN transparency, improved DBRs based on BAlN/AlN structures with high reflectivity can be theoretically achieved in the deep-UV region. Additionally, using BAlN/AlN structure, 20 periods are needed to achieve 99% reflectivity and large-bandwidth DBR. In contrast to these boron-based DBRs, conventional AlGaN/AlN DBRs need more than 30 pairs to achieve the same reflectivity. The theoretical results and the comparison between the different systems were already presented in Chapter 3.

CHAPTER 5

STUDY AND OPTIMIZATION OF GROWTH CONDITIONS FOR (B)ALGAN-BASED DBRS

5.1 Near-UV Nitride distributed Bragg reflectors

Until now, $Al_xGa_{1-x}N/Al_yGa_{1-y}N$ and $Al_xIn_{1-x}N/Al_yGa_{1-y}N$ have been the only nitride-based DBRs available to operate in the UV range. However, because of the numerous issues mentioned in the previous chapters, these systems are not adequate for VCSEL applications. Consequently, an innovative DBR design using a new nitride material system based on boron, which can provide simultaneously high reflectivity and high structural quality, is proposed. These boron-based DBR structures are motivated by the demonstrated high refractive index contrast induced by the boron incorporation reported in Chapter 4. This large refractive index contrast is combined with a low lattice mismatch in the BGaN and strong transparency in the BAlN layers.

5.1.1 AlGaN/GaN DBRs

First, AlGaN/GaN DBR structures were investigated to validate our simulation software and confirm the difficulty in achieving highly reflective structures with these conventional materials. Three- and six-pair $Al_{0.16}Ga_{0.84}N$/GaN Bragg mirrors have been grown aiming a 400nm as a central wavelength. The growth was performed in MOVPE on GaN template. During the DBR runs, the AlGaN and GaN layers were deposited at 1000°C and at 100 torr pressure using N_2 carrier gas. To prevent cracking, the number of periods was limited by the critical thickness. Consequently, the number of periods did not exceed six periods. The GaN and AlGaN $\lambda/4$ layers are 39nm and 40nm thick, respectively. The total DBR thickness is approximately 520nm.

High-resolution X-ray diffraction 2θ-ω-scans of the three- and six-pair GaN/AlGaN DBRs are shown in Figure 77. The distinguished interference fringes indicate smooth surfaces and interfaces of the GaN/AlGaN DBR structures. Additionally, an excellent agreement between experimental and simulated data, suggesting a perfect periodicity, was observed. Using the XRD simulation software, the Al content was deduced to be 16%, and the calculated thicknesses confirmed the expected ones. Consequently, the measured growth rates using in-situ reflectometry were reliable and allowed an accurate control of the different thicknesses.

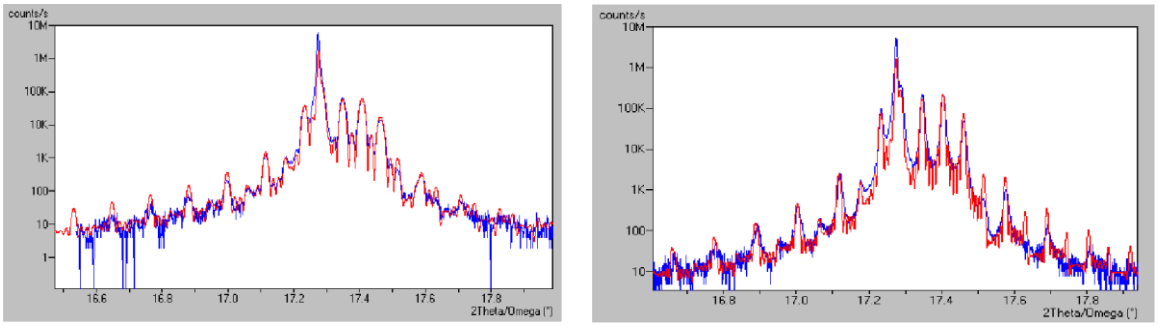

(a) (b)

Figure 77: XRD 2θ-ω scans for AlGaN/AlN DBRs (a) three periods and (b) six periods. Red and blue curves correspond to experimental and simulated data, respectively.

As observed by Normarski microscopy, the surface morphologies of all grown AlGaN/GaN DBR structures are crack free. AFM measurements show a typical 2D morphology with clear terraces. The measured RMS was approximately 0.6nm. Numerous V-pits with important density and size were also observed and are shown in Figure 78.

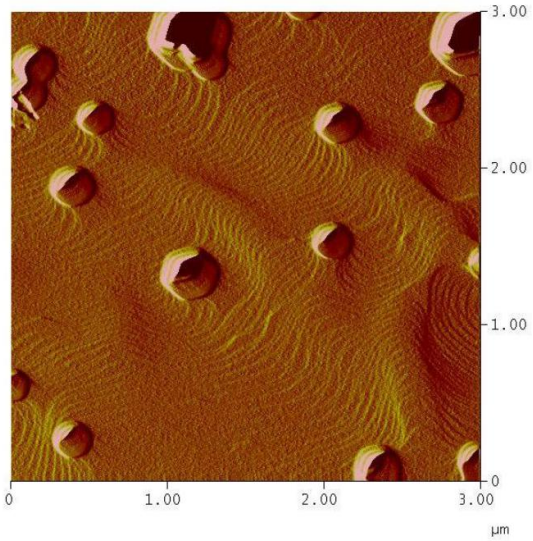

Figure 78: AFM image showing a good surface morphology of a six-pair $Al_{0.16}Ga_{0.84}N$/GaN DBR.

Furthermore, the surface morphologies of the three- and six-pair Bragg reflectors were investigated by SEM. The confirmation of 2D growth and the high size and density of V defects are depicted in Figure 79. The V-defects in the six-pair DBR are much larger than those in the three-pair structure. This difference confirms the difficulty of developing DBR structures with a high number of periods to achieve 90% reflectivity. Using this material system, more than 60 periods are needed to reach such reflectivity.

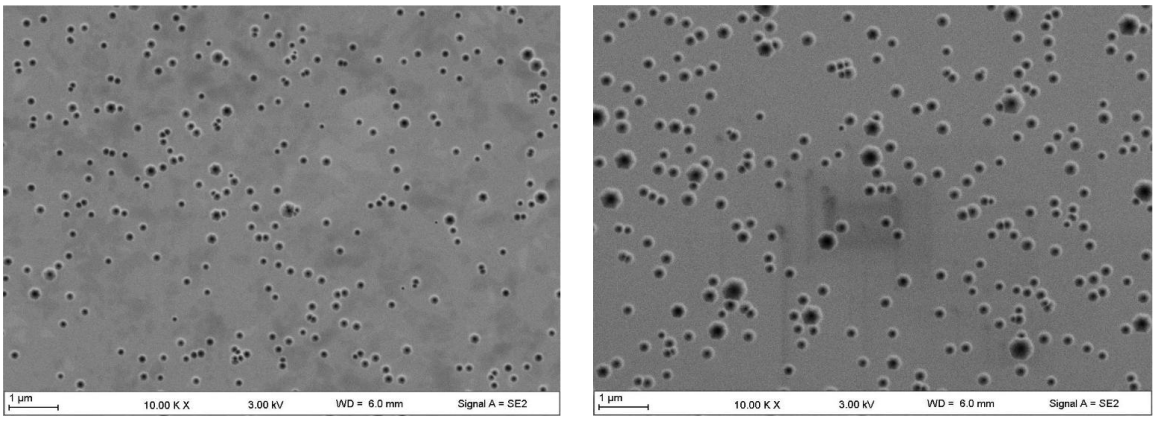

(a) (b)

Figure 79: SEM images showing different DBR surface morphologies of (a) three and (b) six periods.

The DBR reflectivities of the three- and six-pair DBR structures were measured afterward to validate the Reflector software simulations. The experimental reflectivities were measured using spectrophotometry tool, and the results are depicted in Figure 80. The blue and red curves present the experimental and simulated data, respectively.

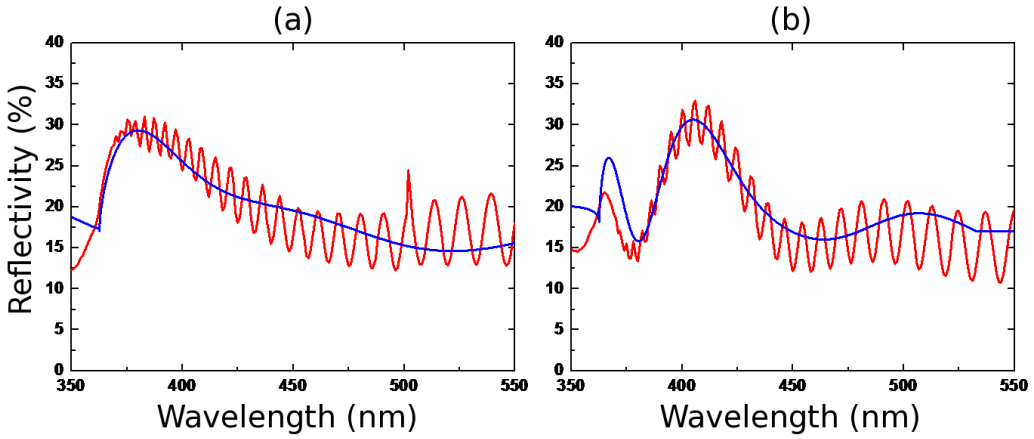

Figure 80: Experimental (red) and simulated (blue) reflectivity curves of (a) three and (b) six periods of AlGaN/GaN DBRs.

The comparison of the simulation data and measurements confirmed the reliability of the developed simulation software. Using the calculated values of the refractive indexes and the corresponding thicknesses, the simulated spectra fitted well the experimental curves. Nonetheless, remaining differences in the high-wavelength part of the spectra were noticed, as can be seen in Figure 80. This difference is mainly because of the interferences caused by the sapphire substrate and was not taken into account in the simulations. Consequently, the reflectivity calculation tool is reliable. Of course, the simulation is only valid if no parasitic effects, such as surface roughness, presence of cracks, or sharp interfaces, deteriorate the reflectivity.

Despite the achieved descent reflectivity in the three- and six-pair DBR structures, growing a large number of periods without cracks was challenging. This difficulty is explained by the limited critical thickness (Section 4.3.2). An additional limitation is the increase of V-defects size and density. When additional AlGaN/GaN DBR structures

with thick structures or high aluminum content have been grown, cracks were observed at the surface. Consequently, the achieved reflectivity was attenuated. Therefore, we have investigated different nitride materials that can be used in the DBR structures in the near-UV range.

5.1.2 BGaN/GaN DBRS

As seen previously, to compensate for the limited refractive index contrast between AlGaN materials, it is fundamental to use highly mismatched materials. However, this high lattice mismatch in conventional AlGaN materials (up to 2.4%) is detrimental to the crystalline quality of the grown layers. For instance, the formation of cracks largely affects the processing of the final device. Consequently, we propose to investigate new BGaN materials to develop highly reflective DBRs.

Taking advantage of the large refractive index contrast between GaN and BGaN and the small induced lattice mismatch, the BGaN/GaN DBRs have been studied as a possible alternative to AlGaN/GaN systems. The DBR structures were grown on a GaN template as a multi stack of six periods of approximately 40nm thick with alternating layers BGaN and GaN. The 420nm central wavelength was chosen to prevent any absorption occurring in the GaN and BGaN layers. In fact, because of the BGaN large bandgap-bowing parameter, the material bandgap energy can reach 380nm.

3D AFM images of the BGaN/GaN DBR surfaces, with 0.7% and 1.3% of boron content, respectively, are shown in Figure 81. The root mean square roughnesses of the surface are calculated to be approximately 21 and 19nm, respectively. This high surface RMS is explained by the 3D growth, which is caused by the BGaN films quality, as observed in Chapter 4. Crystal platelets in different orientations are also observed in the different BGaN-based DBR structures. This feature affects the total reflectivity.

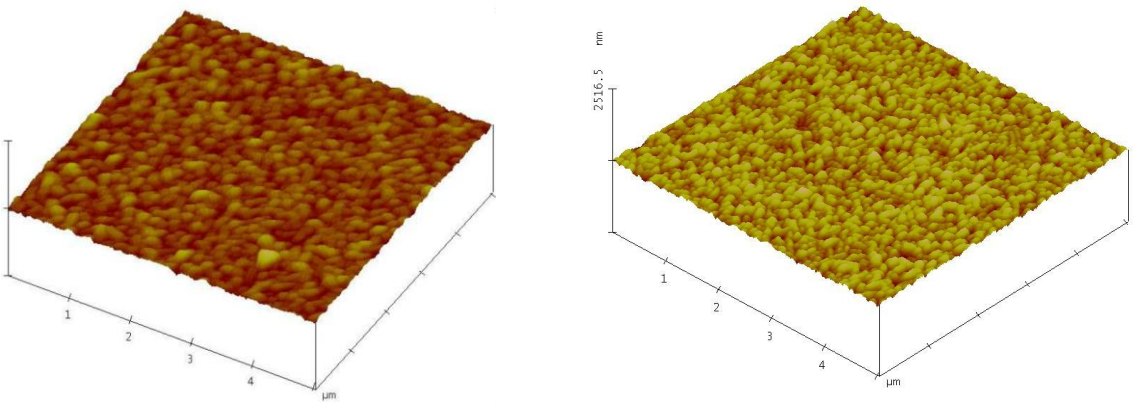

(a) (b)

Figure 81: 3D AFM image showing the surface morphology of BGaN/GaN DBR structures: (a) three and (b) six periods.

Despite this morphological issue, the presence of satellite peaks on the X-ray diffraction 2θ-ω scan of the six periods $B_{0.007}Ga_{0.993}N/GaN$ and $B_{0.013}Ga_{0.987}N/GaN$ DBRs indicates a descent structural quality. The X-ray diffraction scans are shown in Figure 82. The angular spacing between the peaks confirmed the structure periodicity, which is in good agreement with the growth parameters. The low-boron content DBR shows a better crystalline quality with more slightly distinguished fringes than the high-boron content one.

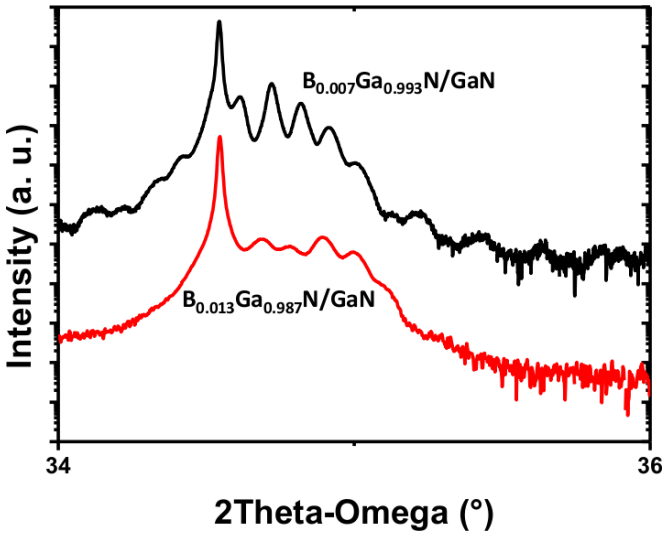

Figure 82: XRD 2θ-ω scans of the (00.2) peak for the six periods $B_{0.007}Ga_{0.993}N/GaN$ and $B_{0.013}Ga_{0.987}N/GaN$ DBR structures.

The experimental and simulated reflectivities of BGaN/GaN DBRs with 0.7 and 1.3% of boron content are shown in Figure 83. The simulated spectra were obtained using the measured BGaN dispersion model and the transfer matrix method [153]. To fit the different interference fringes, the sapphire substrate was taken into consideration in the simulations. Because of the large difference between the calculated and measured data, the alignment of the interferences was important.

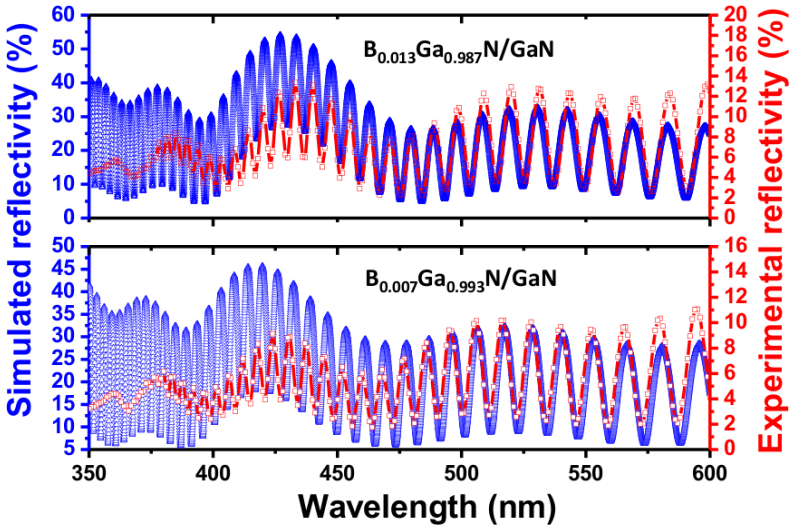

Figure 83: Experimental (red) and simulated (blue) reflectivity spectra of six periods $B_{0.013}Ga_{0.987}N$/GaN (top) and $B_{0.007}Ga_{0.993}N$/GaN (bottom) DBRs. The spectra wavelengths are centered around 420nm, as expected.

In comparison with the peak reflectivity of $B_{0.007}Ga_{0.993}N$/GaN, which is approximately equal to 7%, the peak reflectivity nearly doubled in the second structure. The reflectivity reached 13%. This increase of peak reflectivity at 420 nm is clearly impacted by the boron incorporation. A good agreement of the peak positions between the simulated and experimental curves has been also obtained. However, at the central wavelength, the experimental peak intensity is three to four times lower than the simulated one. This difference can be explained by the large surface roughness and the non-abrupt interfaces between BGaN and GaN.

To investigate the interface quality, the BGaN-based DBR structures have been analyzed using TEM. However, because of the low boron content in the BGaN layers, the

interfaces were not very clear. Consequently, the BGaN and GaN layers were almost undifferentiated. Therefore, a similar structure has been grown with adding seven 1nm-AlN interlayers in the BGaN films to act as markers. The DBR structure and its Z-contrast TEM image are summarized in Figure 84a and 84b, respectively. The dark layers are the AlN markers. When looking at the interfaces between GaN and BGaN, one can see some thickness modulation. This modulation explains the deviation between the measured and simulated reflectivities. Consequently, with the current growth conditions, the development of highly reflective structures would still be difficult. As a conclusion, BGaN has a big potential for DBR structures in the near-UV region. However, an improvement of the BGaN structural quality is paramount for the development of highly reflective BGaN based DBRs.

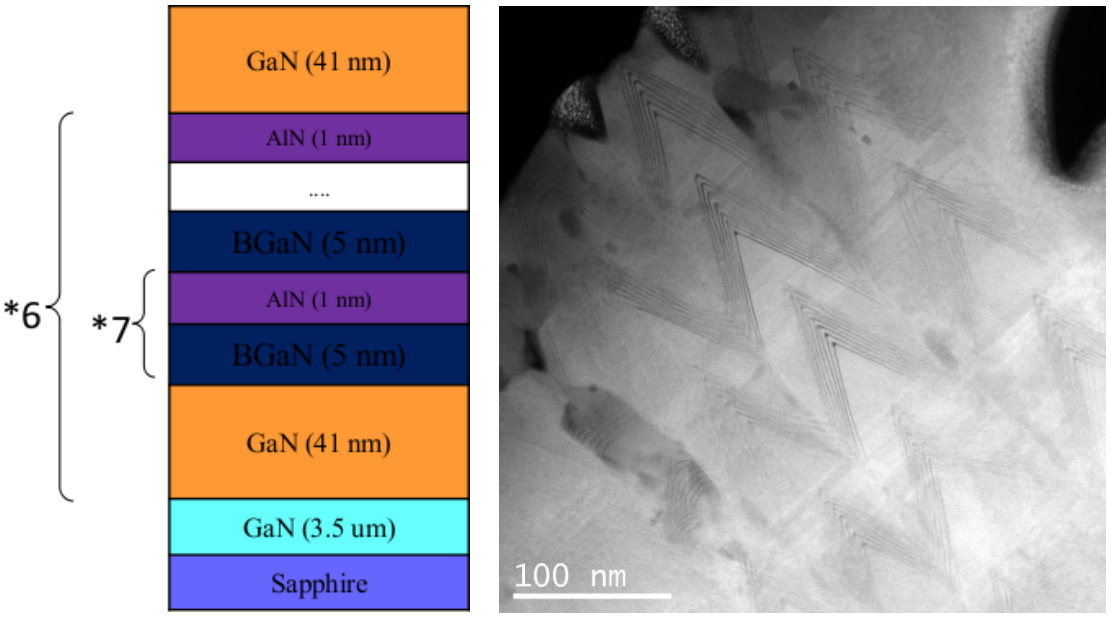

(a) (b)

Figure 84: (a) Schematic of a BGaN/GaN DBR with AlN interlayers. (b) TEM cross section of the DBR structure.

Despite the large difference between the measured and simulated reflectivities, the large increase in the peak reflectivity, induced by a small incorporation of boron, is promising. These results pave the way for BAlN-based DBRs.

5.2 Realization of Deep-UV distributed Bragg reflectors

The growth of AlGaN/GaN and BGaN/GaN DBRs in the near-UV range was summarized in the previous section. Because of the important absorption in GaN, the reported structures cannot be used for DBR applications below 350nm. Consequently, different material systems are investigated in this section to replace the GaN layers for the development of DBR structures in the deep-UV region.

Toward this study, several DBR structures formed by AlN, AlGaN, and BAlN layers were grown on standard AlN templates. Because of the AlN strong transparency, the AlN template is fundamental for deep-UV applications.

5.2.1 AlGaN/AlN DBRs

To date, the $Al_xGa_{1-x}N$ /AlN system is the most frequently studied candidate for deep-UV DBRs. As mentioned in the previous chapters, the DBR design must carefully balance competing trade-offs. Factors to take into account include a) the limited refractive index contrast that decreases with decreasing Ga content in the AlGaN layers, b) the transparency of the AlGaN layers diminishes with increasing Ga content, and c) the large in-plane lattice mismatch, which limits achievable film thickness. These competing requirements mean that highly reflective AlGaN/AlN DBRs need multilayer stacks with many periods and/or high Al content contrast. However, under such conditions, thick structures lead to a reduced stop-band and/or a large in-plane lattice mismatch. The large lattice mismatch degrades the device quality and limits its performance. Consequently, there have been relatively few reports studying DBR reflectivity below 320nm [16, 72], and the results were still not sufficient for VCSEL devices. In fact, the reflectivities did not exceed 95% and the stop-bandwidths were less than 13nm.

In this study, the DBR structure grown to achieve deep-UV region is a five-pair $Al_{0.8}Ga_{0.2}N$/AlN stack. However, to avoid the absorption issues that might occur below 300nm and also to compare this DBR to the previously reported AlGaN/GaN structures,

we aimed a central wavelength of 400nm. During the DBR runs, the AlGaN and GaN layers were deposited at 1000°C and at 100 torr pressure using N2 carrier gas. The AlN and AlGaN λ/4 layers are 47nm thick and 45nm thick, respectively. The total DBR thickness is 500 nm. The number of periods was limited to five to prevent the structure from any relaxation and crack which might affect the reflectivity.

The DBR stack was first analyzed by AFM to investigate the surface morphology, as shown in Figure 85. A very different surface morphology in comparison to the previously reported $Al_{0.16}Ga_{0.84}N$/GaN surfaces was observed. The V-defects completely disappeared in the current structure. However, the growth is 3D, and the surface roughness of 12.5nm is largely higher than previous values. This large roughness can be explained by the difficulty to grow high quality high-Aluminum content AlGaN. The large surface roughness prevents the development of DBR structures using this material system with high number of periods with the current growth conditions. In addition to the high surface roughness, cracks and large dislocation density appeared when growing thick structures. Consequently, investigating other growth conditions is fundamental to achieve high-quality AlGaN-based structures.

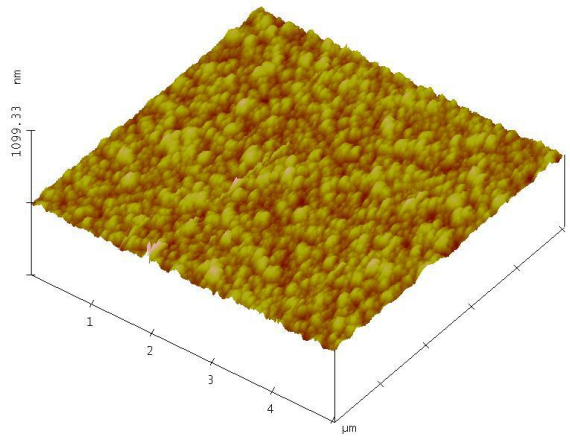

Figure 85: 3D AFM images showing the surface morphology of the five-pair $Al_{0.8}Ga_{0.2}N$/AlN reflector.

The DBR reflectivity was afterward measured over the range [250 - 550nm]. The DBR reflectivity is shown in Figure 86. The red curve presents the experimental data, and the blue one illustrates the simulation based on the Reflector software. Using the AlGaN refractive indexes and the expected thicknesses, the simulated spectra fitted quite well the measured spectra. Nonetheless, a small difference between the spectra can be observed. This is mainly explained by the high surface roughness, which was previously observed by AFM. Consequently, the total reflectivity was affected with 5% of losses. The attenuation becomes more important when thick structures with several periods are investigated.

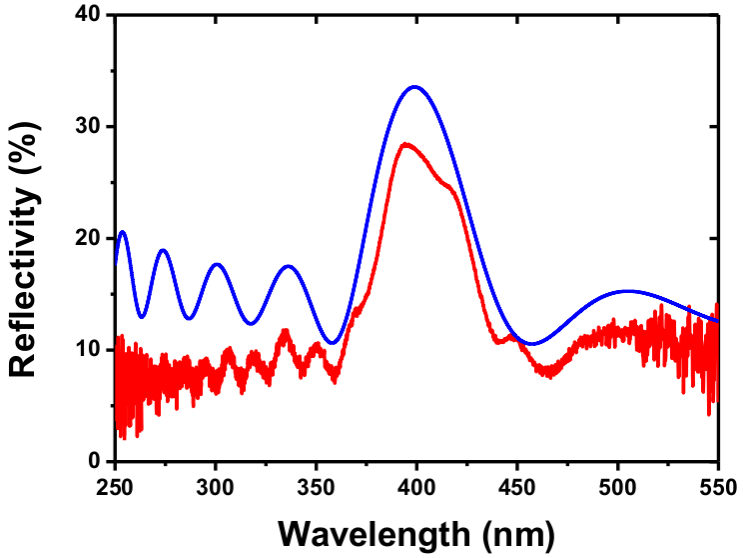

Figure 86: Experimental (red) and simulated (blue) reflectivity curves of a DBR with five periods of $Al_{0.8}Ga_{0.2}N$/AlN. The spectra are centered around 400nm.

Up to now, The AlGaN/AlN material system has been the only candidate to realize nitride mirrors in the deep-UV region. However, these nitride systems present several limitations. BAlN, which extends from 6.2 eV for AlN to 5.5 eV for BN, holds great potential for UV-based DBRs because of its large bandgap energy range. Additionally, BAlN alloys can be used for compensated DBR structures with a specific aluminum and boron concentration. Consequently, DBR structures with large number of periods can be grown without major strain issues. Hence, BAlN was introduced in next

sections to overcome these issues and therefore offer a promising alternative to standard AlGaN-based DBRs in the deep-UV range.

5.2.2 BAlN/AlN DBRs

By combining both BAlN UV transparency and the high refractive index contrast of BAlN with respect to AlN, a series of BAlN/AlN DBRs were grown on AlN template substrates. The BAlN/AlN DBR structures were designed with a target center wavelength located within 250-350nm. The DBR design was based on BAlN and AlN as the low/high refractive index layer and the BAlN/AlN thicknesses were designed to be quarter-wave layers. To compare the reflectivities and bandwidths, the number of stacks in the DBRs was changed from six to 24. The TEB/III ratio was varied from 0 to 71%. Careful examinations by Nomarski optical microscopy after the growth showed that all BAlN/AlN DBR structures were completely crack-free over the full sample area.

Toward this study, an 18-pair BAlN/AlN DBR with 25% boron content was selected to investigate its structural and morphological properties and the AlN/BAlN interfaces through TEM analysis. The total thickness is 1.2µm.

Similarly to the BAlN films, the XRD scans only exhibit the peak related to the AlN layers. Neither BAlN peak nor fringes were observed. This feature confirms that the BAlN structural quality is not good enough to expect a comparable XRD curve to AlGaN or BGaN-based DBR structures. The surface morphology was then analyzed by AFM (Figure 87a) and SEM (Figure 87b). The surface morphology exhibits a smoother surface in comparison to BGaN-based DBR structures with a surface roughness of 11nm, for a much thicker structure. AFM and SEM images reveal several grains along the surface with diameter size not exceeding 100nm. We noticed that the surface roughness doesn't increase when structures with large number of periods are grown. For instance, a 36-pair BAlN/AlN DBR exhibits a 12nm surface roughness.

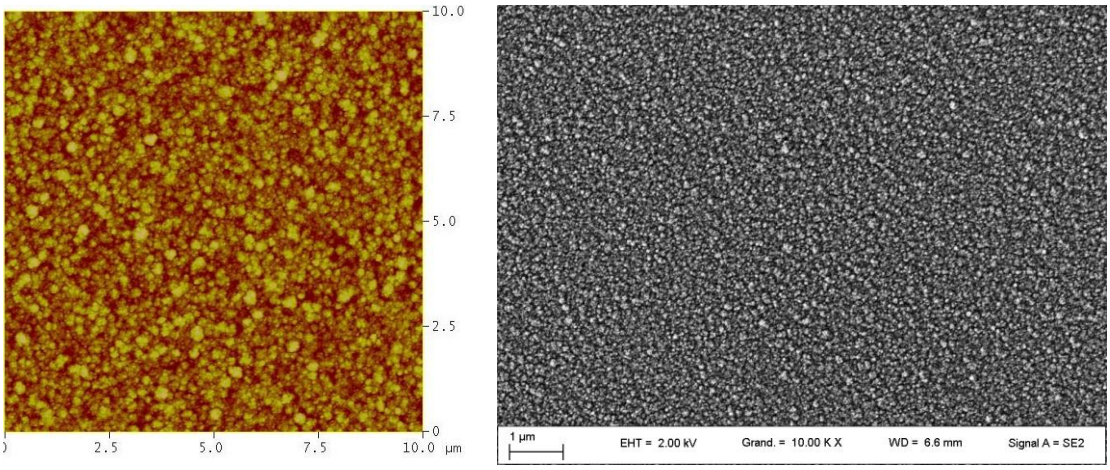

(a) (b)

Figure 87: (a) AFM and (b) SEM surface morphologies of the 18-pair BAlN/AlN DBR structure.

The experimental reflectivity of a BAlN/AlN DBR structure, shown in Figure 88, was measured by Fourier transform infrared spectroscopy over UV and visible ranges.

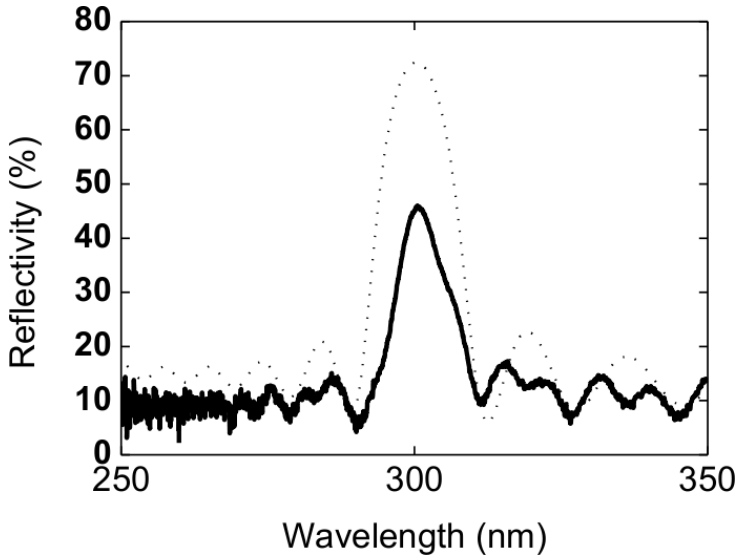

Figure 88: Experimental (solid) and simulated (dashed) reflectivity spectrum of a DBR with 18 periods of BAlN/AlN. The spectra are centered around 300nm.

A maximum reflectivity of 46% with 18 periods was obtained at 300 nm. The bandwidth is around 15nm. Despite the divergence of the experimental peak from the

70% theoretical peak value, a good agreement between the simulated and experimental curves for the peak positions has been obtained. Theoretically, more than 90% reflectivity can be reached with less than 20 periods by incorporating more boron and by improving the BAlN materials structural quality. The simulations were largely investigated in Chapter 3.

To understand the difference between the experimental and simulated reflectivities, the DBR samples were examined by transmission electron microscopy.

A Z-contrast TEM image of the 18-period DBR structure is shown in Figure 89. The bottom layer is the AlN template and the upper layers are the DBRs. One can see that the interface between bright (AlN) and dark (BAlN) layers is quite rough. This roughness is the main reason for the difference between the measured and theoretical peak reflectivities.

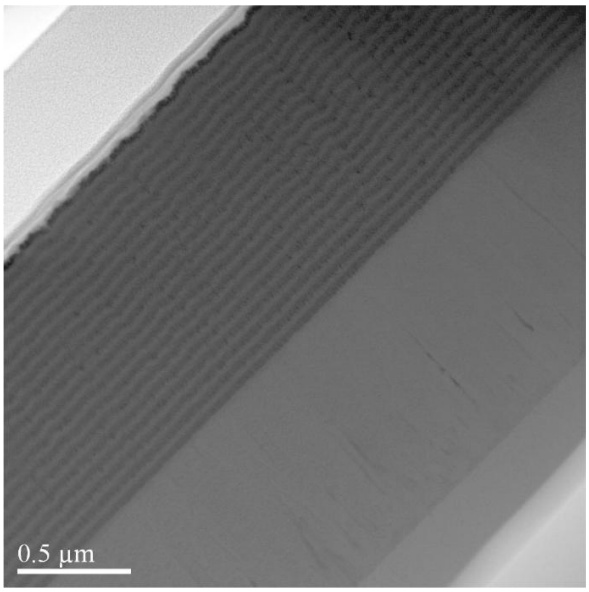

Figure 89: TEM cross section of an 18-pair 1.2µm thick BAlN/AlN stack grown on AlN template.

Additionally, EDX analysis in the DBR structures revealed the presence of boron in the AlN layers, suggesting a BAlN/BAlN DBR structure instead of the expected BAlN/AlN stack. The boron content was approximated to 10% using EDX technique.

This feature also explains the contrast difference in STEM-HAADF between the AlN layers in the DBR structure and the AlN template. This boron presence in AlN implies a reduction of the refractive index contrast. Consequently, the theoretical peak reflectivity decreases. Furthermore, the few nm surface roughness of the DBR structure leads to high optical scattering losses. The last feature can also explain the difference between the calculated and measured reflectivity spectra.

Next, to achieve highly reflective DBR with a minimum number of periods, a series of BAlN/AlN DBRs with high boron content were grown. The boron content reached 47% in the solid phase. A SIMS analysis has been performed in an 18-pair BAlN/AlN stack to evaluate the periodicity for this high-boron content structure.

The SIMS results are reported in Figure 90. One can observe a clear periodicity between the different layers with a good homogeneity of the boron content in the BAlN layers. The 18 periods were also very well defined. The TEM analysis, shown in Figure 89, confirms the good separation between the different layers.

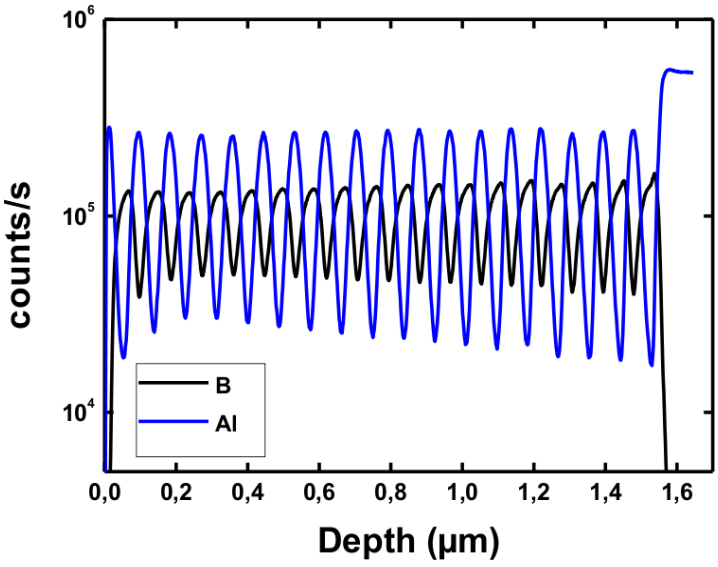

Figure 90: SIMS profile of a BAlN/AlN DBR structure grown on AlN template.

The experimental and calculated reflectivity spectra of 18- and 24-pair BAlN/AlN DBR structures are shown in Figure 91. The experimental reflectivities were measured by

FTIR. At 311nm, a reflectivity of 82% and a bandwidth of 20nm were obtained for only 18 periods. The 24-pair DBR, reaching a deep-UV wavelength of 282nm, exhibits a peak reflectivity of 60% and a bandwidth of 16nm. The results demonstrate the potential of BAlN-based stacks for short-wavelength devices. The large bandwidth of 20nm (215meV) results from the high refractive index contrast between the AlN and BAlN layers. The theoretical bandwidth is higher than the achieved value. The difference is explained by the presence of boron in the AlN layers. Consequently, the refractive index contrast and the bandwidth are reduced.

In spite of the achieved high reflectivities, the measured values are lower than the predicted ones (97 and 99%) using simulations based on the experimental refractive index values.

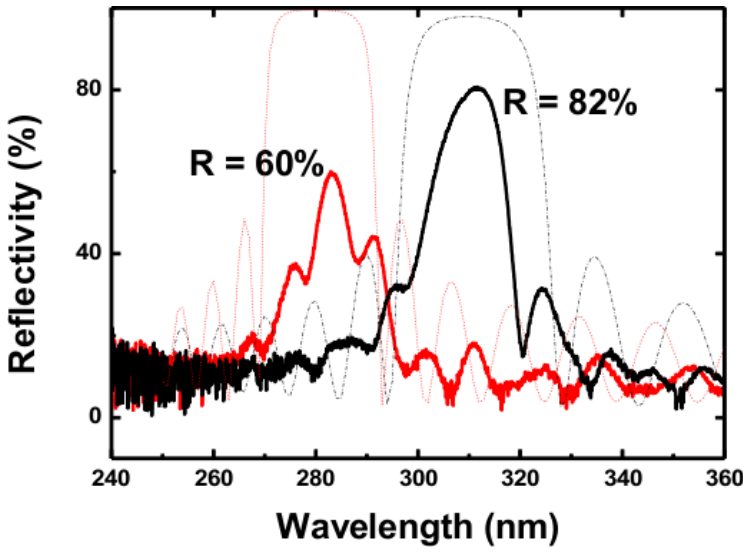

Figure 91: Experimental (solid lines) and simulated (dotted lines) reflectivity spectrum of 18/24-pair BAlN/AlN DBR. The spectra are centered at 311nm and 282nm, respectively.

A close comparison of the measured (solid lines) and the calculated (dotted lines) reflectivities shows that the stop-bandwidth is not reduced by the surface roughness in the BAlN-based DBRs. The difference is fully explained by the presence of boron in the AlN layers. However, the surface and interface roughness only affects the maximal amplitude of the central reflectivities.

It is clear that the surface roughness decreases the peak reflectivty as that was previously observed in AlGaN/AlN structures. However, the surface roughness doesn't explain the attenuation in the peak reflectivity at 280nm in comparison to the 310nm-centered DBR structure. This attenuation can be explained by a residual absorption because of the non-perfect BAlN material quality. Toward this goal, a transmission measurement of the BAlN layer used in this DBR stack was performed.

Theoretically, because of the transparency of the different materials, the spectrum analysis is no longer influenced by the absorption above 220nm (BAlN bandgap). Consequently, if the BAlN has a small number of defects, the transmittance spectrum exhibits a sharp decay close to the bandgap energy, and oscillations appears above 220nm. However, one crucial point worth noticing in Figure 92 is that the transmission curve exhibits a very progressive attenuation. The transmission completely vanishes at the BAlN bandgap. Consequently, the light is strongly absorbed in this wavelength range. This result is an indication of a very large residual absorption tail. Such high residual absorption would limit the DBR reflectivity below 90%. Consequently, the development of very highly reflective DBRs with the currently used growth conditions is very challenging.

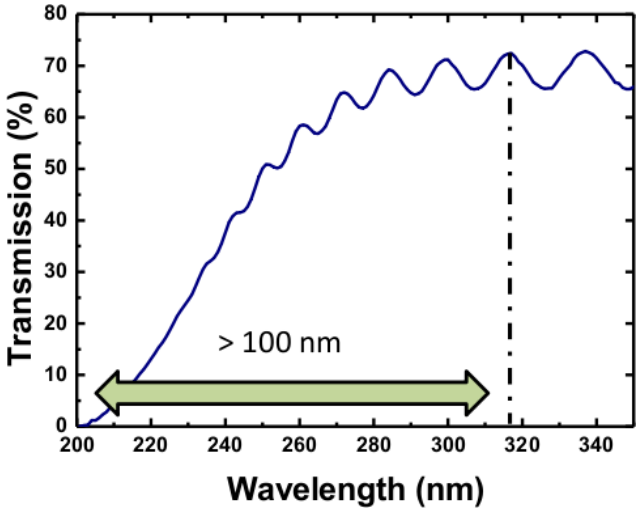

Figure 92: Transmission spectrum of a 150nm BAlN film.

Following the promising results achieved using BAlN/AlN system and the absence of XRD peak, the structural quality of the different DBR layers was studied using Raman spectroscopy.

Toward this study, an 18-pair BAlN/AlN DBR structure grown on GaN template has been investigated. The GaN substrate was chosen to prevent any interference with AlN layers. The surface Raman spectra in two different scattering configurations are shown in Figure 93. The allowed "phonon" modes and the selection rules in the parallel and crossed polarizations for an AlN substrate are illustrated in the inset figure. The Raman selection rules allow the E2 mode in both configurations at 656 cm^{-1}, while only A1(LO) mode is allowed in the parallel polarization at 887 cm^{-1}. We note that the analyzer and polarizer filters attenuate the intensity. The spectra take into consideration this attenuation and the intensities were corrected.

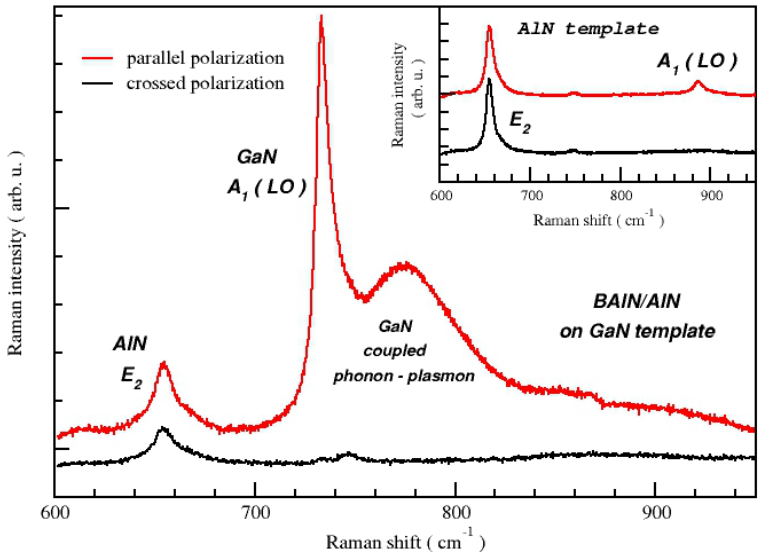

Figure 93: Raman spectra of the 18-pair BAlN/AlN DBR stack on GaN template substrate in the parallel and crossed polarizations.

A dominant peak at 734 cm^{-1} corresponding to the GaN substrate is exhibited in Figure 93. The mode A1(LO) is observed in the parallel polarization and respects the selection rules, as it vanishes in the other configuration. Additionally, the mode E2 of AlN is identified in both configurations at 656 cm^{-1}, suggesting a wurtzite structure of the

AlN layers (there is no equivalent mode in the cubic structures). However, the LO mode is not observed in either polarization. Moreover, no signature of the BAlN films was observed.

Then, to investigate this DBR structure, cross section analysis was performed. The obtained spectra are shown in Figure 94. The selection rules are shown in the inset figure. Similarly to the previous figure, the inset figure depicts the selection rules for a bulk AlN. The different modes of the GaN substrate were clearly observed: A1(TO) at 532 cm^{-1}, E2 at 567 cm^{-1}, and E1(TO) at 559 cm^{-1}. However, only the E2 mode of AlN was observed at 655 cm^{-1}. The absence of the different modes, which are theoretically allowed, suggests the formation of polycrystalline layers when BAlN films were added in the structure.

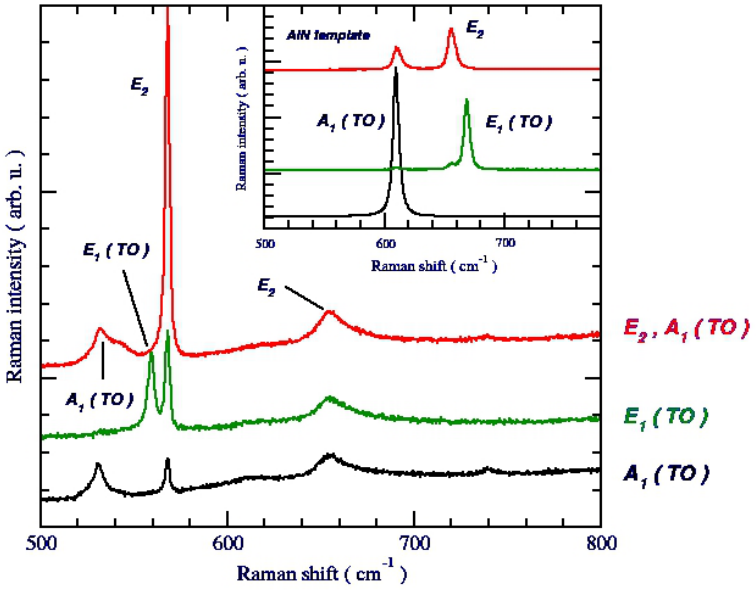

Figure 94: Cross section Raman spectra of the BAlN/AlN DBR structure. A comparison of the modes E2, A1(TO), E1(TO), and A1(T0) is shown in the inset figure.

The observed polycrystallinity was then confirmed by electron diffraction pattern, as shown in Figure 95. In fact, the diffraction pattern produced by the electron beam passing through the film is equivalent to that produced by a beam passing through several single crystals with different orientations. This phenomenon explains the revealed series

of concentric rings, suggesting that the BAlN film is polycrystalline with no preferred orientation.

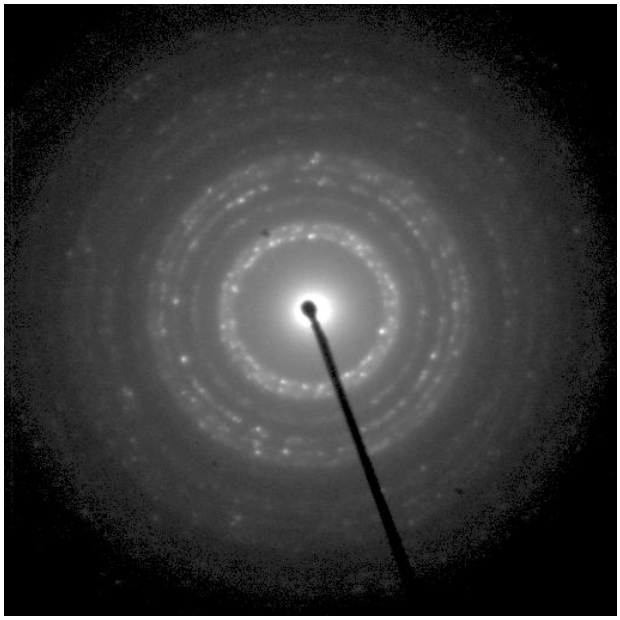

Figure 95: Selected area electron diffraction pattern of a BAlN layer.

As the ultimate goal is to use this structure as a bottom DBR stack in the VCSEL device, the grown layers over BAlN-based DBRs have been investigated. As a preliminary analysis, a 150nm GaN film has been grown on a 4-pair BAlN/AlN DBR structure on AlN template. The sample was then analyzed through photoluminescence and X-ray diffraction. The obtained results are reported in Figure 96.

The PL spectrum exhibits near band edge emission at 363nm. This peak corresponds to the optical bandgap of the GaN film. Therefore, the growth of an active region over the BAlN-based DBR structures is possible. Additionally, this feature was confirmed by the presence of a diffraction peak related to the GaN film. However, the XRD peak is very weak and broad, which means it is fundamental to improve the structural quality of the single BAlN layers. As a consequence of this optimization, the DBR reflectivities and the structural quality of the grown films over the BAlN-based reflectors can be improved.

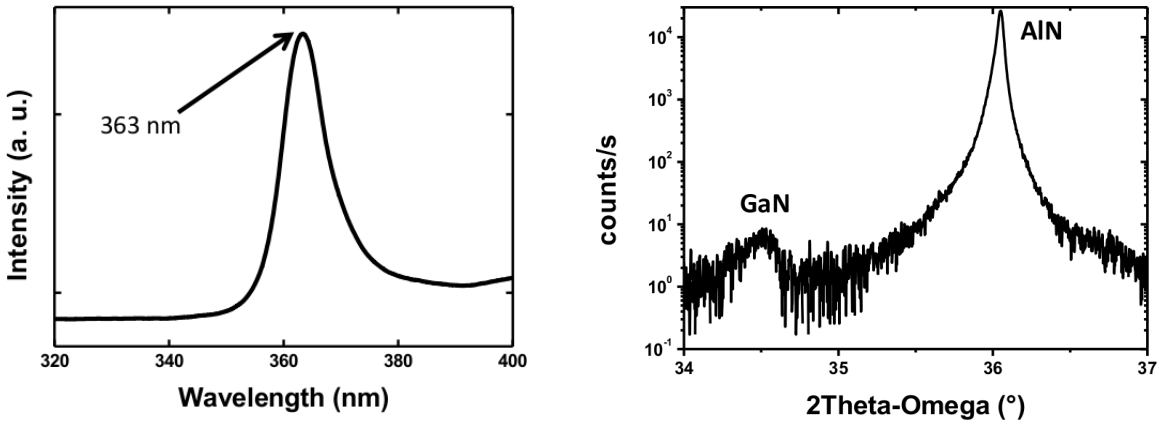

(a) (b)

Figure 96: (a) PL spectrum and (b) XRD 2θ-ω scan of GaN film grown on BAlN/AlN DBR structure on AlN template.

5.2.3 BAlN/AlGaN DBRs

Following the promising results that have been previously demonstrated using BAlN/AlN system, BAlN/AlGaN DBR structures have been developed. Using this material system, the system takes advantage of two important features: (a) the refractive index contrast is larger than BAlN/AlN (Figure 97a) and (b) the possibility to design compensated structures (Figure 97b). In fact, the AlN refractive index and lattice parameter are lower than AlGaN parameters, but larger than BAlN ones. These features enable the development of strain-free structures with refractive index exceeding 0.5 at 300nm.

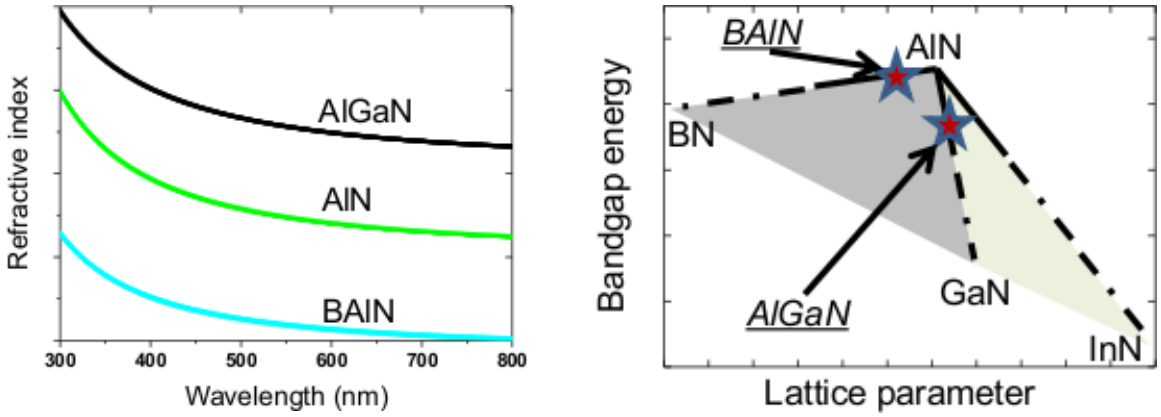

(a) (b)

Figure 97: The two major advantages of the BAlN/AlGaN system for DBR applications: (a) large refractive index contrast and (b) strain compensation.

To confirm this tendency, the BAlN/AlGaN DBRs were investigated. This work is a continuity of the simulation presented in Figure 41. Several BAlN/AlGaN Bragg reflectors with different number of periods were grown. The AlGaN and BAlN layers are deposited with the same growth conditions than the previously studied nitride materials. The BAlN/AlGaN DBR was first compared to the previously reported systems: BAlN/AlN and AlGaN/AlN. Toward this goal, five-pair reflectors were grown with three different configurations with the same boron and aluminum content.

Next, the BAlN/AlGaN was analyzed by X-ray diffraction to study the structural quality of the different layers. The XRD 2θ-ω scan of the five-pair BAlN/AlGaN DBR grown on AlN template is reported in Figure 98. In addition to the AlN peak, an additional XRD peak related to the AlGaN layer was observed. However, the XRD peak is quite broad, suggesting that the structural quality of the AlGaN layers is deteriorated by the BAlN films. The aluminum content was calculated to be 80%. This aluminum content was chosen to prevent any absorption coming from the AlGaN films when using this material system below 300nm.

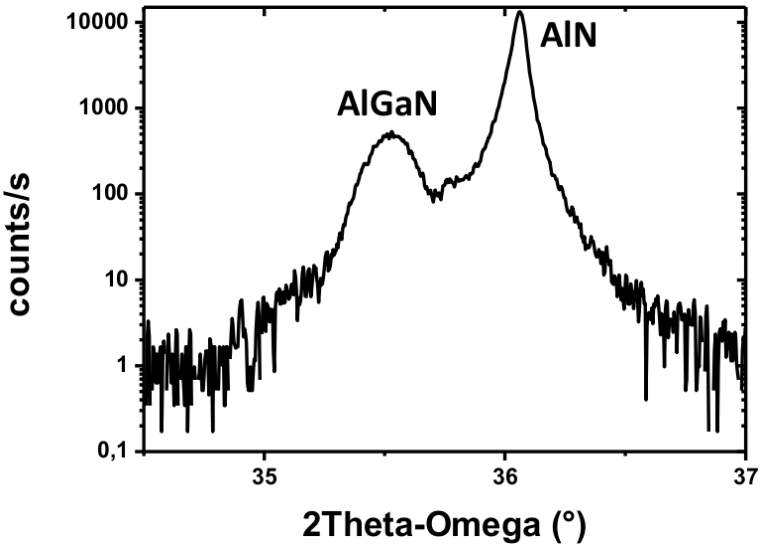

Figure 98: XRD 2θ-ω scan of a five-pair BAlN/AlGaN DBR on AlN template.

A comparison between three DBR systems is reported in Figure 99. The systems are: (a) AlGaN/AlN, (b) BAlN/AlN, and (c) BAlN/AlGaN. All the AlGaN and BAlN layers have the same aluminum and boron content. The first $Al_{0.8}Ga_{0.2}N$/AlN five-pair reflector exhibits a 28% reflectivity. Replacing the AlGaN layers by BAlN layers results in a small increase of the peak reflectivity by approximately 2%. As the material systems have similar refractive indexes, the reflectivity increase is not significant. The difference becomes more significant if DBR structures are grown with more than five pairs. In comparison to the previous systems, the BAlN/AlGaN structure exhibits a 37% peak reflectivity with only five periods. This high-reflectivity value, combined to the large bandgap of BAlN and AlGaN alloys, confirm the potential of the BAlN/AlGaN DBR system to achieve highly reflective DBR structure in the deep-UV range.

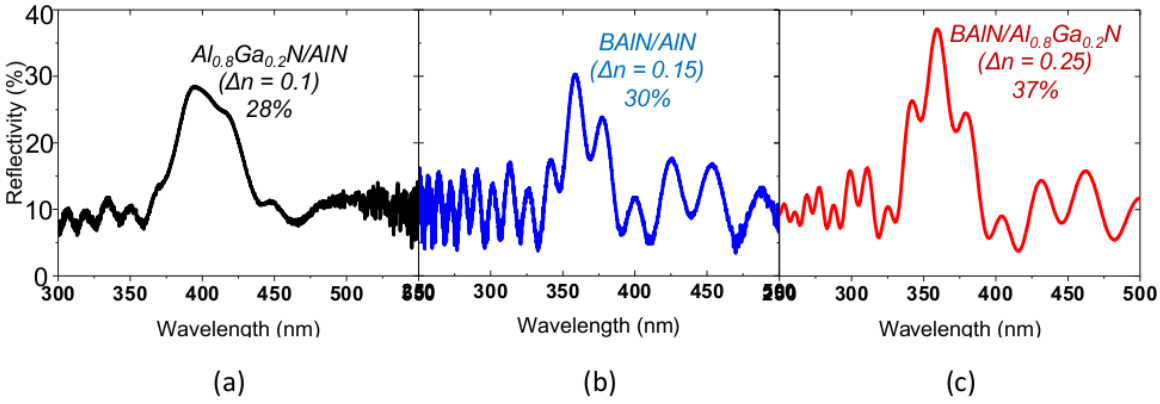

Figure 99: Experimental reflectivity spectrum of five-pair DBR: (a) AlGaN/AlN, (b) BAlN/AlN, and (c) BAlN/AlGaN.

In all reported structures, the experimental peak reflectivity was lower than that expected from the experimental refractive index contrast. This is mainly explained by the relatively large surface roughness already observed in the AFM images and the rough interface between the different layers forming the DBR, as illustrated by TEM analysis. An optimization of the BAlN material will automatically reduce the difference between the experimental and simulated reflectivities. This attenuation can be overcome if DBRs are grown with large number of periods or rich-boron BAlN films. Toward this goal, an

18 pair BAlN/AlGaN DBR has been grown in the near-UV range to avoid any kind of residual absorption. The aluminum content was calculated to be 70%. The experimental reflectivity is given in Figure 100. The reflector exhibits a 93% reflectivity with only 18 periods. The bandwidth is as high as 40 nm. Despite the regular difference between experience and simulation experienced in all BAlN-based structures, the achieved peak reflectivity is very high. In fact, very few papers gave evidence of reflectivity higher than 90% with less than 20 periods.

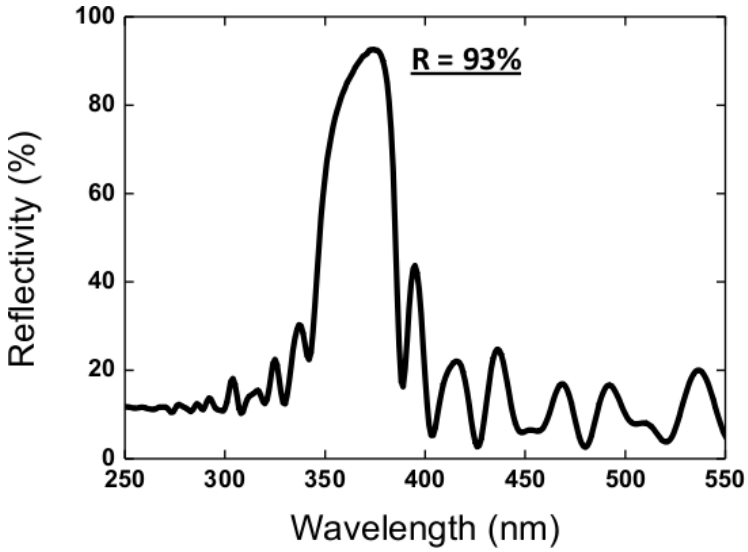

Figure 100: Experimental reflectivity spectrum of a BAlN/AlGaN DBR with 18 periods.

One of the main concerns for boron-based Bragg reflectors is the possible residual light absorption in the deep-UV wavelength range (shown previously in Figure 92). The BAlN/AlGaN DBR will suffer from the reported extremely extended band edge in the sub-bandgap absorption spectra of BAlN samples. This would lead to a strong decrease in the performance of the Bragg reflector, especially when moving to short wavelengths (below 300nm). To overcome this absorption issue, two options will be proposed. The first option is to compensate the losses by growing more periods in the structure. The second option is to investigate BAlN films with different growth conditions; noticeably with H_2 as carrier gas and a growth temperature higher than 1000°C.

In summary, three different possible configurations of the DBR were studied by comparing the theoretical and experimental maximum reflectivities. It was demonstrated that AlGaN/BAlN is undoubtedly the most suitable system for deep-UV applications. The potential of this material system confirms the possible use of BAlN in the bottom DBR structures of next generation boron-based VCSELs in the UV range. Furthermore, these structures can enable the growth of monolithic structures, which will reduce the cost of production of VCSELs.

CHAPTER 6

CONCLUSIONS AND FUTURE DIRECTIONS

6.1 Conclusion

In the past few decades, owing to its compactness, circular beam profile, and small size, VCSEL has progressively emerged as an efficient source of coherent light alongside the conventional edge-emitting laser. The development of the short-wavelength (λ<400nm) VCSEL has been fueled by the need for low-cost devices and the requirement of UV sources for several potential applications. The applications include bioagent detection, printing, and super-high-density optical storage systems. However, the practical realization of these lasers has proved to be challenging because of the numerous technological difficulties, such as achieving good optical confinement and highly reflective semiconductor DBRs. This manuscript described the achieved results during this Ph.D. work to overcome some of the issues listed above.

This work was dedicated to the analysis of the (B,Al,Ga)N semiconductor materials growth and characterization to promote their use in MQW and DBR structures for the development of innovative VCSEL devices emitting in the UV range.

In the first part of this study, we have demonstrated the high refractive index contrast of the dilute BGaN and BAlN ternaries with respect to AlN and GaN, respectively. Indeed, a large refractive index contrast was observed with boron inclusion reaching 0.27 in BAlN/AlN system at 300nm. Consequently, innovative DBRs based on BAlN/AlN structures with high reflectivity can be theoretically achieved at wavelengths as low as 240nm. Then, a structural and morphological analysis was performed on the different nitride layers revealing noticeably a relatively high surface roughness.

After a study of the different nitride materials, the DBR reflectivities were simulated using the experimental data. In fact, the parameters deduced form the

ellipsometry measurements were used in the modeling of the Bragg mirrors. The simulations confirmed the potential of the boron-based materials to achieve highly reflective DBRs in the UV range. Two software were also designed to investigate noticeably the strain-free structures.

Then, AlGaN/AlN MQWs were investigated as a potential candidate of the VCSEL active medium. Clear interstitial fringes were visible in the 2θ-ω scans, indicating a good interface quality between AlGaN wells and AlN barriers in the MQWs. Additionally, photoluminescence peaks were observed around 280nm.

The last part of this study is dedicated to the boron-based DBR stacks. BGaN/GaN, BAlN/AlN, and BAlN/AlGaN DBRs have been grown and characterized, for the first time. These boron-based DBRs present an alternative to conventional AlGaN-based structures. Despite the relatively high surface roughness and the rough interfaces revealed by AFM and TEM, these boron-based DBR structures exhibited promising results in the near-UV and UV spectral ranges. For instance, 93% reflectivity was achieved at 370nm with only 18 periods using BAlN/AlGaN system.

6.2 Recommendations for future research

In the preliminary research, we have essentially focused on the optical properties of diluted B(Al,Ga)N materials and their potential application in the distributed Bragg reflectors in the UV region.

The future research will cover a deep investigation of the BAlN materials through the optimization of the MOVPE growth conditions. This optimization will be followed by the application of those boron-based materials for highly reflective DBRs in the deep-UV region.

BAlN growth conditions optimization: For research and development of novel semiconductor DBRs that simultaneously achieve high reflectivity, high structural quality, and a minimum absorption in the deep-UV region, it is fundamental to further

optimize the growth conditions of BAlN materials. MOVPE growth parameters, such as the total pressure in the reactor and the V/III ratio will be optimized to improve the BAlN structural quality and the interface abruptness in the DBR structures. One additional key parameter to obtain high quality boron-based material is to use high growth temperature around 1300°. H_2 will noticeably be used as carrier gas toward the optimization of the BAlN materials and the reduction of its absorption in the deep-UV region.

Realization of highly reflective DBRs based on BAlN: As stated in the previous sections, we have successfully grown and characterized AlGaN/GaN, BGaN/GaN, and BAlN/AlN DBRs. The next step is to reach at least 98% reflectivity with a central wavelength below 300nm.

Up to now, the highest reflectivity was achieved using BAlN/AlGaN reaching 93% with only 18 periods. Different solutions to obtain highly reflective DBRs have to be explored. The first approach will concern the improvement of the existing structures by growing similar stacks with more periods. However, it is important to consider the optical output of the VCSEL, which will be attenuated if there are too many periods. Consequently, we propose to use other approaches, such as growing DBR structures with more boron content, enabling larger refractive index contrast.

Realization of the final VCSEL structure: After performing the optimization of the BAlN materials and the BAlN-based DBR structures, the objective will be to demonstrate VCSEL laser emission. Toward this goal, promising designs of the nitride VCSEL structures for operation at 280nm are schematically depicted in Figure 101. They contain the major building blocks presented in the previous chapters: the BAlN/AlGaN bottom DBR, a dielectric top DBR, and an InAlGaN-based active region. The first structure (Figure 101a) is an optically-pumped surface-emitting laser. The optical pumping allows to asses the quality of the epitaxial and amorphous dielectric materials, without the need of complex processing technology. The second one (Figure 101b) is an electrically-

pumped device using a lateral carrier injection. The ultimate objective is to go beyond the resonant-cavity LED (RCLED) mode of operation to achieve laser emission.

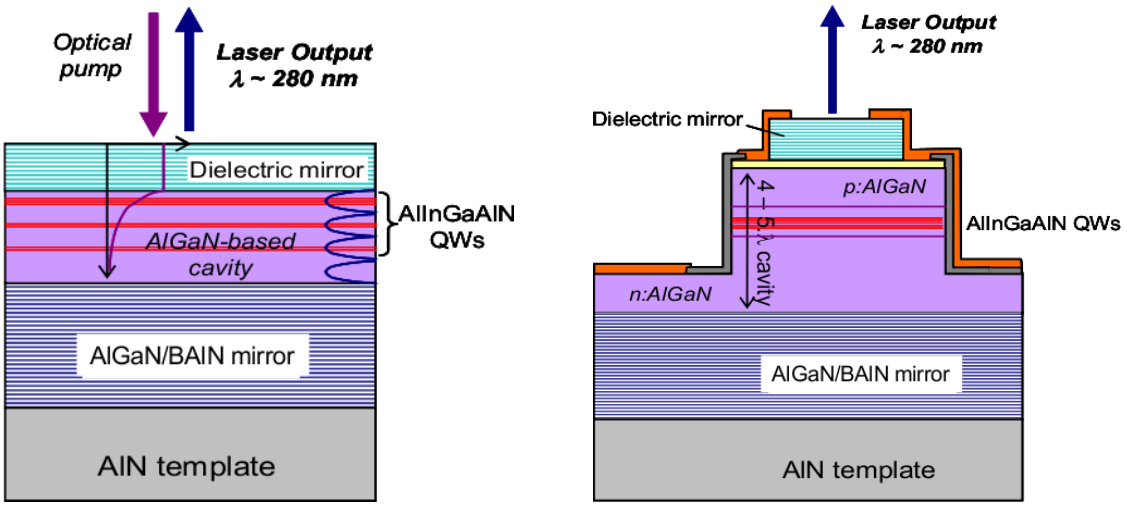

Figure 101: (a) Optically-pumped UV-VCSEL grown on AlN substrate or pseudo-substrate. The structures include an AlGaN/BAlN bottom mirror, a cavity with strained InAlGaN QWs, and a top dielectrically mirror. (b) Electrically-pumped device with two intracavity contacts consisting of transparent conductive oxides.

6.3 The road to UV nitride VCSELs

As presented in the previous chapters, the development of the nitride UV VCSEL is suffering from several challenges. The challenges include the optical quality of the active medium, the poor conductivity of the p-type AlGaN for electrical injection, and mainly the development of highly reflective DBRs with large bandwidth. The introduction of the boron-based materials provides an adequate solution to overcome the different issues preventing the development of highly reflective reflectors in the UV range. One additional consequence of these structures is the possible realization of monolithic devices as a replacement of the costly hybrid structures.

For the electrical injection devices, intra-cavity contacts were reported to propose an efficient carrier injection without passing through the mirrors [34] (Figure 101b). In fact, in this configuration, the electrons and holes are injected in the active medium above the n-side and below the p-side DBRs. Additionally, as the conventional dielectric

mirrors structures are insulating, this intracavity contact solution would also overcome this issue. However, the low conductivity of the p-type AlGaN films remains problematic. In this diagonal injection configuration, several ideas were reported. In fact, increasing the lateral hole conductivity by a factor of 30 was demonstrated using modulation doped nitride superlattices [154, 155]. This is caused by the apparition of high mobility 2D hole gases at each interface [34]. Linked to the previous issue, it is fundamental to overcome the challenge related to the p-type doping of high-Al content $Al_xGa_{1-x}N$ materials with high conductivity.

To date, sapphire is the most common substrate [18, 38, 39]. The efficiency of nitride UV lasers grown on sapphire substrates is very sensitive to the presence of cracks and dislocation density resulting from the high lattice mismatch between the nitride layers. Although special care have been undertaken to reduce dislocations and other defects densities in the substrate and the grown layers, it is fundamental to develop bulk AlN substrates. In fact, to reach UV VCSEL, AlN substrates are required to take advantage of AlN large bandgap and its suitability for high-aluminum AlGaN growth [156]. However, AlN substrates are not yet readily accessible because of the commercially limited availability and high price. Consequently, an intensive effort is currently performed to master this technology and therefore enable their use in commercial devices.

Based on the achieved results in this study, an ANR Blanc entitled "VESUVE" has been accepted in 2011. The ultimate goal of this ANR project is to develop a VCSEL device operating in the UV spectral range based on boron DBRs.

6.4 Publications based on this research work

- C. Alhenc-Gelas, P. Heroin, J. Jacquet, M. Abid, S. Gautier, and A. Ougazzaden, "Design rules of high reflectivity Bragg AlGaN mirrors for 300 nm VCSELs," SPIE, 7229, 72290N (2009).

- T. Moudakir, S. Gautier, G. Orsal, N. Maloufi, D. J. Rogers, F. H. Teherani, F. Jomard, M. Abid, N. Fressengeas, and A. Ougazzaden, "MOVPE growth of InGaN on ZnO-buffered Si(111) substrates for solar cells applications," Proc. EW-MOVPE XIII (2009).
- A. Ougazzaden, D. J. Rogers, F. H. Teherani, G. Orsal, T. Moudakir, S. Gautier, V. E. Sandana, F. Jomard, M. Abid, M. Molinari, M. Troyon, P. L. Voss, D. McGrouther, and J. N. Chapman, "Epitaxial MOVPE growth of highly c-axis oriented InGaN/GaN films on ZnO-buffered Si (111) substrates," Proc. SPIE, 7603, 76031D-1 - 76031D-8 (2010).
- S. Gautier, G. Orsal, T. Moudakir, N. Maloufi, F. Jomard, M. Alnot, Z. Djebbour, M. Abid, P. L. Voss, and A. Ougazzaden, "Metal-organic vapor phase epitaxy of BInGaN quaternary alloys and characterization of boron content," J. Cryst. Growth, 312, 641-644 (2010).
- T. Moudakir, M. Abid, B. T. Doan, E. Demarly, S. Gautier, G. Orsal, J. Jacquet, A. Ougazzaden, and F. Genty, "Asymmetrical design for non-relaxed near-UV AlGaN/GaN distributed Bragg reflectors," Proc. SPIE Photonics Asia, 7847, 78470B (2010).
- M. Abid, T. Moudakir, Z. Djebbour, G. Orsal, A. En Naciri, A. Migan-Dubois, and A. Ougazzaden, "Blue-Violet boron-based Distributed Bragg Reflectors for VCSELs application," J. Cryst. Growth, 315 1, 283-287 (2010).
- S.Gautier, G. Patriarche, T. Moudakir, M. Abid, G. Orsal, K. Pantzas, D. Troadec, A. Soltani, L. Largeau, O. Mauguin, and A. Ougazzaden, "Deep structural analysis of novel BGaN material layers grown by MOVPE," J. Cryst. Growth, 315 1, 288-291 (2010).
- W.H. Goh, G. Patriarche, P.L. Bonanno, S. Gautier, T. Moudakir, M. Abid, G. Orsal, A. A. Sirenko, Z.-H. Cai, A. Marthinez, A. Ramdane, L. Le Gratiet, D. Troadec, A. Soltani, and A. Ougazzaden, "Structural and optical properties of

nanodots, nanowires, and multi-quantum wells of III-nitride grown by MOVPE nano-selective area growth," J. Cryst. Growth, 315 1, Pages 160-163 (2010).

- S. Gautier, M. Abid, T. Moudakir, G. Orsal, A. En Naciri, K. Pantzas, F. Jomard, P. L. Voss, and A. Ougazzaden, "Application of dilute boron B(Al,In,Ga)N alloys for UV light sources," Proc. SPIE, 7940, 79400X, (2011).
- M. Abid, T. Moudakir, G. Orsal, S. Gautier, A. En Naciri, Z. Djebbour, J.-H. Ryou, G. Patriarche, L. Largeau, H. J. Kim, Z. Lochner, K. Pantzas, D. Alamarguy, F. Jomard, R. D. Dupuis, J.-P. Salvestrini, P. L. Voss, and A. Ougazzaden, "Distributed Bragg reflectors based on diluted boron-based BAlN alloys for deep ultraviolet optoelectronic applications," Appl. Phys. Lett., 100, 051101, (2012).

APPENDIX A

POLARIZATION IN THE III-N MATERIALS

In III-nitride materials, polarization is present as a direct consequence of their non centrosymmetric wurtzite structure, the large ionicity of the covalent metal-nitrogen bonds, and the large lattice mismatch when dealing with heterostructures. The origin and effect of the III-N system polarization will be briefly explained.

Because of the large difference in lattice parameters in III-N strained heterostructures, the layers are either under tensile or compressive strain. Therefore, III-N alloys exhibit a strong piezoelectric effect which can be formulated by Equation 48.

$$P_{PE} = 2\frac{a - a_0}{a_0}(e_{31} - e_{33}\frac{c_{13}}{c_{33}}), \tag{48}$$

whereas a_0 and a are the relaxed and real lattice constants, C are elastic stiffness constant related to Young's modulus and Poisson's ratio, and e are piezoelectric constants [157, 158]. Table 9 summarizes the main structural parameters of the nitride alloys.

Table 9: Polarization and elastic parameters of wurtzite BN, AlN, and GaN [3].

Parameters	GaN	AlN	BN
C_{11} (GPa)	347	390	957
C_{12} (GPa)	139	133	137
C_{13} (GPa)	104	112	74
C_{33} (GPa)	376	383	1077
e_{13} (C/m^2)	-0.32	-0.38	0.27
e_{33} (GPa)	0.63	1.29	-0.85

The piezoelectric polarization occurs when stress is applied to the group III-nitride lattice, changing the lattice parameters a and c of the relaxed structure to accommodate the stress. This polarization is added to the spontaneous polarization, which occurs in the equilibrium lattice of the group III-N systems at zero strain. In fact, In 1997, the first value of spontaneous polarization were reported by F. Bernardini et al. [159] while demonstrating that electric fields arising in AlN/GaN Superlattices is not only piezoelectric. In fact, the electric field was explained by the spontaneous polarization in nitride materials. Since then, several studies have been published on the polarization effect and origin in III-N alloys.

As explained in Chapter 4, group III-N atoms are surrounded with nitrogen atoms by their intense ionicity-covalent bonds. The structure can be simplified by a model assuming that the nitrogen planes carry a negative charge and the III elements planes carry positive charge, as shown in Figure 102. Consequently, an electrical dipole is formed along the c-axis, and the coulomb interaction between atoms lead to the appearance of a strong macroscopic spontaneous polarization. It is very important to consider the orientation of the nitride growth as the group III-N will have two different faces, as shown in Figure 102. They are referred to N-face and group III (Ga, Al, In, B)-face when the III element is on the top position of the {0001} bilayer, corresponding to the [0001] polarity. The N-face is defined by a polarization vector pointing from the anion (N) to the nearest cation (III element) along the longitudinal bond, as depicted with a red upward vector along the c-axis. Spontaneous polarization in ternary or quaternary coumpounds can be calculated by interpolating the binary systems corrected with a bowing "b" parameter.

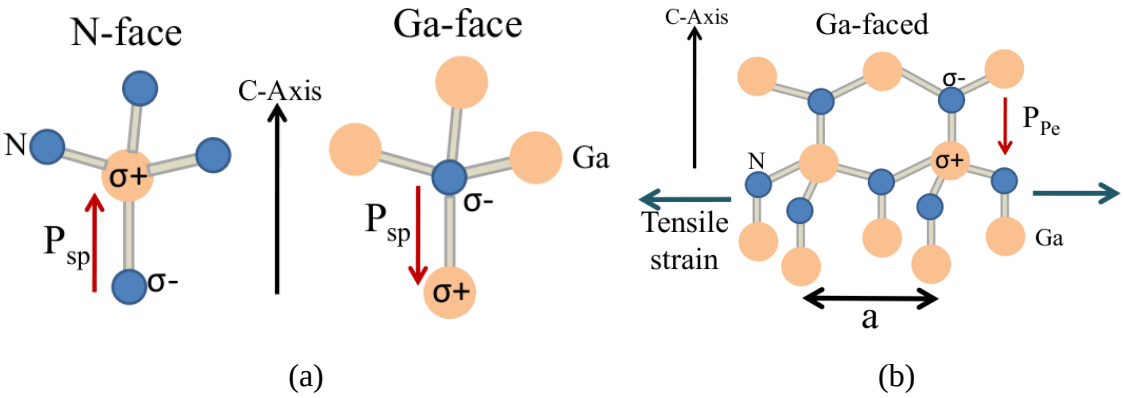

Figure 102: (a) Spontaneous polarization and (b) piezoelectric polarization caused by tensile stress.

When considering nitride heterostructures, both polarizations sum up, giving the total polarization $P_{tot} = P_{PE} + P_{Sp}$. As an important consequence of the total polarization, the electrical and optical characteristics of III-N materials can be influenced because the polarization leads to the band structure bending. Consequently, the net polarization and consequent internal electric fields have been shown to be detrimental to the performance of optoelectronic devices. For instance, the built-in electric field induced from the strained QW results in a quantum confined stark effect (QCSE), leading to a decreased recombination efficiency. Nevertheless, the net polarization can be also used constructively in solar cells and HEMT devices to improve their performances. Therefore, the understanding of spontaneous and piezoelectric polarizations in III-N binaries and their related alloys is fundamental and has reached in the last years a new plateau. However, further research is still needed to confirm the proposed values, noticeably related to boron-based materials as they are only calculated theoretically.

REFERENCES

[1] http://www.ioffe.rssi.ru.

[2] http://en.wikipedia.org.

[3] K. Shimada, T. Sota, and K. Suzuki, "First-principles study on electronic and elastic properties of BN, AlN, and GaN," JOURNAL OF APPLIED PHYSICS, vol. 84, pp. 4951-4958, NOV 1 1998.

[4] J. Li, K. Nam, M. Nakarmi, J. Lin, H. Jiang, P. Carrier, and S. Wei, "Band structure and fundamental optical transitions in wurtzite AlN," APPLIED PHYSICS LETTERS, vol. 83, pp. 5163-5165, DEC 22 2003.

[5] D. Brunner, H. Angerer, E. Bustarret, F. Freudenberg, R. Hopler, R. Dimitrov, O. Ambacher, and M. Stutzmann, "Optical constants of epitaxial AlGaN films and their temperature dependence," JOURNAL OF APPLIED PHYSICS, vol. 82, pp. 5090-5096, NOV 15 1997.

[6] J. Piprek, T. Peng, G. Qui, and J. Olowolafe, "Energy gap bowing and refractive index spectrum of AlInN and AlGaInN," in 1997 IEEE INTERNATIONAL SYMPOSIUM ON COMPOUND SEMICONDUCTORS (Melloch, M and Reed, MA, ed.), (345 E 47TH ST, NEW YORK, NY 10017 USA), pp. 227-230, IEEE; Motorola; USN, Off Naval Res; Siemens; Aixtron; EPI, IEEE, 1998. 24th IEEE International Symposium on Compound Semiconductors, SAN DIEGO, CA, SEP 08-11, 1997.

[7] S.Watanabe, T. Takano, K. Jinen, J. Yamamoto, and H. Kawanishi, "Refractive indices of bxal1-xn (x = 0-0.012) and byga1-yn (y = 0-0.023) epitaxial layers in ultraviolet region," PHYSICA STATUS SOLIDI (c), vol. 0, pp. 2691-2694, 2003.

[8] www.azom.com/.

[9] S. Murtaza, K. Anselm, A. Srinivasan, B. Streetman, J. Campbell, J. Bean, and L. Peticolas, "High-Reflectivity Bragg Mirrors For Optoelectronic Applications," IEEE JOURNAL OF QUANTUM ELECTRONICS, vol. 31, pp. 1819-1825, OCT 1995.

[10] S. Einfeldt, V. Kirchner, H. Heinke, M. Diesselberg, S. Figge, K. Vogeler, and D. Hommel, "Strain relaxation in AlGaN under tensile plane stress," JOURNAL OF APPLIED PHYSICS, vol. 88, pp. 7029-7036, DEC 15 2000.

[11] S. Hearne, J. Han, S. Lee, J. Floro, D. Follstaedt, E. Chason, and I. Tsong, "Brittle-ductile relaxation kinetics of strained AlGaN/GaN heterostructures," APPLIED PHYSICS LETTERS, vol. 76, pp. 1534-1536, MAR 20 2000.

[12] J. Bethoux, P. Vennegues, F. Natali, E. Feltin, O. Tottereau, G. Nataf, P. De Mierry, and F. Semond, "Growth of high quality crack-free AlGaN films on GaN templates using plastic relaxation through buried cracks," JOURNAL OF APPLIED PHYSICS, vol. 94, pp. 6499-6507, NOV 15 2003.

[13] H. Soda, K. Iga, C. Kitahara, and Y. Suematsu, "GaInAsP-InP surface emitting injection-lasers," JAPANESE JOURNAL OF APPLIED PHYSICS, vol. 18, no. 12, pp. 2329-2330, 1979.

[14] http://www.optowell.com/.

[15] K. Iga, "Vertical-cavity surface-emitting laser: Its conception and evolution," JAPANESE JOURNAL OF APPLIED PHYSICS, vol. 47, pp. 1-10, JAN 2008.

[16] C. Moe, Y. Wu, J. Piprek, S. Keller, J. Speck, S. DenBaars, and D. Emerson, "AlGaN/AlN distributed Bragg reflectors for deep ultraviolet wavelengths," PHYSICA STATUS SOLIDI A-APPLICATIONS AND MATERIALS SCIENCE, vol. 203, pp. 1915-1919, JUN 2006.

[17] http://www.azooptics.com/Details.asp?newsID=2849.

[18] H. Yoshida, Y. Yamashita, M. Kuwabara, and H. Kan, "Demonstration of an ultraviolet 336 nm AlGaN multiple-quantum-well laser diode," APPLIED PHYSICS LETTERS, vol. 93, DEC 15 2008.

[19] http://www.scienceblog.com/community/older/2003/D/20032215.html.

[20] C. DeCusatis, Handbook of Fiber Optic Data Communication. ACADEMIC PRESS, 2002.

[21] J. Wu, W. Walukiewicz, K. Yu, J. Ager, E. Haller, H. Lu, and W. Schaff, "Small band gap bowing in In1-xGaxN alloys," APPLIED PHYSICS LETTERS, vol. 80, pp. 4741-4743, JUN 24 2002.

[22] J. W. Lee, C. Sone, Y. Park, S. N. Lee, J. H. Ryou, R. D. Dupuis, C. H. Hong, and H. Kim, "High effciency GaN-based light-emitting diodes fabricated on dielectric-mask-embedded structures (vol 95, 011108, 2009)," APPLIED PHYSICS LETTERS, vol. 95, SEP 28 2009.

[23] K. Watanabe, T. Taniguchi, and H. Kanda, "Direct-bandgap properties and evidence for ultraviolet lasing of hexagonal boron nitride single crystal," NATURE MATERIALS, vol. 3, pp. 404-409, JUN 2004.

[24] M. Haase, J. Qiu, J. Depuydt, and H. Cheng, "Blue-Green Laser diodes," APPLIED PHYSICS LETTERS, vol. 59, pp. 1272-1274, SEP 9 1991.

[25] S. Nakamura, Introduction to Nitride Semiconductor Blue Lasers and Light Emitting Diodes. CRC Press, 2000.

[26] D. Yoo, Growth and Characterization Of III-Nitrides Materials System For Photonic And Electronic Devices By Metalorganic Chemical Vapor Deposition. PhD thesis, Georgia Institute of Technology, 2007.

[27] A. Denton and N. Ashcroft, "Vegard law," PHYSICAL REVIEW A, vol. 43, pp. 3161-3164, MAR 15 1991.

[28] P. Saengkaew, Epitaxial growth and properties of AlGaN-based UV-LEDs on Si(111) substrates. PhD thesis, genehmigt durch die Fakultät für Naturwissenschaften der Otto-von-Guericke-Universität Magdeburg, 2010.

[29] C. Wetzel, T. Takeuchi, S. Yamaguchi, H. Katoh, H. Amano, and I. Akasaki, "Optical band gap in Ga1-xInxN (O < x < 0.2) on GaN by photoreflection spectroscopy," APPLIED PHYSICS LETTERS, vol. 73, pp. 1994-1996, OCT 1998.

[30] S. Lee, A.Wright, M. Crawford, G. Petersen, J. Han, and R. Biefeld, "The bandgap bowing of AlxGa1-xN alloys," APPLIED PHYSICS LETTERS, vol. 74, pp. 3344-3346, MAY 31 1999.

[31] I. Vurgaftman, J. Meyer, and L. Ram-Mohan, "Band parameters for III-V compound semiconductors and their alloys," JOURNAL OF APPLIED PHYSICS, vol. 89, pp. 5815-5875, JUN 1 2001.

[32] S. Azzi, A. Zaoui, and M. Ferhat, "On the importance of the band gap bowing in Boron-based III-V ternary alloys," SOLID STATE COMMUNICATIONS, vol. 144, pp. 245-248, NOV 2007.

[33] A. Ougazzaden, S. Gautier, T. Moudakir, Z. Djebbour, Z. Lochner, S. Choi, H. J. Kim, J. H. Ryou, R. D. Dupuis, and A. A. Sirenko, "Bandgap bowing in BGaN thin □lms," APPLIED PHYSICS LETTERS, vol. 93, AUG 25 2008.

[34] J. Dorsaz, Lattice-matched AlInN Alloys For Nitride-Based Optoelectronic Devices. PhD thesis, Ecole Polytechnique Fédérale de Lausanne, 2006.

[35] J. Matthews and A. Blakeslee, "Defects In Epitaxial Multilayers Misfit Dislocations," JOURNAL OF CRYSTAL GROWTH, vol. 27, no. DEC, pp. 118-125, 1974.

[36] C. Kittel, Quantum Theory of Solids. 1987.

[37] http://www.cartage.org.lb/en/themes/sciences/physics/optics/LaserTutorial/Abso

[38] M. Kneissl, D. Treat, M. Teepe, N. Miyashita, and N. Johnson, "Ultraviolet InAlGaN multiple-quantum-well laser diodes," PHYSICA STATUS SOLIDI A APPLIED RESEARCH, vol. 200, pp. 118-121, NOV 2003.

[39] K. Iida, T. Kawashima, A. Miyazaki, H. Kasugai, S. Mishima, A. Honshio, Y. Miyake, M. Iwaya, S. Kamiyama, H. Amano, and I. Akasaki, "Laser diode of 350.9 nm wavelength grown on sapphire substrate by MOVPE," JOURNAL OF CRYSTAL GROWTH, vol. 272, pp. 270-273, DEC 10 2004.

[40] K. Iida, T. Kawashima, A. Miyazaki, H. Kasugai, S. Mishima, A. Honshio, Y. Miyake, M. Iwaya, S. Kamiyama, H. Amano, and I. Akasaki, "350.9 nm UV laser diode grown on low-dislocation-density AlGaN," JAPANESE JOURNAL OF APPLIED PHYSICS PART 2-LETTERS & EXPRESS LETTERS, vol. 43, pp. L499-L500, APR 1 2004.

[41] T. Margalith, Development of Growth and Fabrication Technology for Gallium Nitride-Based Vertical Cavity Surface Emitting Lasers. PhD thesis, University of California, 2002.

[42] C. Wilmsen, H. Temkin, and L. Coldren, Vertical-Cavity Surface-Emitting Lasers; design, Fabrication, characterization and applications. Cambridge University Press, 1999.

[43] M. Linnik and A. Christou, "Design and performance of a vertical cavity surface emitting laser based on III-V quaternary semiconductor alloys for operation at 1.55 mu m," IEEE TRANSACTIONS ON ELECTRON DEVICES, vol. 48, pp. 2228-2237, OCT 2001.

[44] H. T. C. Wilmsen and L. A. Coldren, Vertical-cavity surface-emitting lasers design, fabrication, characterization and applications. Cambridge University Press, 2001.

[45] S. F. Yu, Analysis and Design of Vertical Cavity Surface Emitting Lasers. Wiley-Interscience, 2003.

[46] Z. M. Lochner, Green Light Emitting Diodes And Laser Diodes Grown by Metalorganic Chemical Vapor Deposition. PhD thesis, Georgia Institute of Technology, 2010.

[47] S. Nakamura and G. Fasol, The Blue Laser Diode. 1997.

[48] J. Ding, H. Jeon, A. Nurmikko, H. Luo, N. Samarth, and J. Furdyna, "Laser action in the blue-green from optically pumped (Zn,Cd)Se/ZnSe) single quantumwell structures," APPLIED PHYSICS LETTERS, vol. 57, pp. 2756-2758, DEC 24 1990.

[49] B. G. Ed, Group III Nitride Semiconductor Compounds. Oxford University Press, 1998.

[50] F. McIntosh, K. Boutros, J. Roberts, S. Bedair, E. Piner, and N. ElMasry, "Growth and characterization of AlInGaN quaternary alloys," APPLIED PHYSICS LETTERS, vol. 68, pp. 40-42, JAN 1 1996.

[51] M. Shatalov, J. Zhang, A. Chitnis, V. Adivarahan, J. Yang, G. Simin, and M. Khan, "Deep ultraviolet light-emitting diodes using quaternary AlInGaN multiple quantum

wells," IEEE JOURNAL OF SELECTED TOPICS IN QUANTUM ELECTRONICS, vol. 8, pp. 302-309, MAR-APR 2002.

[52] I. Akasaki, H. Amano, S. Sota, H. Sakai, T. Tanaka, and M. Koike, "Stimulated emission by current injection from an AlGaN/GaN/GaInN quantum-well device," JAPANESE JOURNAL OF APPLIED PHYSICS PART 2-LETTERS, vol. 34, pp. 1517-1519, NOV 15 1995.

[53] S. Masui, Y. Matsuyama, T. Yanamoto, T. Kozaki, S. Nagahama, and T. Mukai, "365 mn ultraviolet laser diodes composed of quaternary AlInGaN alloy," JAPANESE JOURNAL OF APPLIED PHYSICS PART 2-LETTERS, vol. 42, pp. L1318-L1320, NOV 1 2003.

[54] M. A. Miller, M. H. Crawford, A. A. Allerman, K. C. Cross, M. A. Banas, R. J. Shul, J. Stevens, and K. H. A. Bogart, "Smooth and Vertical Facet Formation for AlGaN-Based Deep-UV Laser Diodes," JOURNAL OF ELECTRONIC MATERIALS, vol. 38, pp. 533-537, APR 2009.

[55] http://astrobiology.nasa.gov/astid/projects/.

[56] K. Iga, "Surface-emitting laser - its birth and generation of new optoelectronics field," IEEE JOURNAL OF SELECTED TOPICS IN QUANTUM ELECTRONICS, vol. 6, pp. 1201-1215, 2000.

[57] E. Towe, R. Leheny, and A. Yang, "A historical perspective of the development of the vertical-cavity surface-emitting laser," IEEE JOURNAL OF SELECTED TOPICS IN QUANTUM ELECTRONICS, vol. 6, pp. 1458-1464, NOV-DEC 2000.

[58] J. Harris, "Tunable long-wavelength vertical-cavity lasers: The engine of next generation optical networks?," IEEE JOURNAL OF SELECTED TOPICS IN QUANTUM ELECTRONICS, vol. 6, pp. 1145-1160, NOV-DEC 2000.

[59] C. Kao, Y. Peng, H. Yao, J. Tsai, Y. Chang, J. Chu, H. Huang, T. Kao, T. Lu, H. Kuo, S. Wang, and C. Lin, "Fabrication and performance of blue GaN-based vertical-cavity surface emitting laser employing AlN/GaN and Ta2O5/SiO2 distributed Bragg reflector," APPLIED PHYSICS LETTERS, vol. 87, AUG 22 2005.

[60] J.-Y. Zhang, L.-E. Cai, B.-P. Zhang, S.-Q. Li, F. Lin, J.-Z. Shang, D.-X. Wang, K.-C. Lin, J.-Z. Yu, and Q.-M. Wang, "Low threshold lasing of GaN-based vertical

cavity surface emitting lasers with an asymmetric coupled quantum well active region," APPLIED PHYSICS LETTERS, vol. 93, NOV 10 2008.

[61] T.-C. Lu, J.-R. Chen, S.-W. Chen, H.-C. Kuo, C.-C. Kuo, C.-C. Lee, and S.-C. Wang, "Development of GaN-Based Vertical-Cavity Surface-Emitting Lasers," IEEE JOURNAL OF SELECTED TOPICS IN QUANTUM ELECTRONICS, vol. 15, pp. 850-860, MAY-JUN 2009.

[62] T. Someya, R. Werner, A. Forchel, M. Catalano, R. Cingolani, and Y. Arakawa, "Room temperature lasing at blue wavelengths in gallium nitride microcavities," SCIENCE, vol. 285, pp. 1905-1906, SEP 17 1999.

[63] T.-C. Lu, C.-C. Kao, H.-C. Kuo, G.-S. Huang, and S.-C. Wang, "CW lasing of current injection blue GaN-based vertical cavity surface emitting laser," APPLIED PHYSICS LETTERS, vol. 92, APR 7 2008.

[64] Y. Higuchi, K. Omae, H. Matsumura, and T. Mukai, "Room-Temperature CW Lasing of a GaN-Based Vertical-Cavity Surface-Emitting Laser by Current Injection," APPLIED PHYSICS EXPRESS, vol. 1, DEC 2008.

[65] H. Ng, T. Moustakas, and S. Chu, "High reflectivity and broad bandwidth AlN/GaN distributed Bragg re ectors grown by molecular-beam epitaxy," APPLIED PHYSICS LETTERS, vol. 76, pp. 2818-2820, MAY 15 2000.

[66] M. Khan, J. Kuznia, J. Vanhove, and D. Olson, "Reflective filters based on single-crystal GaN/AlxGa1-xN multilayers deposited using low-pressure metalorganic chemical vapor-deposition," APPLIED PHYSICS LETTERS, vol. 59, pp. 1449-1451, SEP 16 1991.

[67] K. Waldrip, J. Han, J. Figiel, H. Zhou, E. Makarona, and A. Nurmikko, "Stress engineering during metalorganic chemical vapor deposition of AlGaN/GaN distributed Bragg reflectors," APPLIED PHYSICS LETTERS, vol. 78, pp. 3205-3207, MAY 21 2001.

[68] T. Someya and Y. Arakawa, "Highly reflective GaN/Al0.34Ga0.66N quarterwave reflectors grown by metal organic chemical vapor deposition," APPLIED PHYSICS LETTERS, vol. 73, pp. 3653-3655, DEC 21 1998.

[69] A. Bhattacharyya, S. Iyer, E. Iliopoulos, A. Sampath, J. Cabalu, T. Moustakas, and I. Friel, "High reflectivity and crack-free AlGaN/AlN ultraviolet distributed Bragg

reflectors," JOURNAL OF VACUUM SCIENCE & TECHNOLOGY B, vol. 20, pp. 1229-1233, MAY-JUN 2002.

[70] O. Mitrofanov, S. Schmult, M. Manfra, T. Siegrist, N. Weimann, A. Sergent, and R. Molnar, "High-reflectivity ultraviolet AlGaN/AlGaN distributed Bragg reflectors," APPLIED PHYSICS LETTERS, vol. 88, APR 24 2006.

[71] E. Feltin, J. Carlin, J. Dorsaz, G. Christmann, R. Butte, M. Laugt, M. Ilegems, and N. Grandjean, "Crack-free highly reflective AlInN/AlGaN bragg mirrors for UV applications," APPLIED PHYSICS LETTERS, vol. 88, JAN 30 2006.

[72] J. Xiao-Li, J. Ruo-Lian, X. Zi-Li, L. Bin, Z. Jian-Jun, L. Liang, H. Ping, Z. Rong, ZhengYou-Dou, and G. Hai-Mei, "High-reflectivity AlGaN/AlN distributed Bragg reflector in ultraviolet region," CHINESE PHYSICS LETTERS, vol. 24, pp. 1735-1737, JUN 2007.

[73] H. Ng, D. Doppalapudi, E. Iliopoulos, and T. Moustakas, "Distributed Bragg reflectors based on AlN/GaN multilayers," APPLIED PHYSICS LETTERS, vol. 74, pp. 1036-1038, FEB 15 1999.

[74] H. Yao, C. Lin, H. Kuo, and S. Wang, "MOCVD growth of AlN/GaN DBR structures under various ambient conditions," JOURNAL OF CRYSTAL GROWTH, vol. 262, pp. 151-156, FEB 15 2004.

[75] T. Zhu, A. Dussaigne, G. Christmann, C. Pinquier, E. Feltin, D. Martin, R. Butte, and N. Grandjean, "Nonpolar GaN-based microcavity using AlN/GaN distributed bragg reflector," APPLIED PHYSICS LETTERS, vol. 92, FEB 11 2008.

[76] T. Wang, R. Lynch, P. Parbrook, R. Butte, A. Alyamani, D. Sanvitto, D. Whittaker, and M. Skolnick, "High-reflectivity AlxGa1-xN/AlyGa1-yN distributed Bragg reflectors with peak wavelength around 350 nm," APPLIED PHYSICS LETTERS, vol. 85, pp. 43-45, JUL 5 2004.

[77] C. Simbrunner, M. Wegscheider, M. Quast, T. Li, A. Navarro-Quezada, H. Sitter, A. Bonanni, and R. Jakiela, "On the effect of periodic Mg distribution in GaN :delta-Mg," APPLIED PHYSICS LETTERS, vol. 90, APR 2 2007.

[78] J. Carlin and M. Ilegems, "High-quality AlInN for high index contrast Bragg mirrors lattice matched to GaN," APPLIED PHYSICS LETTERS, vol. 83, pp. 668-670, JUL 28 2003.

[79] J. Carlin, J. Dorsaz, E. Feltin, R. Butte, N. Grandjean, M. Ilegems, and M. Laugt, "Crack-free fully epitaxial nitride microcavity using highly reflective AllnN/GaN Bragg mirrors," APPLIED PHYSICS LETTERS, vol. 86, JAN 17 2005.

[80] X. Ni, R. Shimada, T. D. Kang, J. H. Leach, and U. Oezguer, "GaN-based vertical cavities with crack-free high-reflectivity patterned AlGaN/GaN distributed Bragg reflectors," PHYSICA STATUS SOLIDI A-APPLICATIONS AND MATERIALS SCIENCE, vol. 206, pp. 367-370, FEB 2009.

[81] E. Tiede, M. Thimann, and K. Sensse, "Phosphorescence-capable, by silicon activated aluminium nitride.," BERICHTE DER DEUTSCHEN CHEMISCHEN GESELLSCHAFT, vol. 61, no. Part 2, pp. 1568-1573, 1928.

[82] W. Johnson, J. Parson, and M. Crew, "Nitrogen Compounds of Gallium III.Gallic. Nitride," Journal of Physical Chemistry, vol. 36, p. 2561, 1932.

[83] R. Juza and H. Hahn, "Crystal structures of Cu3N, GaN and InN – Metallic amides and metallic nitrides V Announcement," ZEITSCHRIFT FUR ANORGANISCHE UND ALLGEMEINE CHEMIE, vol. 239, pp. 282-287, OCT 1938.

[84] H. Maruska and J. Tietjen, "Preparation and properties of vapor-deposited single-crystalline GaN," APPLIED PHYSICS LETTERS, vol. 15, no. 10, pp. 327-&, 1969.

[85] S. Yoshida, S. Misawa, and S. Gonda, "Improvements on the electrical and luminescent properties of reactive molecular-beam epitaxial grown GaN films by using AlN-coated Sapphire substrates," APPLIED PHYSICS LETTERS, vol. 42, no. 5, pp. 427-429, 1983.

[86] I. Akasaki, H. Amano, Y. Koide, K. Hiramatsu, and N. Sawaki, "Effects of AlN buffer layer on crystallographic structure and on electrical and optial properties of GaN and Ga1-xAlxN (x less than or equal to 0.4) films grown on sapphire substrate by MOVPE," JOURNAL OF CRYSTAL GROWTH, vol. 98, pp. 209-219, NOV 1989.

[87] S. Nakamura Jpn. J. Appl. Phys., vol. 30, p. L1705, 1991.

[88] S. Nakamura, T. Mukai, and M. Senoh, "Candela-class highbrightness InGaN/AlGaN double-heterostructure bluelight emitting diodes," APPLIED PHYSICS LETTERS, vol. 64, pp. 1687-1689, MAR 28 1994.

[89] A. Cho and J. Arthur, "Molecular Beam Epitaxy," Progress in Solid State Chemistry, vol. 10, p. 157, 1975.

[90] S. Yoshida, S. Misawa, and A. Itoh, "Epitaxial-growth of Aluminum nitride films on Sapphire by reactive evaporation," APPLIED PHYSICS LETTERS, vol. 26, no. 8, pp. 461-462, 1975.

[91] H.M. Manasevi, "Single-crystal gallium arsenide on insulating substrates," APPLIED PHYSICS LETTERS, vol. 12, no. 4, pp. 156-159, 1968.

[92] H. Manasevit, F. Erdmann, and W. Simpson, "The Use of Metalorganics in the Preparation of Semiconductor Materials," Journal of The Electrochemical Society, vol. 118, pp. 1864-1868, 1972.

[93] B. Gil, Group III Nitride Semiconductor Compound Physics and Applications. Oxford Science Publications, 1998.

[94] V. Ban, "Mass spectrometric studies of vapor-phase crystal growth .2. GaN," JOURNAL OF THE ELECTROCHEMICAL SOCIETY, vol. 119, no. 6, pp. 761-&, 1972.

[95] T. Aggerstam, Gallium nitride templates and its related materials for electronic and photonic devices. PhD thesis, Royal Institute of Technology, 2008.

[96] Y. Qi, H. Liang, D. Wang, D. Lu, W. Tang, and K. Lau, "Comparison of blue and green InGaN/GaN multiple-quantum-well light-emitting diodes grown by metalorganic vapor phase epitaxy," APPLIED PHYSICS LETTERS, vol. 86, MAR 7 2005.

[97] P. Barletta, Study OF GaN-Based Materials For Light-emitting Applications. PhD thesis, North Carolina State University, 2006.

[98] A. Mircea, A. Ougazzaden, and R. Mellet, "Very uniform epitaxy," PROGRESS IN CRYSTAL GROWTH AND CHARACTERIZATION OF MATERIALS, vol. 19, no. 1-2, pp. 39-49, 1989.

[99] V. Holy, U. Pietsch, and T. Baumbach, "Basic elements of the equipment," in HIGH-RESOLUTION X-RAY SCATTERING FROM THIN FILMS AND MULTILAYERS, vol. 149 of SPRINGER TRACTS IN MODERN PHYSICS, pp.

3-16, HEIDELBERGER PLATZ 3, D-14197 BERLIN, GERMANY: SPRINGER-VERLAG BERLIN, 1999.

[100] G. B. A. Krost and J. Woitok, Optical Characterization of Epitaxia Semiconductor Layers. Berlin: Srpinger, 1995.

[101] R. E.Lee, Scanning Electron Microscopy and X-ray Microanalysis. New Jersey: Prentice Hall, Englewood Cliffs, 1993.

[102] http://mse.iastate.edu/microscopy/path2.html.

[103] C. Kittle, Introduction to Solid State Physics. New Jersey: John Wiley and Sons, Inc., 2005.

[104] C. Y. F. K. C. Khulbe and T. Matsuura, Synthetic Polymeric Membranes Characterization by Atomic Force Microscopy. Berlin: Springer, 2008.

[105] L. Ozawa, Cathodoluminescence and Photoluminescence: Theories and Practical Applications. Taiwan: CRC Press, 2007.

[106] www.brukeroptics.com/.

[107] http://www.labsphere.com.

[108] J. C. R. Brundle, C. A. Evans and S. Wilson, ENCYCLOPEDIA OF MATERIALS CHARACTERIZATION. Butterworth-Heinemann, 1992.

[109] http://www.whoi.edu/.

[110] http://mee-inc.com/xray-photo.html.

[111] http://www.chem.qmul.ac.uk/surfaces/scc/scat5_3.htm.

[112] G. Lanty, J. S. Lauret, E. Deleporte, S. Bouchoule, and X. Lafosse, "UV polaritonic emission from a perovskite-based microcavity," APPLIED PHYSICS LETTERS, vol. 93, AUG 25 2008.

[113] G. Lanty, J. S. Lauret, E. Deleporte, S. Bouchoule, and X. Lafosse, "UV polaritons at room temperature in a microcavity containing perovskites," JOURNAL OF LUMINESCENCE, vol. 129, pp. 1985-1988, DEC 2009. International Conference on Luminescence and Optical Spectroscopy of Condensed Matter (ICL'08), Lyon, FRANCE, JUL 07-11, 2008.

[114] S. Faure, C. Brimont, T. Guillet, T. Bretagnon, B. Gil, F. Medard, D. Lagarde, P. Disseix, J. Leymarie, J. Zuniga-Perez, M. Leroux, E. Frayssinet, J. C. Moreno, F. Semond, and S. Bouchoule, "Relaxation and emission of Braggmode and cavity-mode polaritons in a ZnO microcavity at room temperature," APPLIED PHYSICS LETTERS, vol. 95, SEP 21 2009.

[115] J.-R. Chen, T.-C. Lu, Y.-C. Wu, S.-C. Lin, W.-R. Liu, W.-F. Hsieh, C.-C. Kuo, and C.-C. Lee, "Large vacuum Rabi splitting in ZnO-based hybrid microcavities observed at room temperature," APPLIED PHYSICS LETTERS, vol. 94, FEB 9 2009.

[116] M. Nakayama, S. Komura, T. Kawase, and D. Kim, "Observation of exciton polaritons in a ZnO microcavity with HfO2/SiO2 distributed bragg reflectors," JOURNAL OF THE PHYSICAL SOCIETY OF JAPAN, vol. 77, SEP 2008.

[117] P. Torchio, A. Gatto, M. Alvisi, G. Albrand, N. Kaiser, and C. Amra, "High-reflectivity HfO2/SiO2 ultraviolet mirrors," APPLIED OPTICS, vol. 41, pp. 3256-3261, JUN 1 2002.

[118] R. Thielsch, A. Gatto, J. Heber, and N. Kaiser, "A comparative study of the UV optical and structural properties of SiO2, Al2O3, and HfO2 single layers deposited by reactive evaporation, ion-assisted deposition and plasma ion-assisted deposition," THIN SOLID FILMS, vol. 410, pp. 86-93, MAY 1 2002.

[119] http://www.emse.fr/.

[120] T. Glisson, J. Hauser, M. Littlejohn, and C. Williams, "Energy bandgap and lattice-constant contours of III-V quaternary alloys," JOURNAL OF ELECTRONIC MATERIALS, vol. 7, no. 1, pp. 1-16, 1978.

[121] J. Borgulov, F. Uherek, J. Kovc, and A. Satka, "Design of Multilayer optoelectronic Devices," IEEE, SPIE Proc. Ser., vol. 3820, p. 239, 1999.

[122] Z. Knittl, Optics of thin lms. SNTL - Wiley, 1976.

[123] N. Ekins-Daukes, K. Kawaguchi, and J. Zhang, "Strain-balanced criteria for multiple quantum well structures and its signature in X-ray rocking curves," CRYSTAL GROWTH & DESIGN, vol. 2, pp. 287-292, JUL-AUG 2002.

[124] J.-M. Bethoux, Relaxation des contraintes dans les hétérostructures épaisses (Al,Ga)N : une piste originale pour la réalisation de diodes électroluminescentes à cavité résonante. PhD thesis, Université de Nice Sophia-Antipolis, 2004.

[125] N. Nakada, H. Ishikawa, T. Egawa, and T. Jimbo, Suppression of crack generation in GaN/AIGaN distributed Bragg reflector on sapphire by the insertion of GaN/AIGaN superlattice grown by metal-organic chemical vapor deposition," JAPANESE JOURNAL OF APPLIED PHYSICS PART 2-LETTERS, vol. 42, pp. L144-L146, FEB 15 2003.

[126] Z.-Y. Li, T.-C. Lu, H.-C. Kuo, S.-C. Wang, M.-H. Lo, and K. M. Lau, "HRTEM investigation of high-reflectance AlN/GaN distributed Bragg-reflectors by inserting AlN/GaN superlattice," JOURNAL OF CRYSTAL GROWTH, vol. 311, pp. 3089-3092, MAY 1 2009. 2nd International Symposium on Growth of III Nitrides (ISGN-2), Laforet Shuzenji, JAPAN, JUL 07-09, 2008.

[127] J. Bean, L. Peticolas, R. Hull, D. Windt, R. Kuchibhotla, and J. Campbell, "Design and fabrication of asymmetric strained layer mirrors for optoelectronics applications," APPLIED PHYSICS LETTERS, vol. 63, pp. 444-446, JUL 26 1993.

[128] V. Gupta, C. Wamsley, M. Koch, and G. Wicks, "Molecular beam epitaxy growth of boron-containing nitrides," JOURNAL OF VACUUM SCIENCE & TECHNOLOGY B, vol. 17, pp. 1246-1248, MAY-JUN 1999.

[129] T. Takano, M. Kurimoto, J. Yamamoto, and H. Kawanishi, "Epitaxial growth of high quality BAlGaN quaternary lattice matched to AlN on 6H-SiC substrate by LP-MOVPE for deep-UV emission," JOURNAL OF CRYSTAL GROWTH, vol. 237, pp. 972-977, APR 2002.

[130] T. Takano, M. Kurimoto, J. Yamamoto, M. Shibata, Y. Ishihara, M. Tsubamoto, T. Honda, and H. Kawanishi, "Room-temperature photoluminescence from BAlGaN-based double or single heterostructures for UV laser diode," PHYSICA STATUS SOLIDI A-APPLIED RESEARCH, vol. 180, pp. 231-234, JUL 16 2000.

[131] L. Teles, J. Furthmuller, L. Scolfaro, A. Tabata, J. Leite, F. Bechstedt, T. Frey, D. As, and K. Lischka, "Phase separation and gap bowing in zinc-blende InGaN, InAlN, BGaN, and BAlN alloy layers," PHYSICA E-LOW-DIMENSIONAL

SYSTEMS & NANOSTRUCTURES, vol. 13, pp. 1086-1089, MAR 2002. 10th International Conference on Modulated Semiconductor Structures, LINZ, AUSTRIA, JUL 23-27, 2001.

[132] C. Wei and J. Edgar, "Unstable composition region in the wurtzite B1-xyGaxAlyN system," JOURNAL OF CRYSTAL GROWTH, vol. 208, pp. 179-182, JAN 2000.

[133] R. Farivar and T. G. Andersson, "Initial boron growth on GaN and AlN surfaces by molecular beam epitaxy," in PHYSICA STATUS SOLIDI C: CURRENT TOPICS IN SOLID STATE PHYSICS, VOL 7, NO 1, pp. 25-27, 2010.

[134] J. Hutchinson and Z. Suo, "Mixed-mode cracking in layered materials," in ADVANCES IN APPLIED MECHANICS, VOL 29, vol. 29 of ADVANCES IN APPLIED MECHANICS, pp. 63-191, 525 B STREET, SUITE 1900, SAN DIEGO, CA 92101-4495: ACADEMIC PRESS INC, 1992.

[135] S. Jain, J. Willis, and R. Bullough, "A review of theoretical and experimental work on the structure of GaxSi1-x strained layers and superlattices, with extensive bibliography," ADVANCES IN PHYSICS, vol. 39, pp. 127-190, MAR-APR 1990.

[136] R. People and J. Bean, "Calculation of critical layer thickness versus lattice mismatch for GexSi1-x/Si strained layer heterostructures," APPLIED PHYSICS LETTERS, vol. 47, no. 3, pp. 322-324, 1985.

[137] A. Fischer, H. Kuhne, and H. Richter, "New approach in equilibrium-theory for strained-layer relaxation," PHYSICAL REVIEW LETTERS, vol. 73, pp. 2712-2715, NOV 14 1994.

[138] T. Sugahara, H. Sato, M. Hao, Y. Naoi, S. Kurai, S. Tottori, K. Yamashita, K. Nishino, L. Romano, and S. Sakai, "Direct evidence that dislocations are non-radiative recombination centers in GaN," JAPANESE JOURNAL OF APPLIED PHYSICS PART 2-LETTERS, vol. 37, pp. L398-L400, APR 1 1998.

[139] D.-B. Li, M. Aoki, T. Katsuno, H. Miyake, K. Hiramatsu, and T. Shibata, "Influence of growth interruption and Si doping on the structural and optical properties of AlxGaN/AlN ($x > 0.5$) multiple quantum wells," JOURNAL OF CRYSTAL GROWTH, vol. 298, pp. 500-503, JAN 2007. 13th International Conference on Metal Organic Vapor Phase Epitaxy, Miyazaki, JAPAN, MAY 22-26, 2006.

[140] S. Sumiya, Y. Zhu, J. Zhang, K. Kosaka, M. Miyoshi, T. Shibata, M. Tanaka, and T. Egawa, "AlGaN-based deep ultraviolet light-emitting diodes grown on epitaxial AIN/sapphire templates," JAPANESE JOURNAL OF APPLIED PHYSICS, vol. 47, pp. 43-46, JAN 2008.

[141] K. Nagamatsu, N. Okada, H. Sugimura, H. Tsuzuki, F. Mori, K. Iida, A. Bando, M. Iwaya, S. Kamiyama, H. Amano, and I. Akasakia, "High-efficiency AlGaN based UV light-emitting diode on laterally overgrown AlN," JOURNAL OF CRYSTAL GROWTH, vol. 310, pp. 2326-2329, APR 2008. 15th International Conference on Crystal Growth, Salt Lake City, UT, AUG 12-17, 2007.

[142] R. Gaska, C. Chen, J. Yang, E. Kuokstis, A. Khan, G. Tamulaitis, I. Yilmaz, M. Shur, J. Rojo, and L. Schowalter, "Deep-ultraviolet emission of AlGaN/AlN quantum wells on bulk AlN," APPLIED PHYSICS LETTERS, vol. 81, pp. 4658-4660, DEC 9 2002.

[143] S. H. Park, "Theoretical study of optical properties in deep ultraviolet Al-rich AlGaN/AIN quantum wells," SEMICONDUCTOR SCIENCE AND TECHNOLOGY, vol. 24, MAR 2009.

[144] S. OLeary, S. Johnson, and P. Lim, "The relationship between the distribution of electronic states and the optical absorption spectrum of an amorphous semiconductor: An empirical analysis," JOURNAL OF APPLIED PHYSICS, vol. 82, pp. 3334-3340, OCT 1 1997.

[145] N. Grandjean, B. Damilano, S. Dalmasso, M. Leroux, M. Laugt, and J. Massies, "Built-in electric-field effects in wurtzite AlGaN/GaN quantum wells," JOURNAL OF APPLIED PHYSICS, vol. 86, pp. 3714-3720, OCT 1 1999.

[146] H. Teisseyre, T. Suski, S. Lepkowski, S. Anceau, P. Perlin, P. Lefebvre, L. Konczewicz, H. Hirayama, and Y. Aoyagi, "Determination of built-in electric fields in quaternary InAlGaN heterostructures," APPLIED PHYSICS LETTERS, vol. 82, pp. 1541-1543, MAR 2003.

[147] M. Reshchikov and H. Morkoc, "Luminescence properties of defects in GaN," JOURNAL OF APPLIED PHYSICS, vol. 97, MAR 15 2005.

[148] M. Abid, T. Moudakir, Z. Djebbour, G. Orsal, S. Gautier, A. E. Naciri, A. Migan-Dubois, and A. Ougazzaden, "Blue-violet boron-based Distributed Bragg Re ectors for VCSEL application," JOURNAL OF CRYSTAL GROWTH, vol. 315, pp. 283-

287, JAN 15 2011. 15th International Conference on Metalorganic Vapor Phase Epitaxy (ICMOVPE-XV), Incline Village, NV, MAY 23-28, 2010.

[149] M. B. Kanoun and S. Goumri-Said, "Theoretical study of structural parameters and energy gap composition dependence of Ga1-xBxN alloys," SEMICONDUCTOR SCIENCE AND TECHNOLOGY, vol. 23, DEC 2008.

[150] G. Jellison and F. Modine, "Parameterization of the optical functions of amorphous materials in the interband region," APPLIED PHYSICS LETTERS, vol. 69, pp. 371-373, JUL 15 1996.

[151] G. Jellison, F. Modine, P. Doshi, and A. Rohatgi, "Spectroscopic ellipsometry characterization of thin-film silicon nitride," THIN SOLID FILMS, vol. 313, pp. 193-197, FEB 1998.

[152] D. Aspnes, "Optical-properties of thin-films," THIN SOLID FILMS, vol. 89, no. 3, pp. 249-262, 1982.

[153] M. Born and E. Wolf, Principles of Optic. 1959.

[154] M. Kauser, A. Osinsky, A. Dabiran, and S. Pearton, "Optimization of conductivity in p-type GaN/InGaN-graded superlattices," JOURNAL OF APPLIED PHYSICS, vol. 97, APR 15 2005.

[155] M. Kauser, A. Osinsky, A. Dabiran, and P. Chow, "Enhanced vertical transport in p-type AlGaN/GaN superlattices," APPLIED PHYSICS LETTERS, vol. 85, pp. 5275-5277, NOV 29 2004.

[156] M. Kneissl, Z. Yang, M. Teepe, C. Knollenberg, O. Schmidt, P. Kiesel, N. M. Johnson, S. Schujman, and L. J. Schowalter, "Ultraviolet semiconductor laser diodes on bulk AlN," JOURNAL OF APPLIED PHYSICS, vol. 101, JUN 15 2007.

[157] O. Ambacher, "Growth and applications of Group III nitrides," JOURNAL OF PHYSICS D-APPLIED PHYSICS, vol. 31, pp. 2653-2710, OCT 21 1998.

[158] H. Morkoc, Handbook of nitride semiconductors and devices 1. 2008.

[159] F. Bernardini, V. Fiorentini, and D. Vanderbilt, “Spontaneous polarization and piezoelectric constants of III-V nitrides,” PHYSICAL REVIEW B, vol. 56, pp. 10024-10027, OCT 15 1997.